NANO/MICROSYSTEMS FOR CANCER DIAGNOSIS AND THERAPY

Manuel García Algar

UNIVERSITAT ROVIRA i VIRGILI

Optical methods and nano/microsystems for cancer diagnosis and therapy

Manuel García Algar

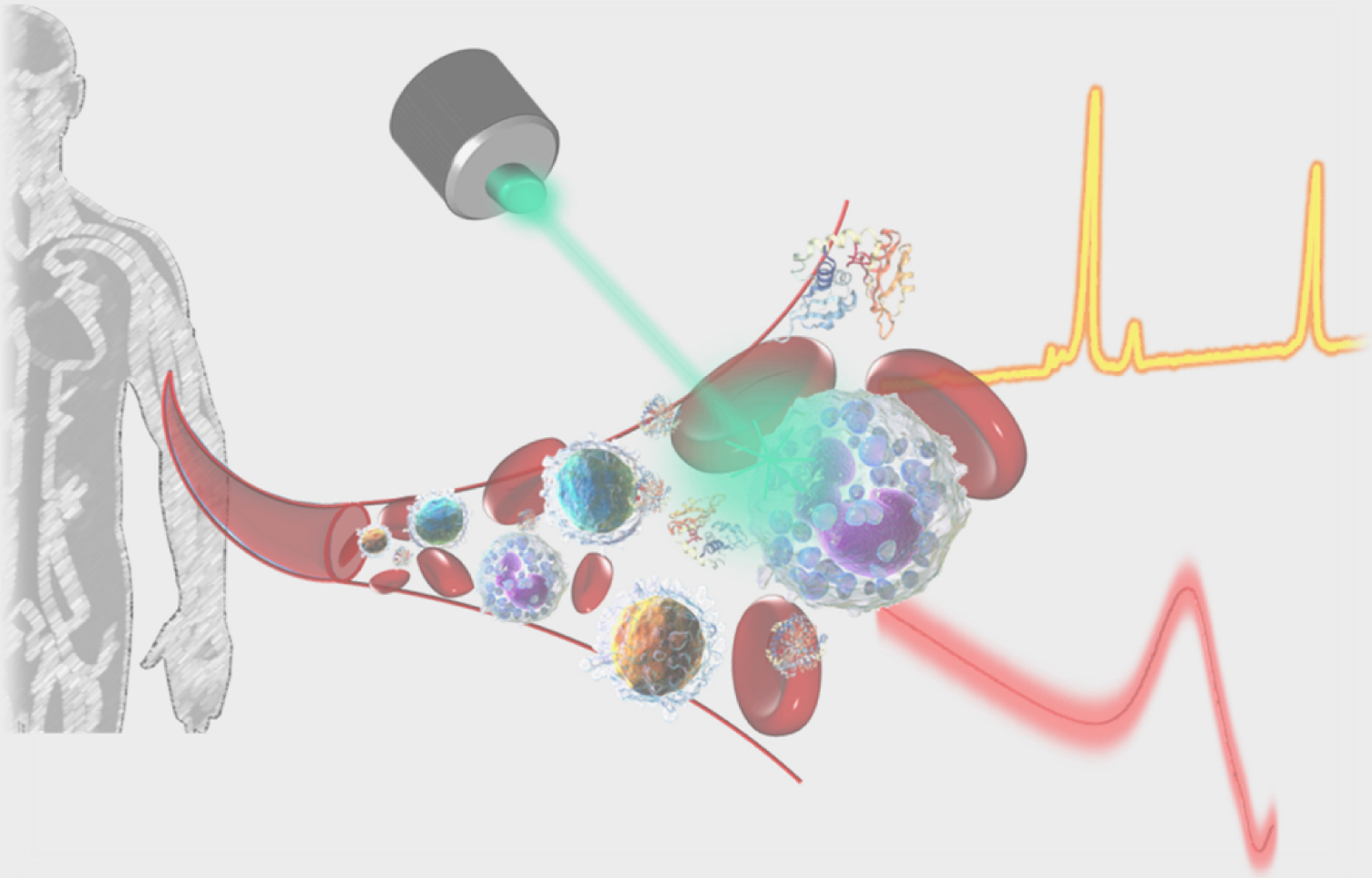

DOCTORAL THESIS
2018

UNIVERSITAT ROVIRA I VIRGILI
NANO/MICROSYSTEMS FOR CANCER DIAGNOSIS AND THERAPY
Manuel García Algar

UNIVERSITAT ROVIRA I VIRGILI
NANO/MICROSYSTEMS FOR CANCER DIAGNOSIS AND THERAPY
Manuel García Algar

UNIVERSITAT ROVIRA I VIRGILI
NANO/MICROSYSTEMS FOR CANCER DIAGNOSIS AND THERAPY
Manuel García Algar

Manuel García Algar

Optical methods and nano/microsystems for cancer diagnosis and therapy

DOCTORAL THESIS

Industrial Mention

Supervised by

Prof. Ramón A. Álvarez-Puebla

Dr. Nicolás C. Pazos Pérez

Department of Physical and Inorganic Chemistry

Tarragona, 2018

UNIVERSITAT ROVIRA i VIRGILI

medcom advance

UNIVERSITAT ROVIRA I VIRGILI
NANO/MICROSYSTEMS FOR CANCER DIAGNOSIS AND THERAPY
Manuel García Algar

Aquesta tesi s'ha realitzat amb el suport de la Secretaria d'Universitats i Recerca del Departament d'Empresa i Coneixement de la Generalitat de Catalunya.

Generalitat de Catalunya
Departament d'Empresa i Coneixement
Secretaria d'Universitats i Recerca

UNIVERSITAT ROVIRA I VIRGILI
NANO/MICROSYSTEMS FOR CANCER DIAGNOSIS AND THERAPY
Manuel García Algar

UNIVERSITAT ROVIRA i VIRGILI

Departament of Physical and Inorganic Chemistry
c/Marcel·lí Domingo s/n, Edifici N4
Campus Sescelades
43007 Tarragona, Spain
secfqui@urv.cat

I STATE that the present study, entitled "**Optical methods and nano/microsystems for cancer diagnosis and therapy**", presented by **Manuel García Algar** for the award of the degree of Doctor, has been carried out under my supervision at the Department Physical and Inorganic Chemistry of this university.

Tarragona, February 2018

Doctoral Thesis Supervisor/s

Prof. Ramón A. Álvarez Puebla

Dr. Nicolás C. Pazos Pérez

UNIVERSITAT ROVIRA I VIRGILI
NANO/MICROSYSTEMS FOR CANCER DIAGNOSIS AND THERAPY
Manuel García Algar

Agradecimientos

No resulta fácil resumir estos más de tres años de tesis en unas pocas líneas pues no sólo he crecido a nivel profesional sino que también a nivel personal. Parecía un largo trayecto con un destino muy lejano y complejo de alcanzar, pero que al final se ha cumplido gracias al esfuerzo diario y el apoyo de muchas personas.

En primer lugar, me gustaría agradecer al Prof. Ramón Álvarez Puebla haberme brindado la oportunidad de entrar en su grupo de investigación y por creer en mis capacidades. Gracias por enseñarme el pensamiento científico y crítico y las posibilidades de desarrollo profesional en la ciencia.

Hacer mención a todas las colaboraciones que han contribuido al desarrollo de esta tesis: al Prof. Wolfgang Parak y la Dra. Neus Feliu de la Phillips-Universität de Märburg, que me acogieron y enseñaron cómo trabajar con el citómetro de flujo; al Prof. Francesc Díaz del grupo de Física y Ciencia de Materiales de la Universidad Rovira i Virgili y a su doctorando Eric Pedrol, por su colaboración en el desarrollo de dispositivos microfluídicos.

A los doctores Luca Guerrini, Nicolás Pazos y Moritz Nazarenus por guiarme y transmitirme sus conocimientos en los campos de la química física tan lejana para alguien como yo, proveniente de ciencias biológicas. A las doctoras Sara Gómez y Elena Pazos, por su continua ayuda científica y moral que siempre han estado apoyándome y consolando en los altibajos emocionales producto de resultados experimentales inesperados.

Especialmente, me gustaría agradecer a mis compañeros de tesis, Ana, Alicia, Arnau, Patri, Carme, Bernat y a mi querida amiga Judit. Sin ellos estos tres años no hubieran sido igual de provechosos que lo han sido, pues han supuesto un apoyo incondicional. Muchas gracias por las horas y horas de trabajo codo con codo, los largos ratos de risas y diversión, las charlas científicas para resolver problemas, las fiestas, las meriendas y vuestro gusto para corregirme los colores de los trabajos.

Tampoco puedo dejar de mencionar a mis amigos de siempre, David, Genís y Gerard y los de la universidad Katherine, Maria, Carol, Ana, Cristina…, que siempre creen en mí y nunca se olvidan de preocuparse por mí aunque sea para escribirme una tontería.

Agradecer a mis recientes amistades de CampusRom, que me hacen sentir un referente para muchos de ellos y que se fortalecen a seguir adelante en la lucha por la inclusión de minorías en todos los ámbitos de la sociedad.

Finalmente, quiero dedicar este párrafo a agradecerle a toda mi familia. A mi hermana y a mi hermano por estar siempre a mi lado, ya que suponen los dos pilares fundamentales de mi vida. Y sobre todo, a mi papa y a mi mama, por haberme educado e inculcado los mejores valores que han podido, los cuales me hacen ser la persona que soy y por apoyarme en todo lo que hago.

" Nunca consideres el estudio como una obligación, sino como una oportunidad para penetrar en el bello y maravilloso mundo del saber."

Albert Einstein

UNIVERSITAT ROVIRA I VIRGILI
NANO/MICROSYSTEMS FOR CANCER DIAGNOSIS AND THERAPY
Manuel García Algar

Contents

Abbreviations

^{1}H NMR	proton nuclear magnetic resonance
^{18}F-FDG	2-[^{18}F]fluoro-2-deoxy-D-glucose
2-NBDG	2-[N-(7-nitrobenz-2-oxa-1,3-diazol-4-yl)amino]-2-deoxy-D-glucose
2-DG	2-D-glucose
A549	adenocarcinoma human lung cancer cell line
Ala	alanine
AMPB	adaptive metabolic pattern biomarker
APC	allophycocyanin
APS	aminopropylsilane
ATP	adenosine 5'-triphosphate
CCD	charge-coupled device
CD45	cluster of differentiation 45
CD14	cluster of differentiation 14
cfNA	cell-free nucleic acid
CP	cancer patient
CT	computational tomography
CTC	circulating tumor cell
ctDNA	circulating tumor deoxyribonucleic acid
ctmRNA	circulating tumor messenger ribonucleic acid
ctRNA	circulating tumor ribonucleic acid
CVD	chemical vapor deposition
DMF	dimethylformamine
DNA	deoxyribonucleic acid

EDX energy dispersive X-ray spectroscopy

ELISA enzyme-linked immunoabsorbent assay

EMT epithelial-mesenchymal transition

EpCAM epithelial cell adhesion molecule

EPR enhanced permeability and retention

ErbB HER, human epidermal growth factor receptor

FDA Food and Drug Administration

FGFR fibroblast growth factor receptor

FIB focused ion beam

FSC forward scattering

GLUT glucose transporter

GFR growth factor receptor

HER human epidermal growth factor receptor family

HRP horseradish peroxidase

IC internal conversion

IGFR insulin growth factor receptor

IR infrared

ISC intersystem crossing

KD kernel density

LB liquid biopsy

LD_{50} lethal dose 50%

LSPR local surface plasmon resonance

MAPK mitogen-activated protein kinase

MCF-7 Michigan Cancer Foundation breast cancer cell line 7

MDA-MB-435 breast melanoma cell line

MBL metabolic liquid biopsy

mRNA messenger ribonucleic acid

NIR	near-infrared
NSCLC	non-small cell lung cancer
OS	overall survival
PBMC	peripheral blood mononuclear cell
PET	positron emission tomography
PFS	progression free survival
Phe^{522}	phenilalanine residue modified at position 522
PSiP	porous silicon particle
Ras-GDP	retrovirus associated-DNA sequence guanosine 5'-diphosphate
Ras-GTP	retrovirus associated-DNA sequence guanosine 5'-triphosphate
RNA	ribonucleic acid
RT	room temperature
S	spin multiplicity
SCLC	small cell lung cancer
SEM	scanning electron microscopy
Ser^{520}	serine residue modified at position 520
SERS	surface-enhanced Raman scattering
SGLT	sodium-dependent glucose transporter
SK-BR-3	Memorial Sloan-Kettering Cancer center breast cancer cell line 3
SSC	sight scattering
SUV	standardized uptake value
TEM	transmission electron microscopy
TGF-βR	tumor growth factor β receptor
THF	tetrahydrofuran
TKI	tyrosine kinase inhibitor
TLC	thin layer chromatography
TNM	imaging techniques

UV ultraviolet

VEGFR vascular endothelial growth factor receptor

WB western blot

UNIVERSITAT ROVIRA I VIRGILI
NANO/MICROSYSTEMS FOR CANCER DIAGNOSIS AND THERAPY
Manuel García Algar

UNIVERSITAT ROVIRA I VIRGILI
NANO/MICROSYSTEMS FOR CANCER DIAGNOSIS AND THERAPY
Manuel García Algar

Thesis scope

Cancer disease represents one of the most widespread public health problem still to be solved. As a genetic disease, the heterogeneous nature makes challenge to find out a general solution for its prognosis, diagnosis and treatment. Consequently, efforts have focused during decades on studying and understanding the genetics and further molecular basis behind the disease. Mainly, cancer is product of a deregulated cell division resulting in a solid tumor formation than can become malignant and metastasize to surrounding tissues, travelling within the bloodstream. Lots of cancerous material can be released to the blood in form of nucleic acids, proteins or cells, and its detection and analysis can provide relevant information of the pathogenesis. Molecular identification of those materials not only can advise about the progression of cancer, but also can instruct of subsequent treatment for its eradication.

Several specific and high-sensitivity fluorescent techniques and other optical methods, such as surface-enhanced Raman scattering (SERS), are commonly used, as in immunohistochemistry, for classification of cancer and molecular evaluation, with slices from solid tumor biopsies. Recently, liquid biopsies have gained relevance in clinical oncology, since they represent a potential alternative to invasive biopsies due to their easy manner of sampling collection.

In this stage, **the main objectives of this experimental work are: (i) to develop new optical methods for detection of cancerous material in liquid biopsies and (ii) to build up a platform for cancer targeting and therapy.**

To successfully accomplish these purposes, two different strategies will be approached for cancer diagnosis: one method based on the use of a fluorescent label to highlight entire cancer cells (CTCs) front normal cells in human blood and its application in lung cancer diagnosis, and a second method, based on a SERS platform for detection and quantification of an oncoprotein c-MYC in breast cancer.

2 Thesis scope

For cancer therapy, a platform based in a hybrid material is engineered to specifically target and eliminate HER-2 breast cancer cells *in vitro*.

Accordingly, this dissertation comprises five different chapters:

In **Chapter 1**, it will be described the molecular basis of cancer, exploring from genetics to aberrant behavior of cancer cells and the metastatic process to secondary sites. The second part of the chapter will focus on explaining physical concepts behind the optical techniques used in biomedical research.

The first method developed for cancer diagnosis will be shown in **Chapter 2**. Basically, it consists in the exploitation of cancer behavior to acquire larger amounts of sugars to support metabolic requirements. Using a fluorescent glucose analogue 2-NBDG it will be describe a methodology to identify cancer cells within human blood, under optimized conditions.

After its description and demonstration, the developed method in previous chapter will be implemented in **Chapter 3** for the detection and quantification of CTCs in patients with human lung cancer at different stages of the disease. The results of the method will be statistically analyzed and contrasted with conventional clinical oncology techniques.

Chapter 4 will focused on the explanation of a second developed method for cancer diagnosis, as well. This is based on the construction of a nano/microsystem composed by silica microbeads decorated with silver plasmonic nanoparticles. By holding a SERS reporter the sensing platform is able to induce a quantitative optical response when detecting c-MYC oncoprotein from both breast cancer cell lines and cancer patient blood.

To end, an immunotherapeutic agent will be described in **Chapter 5** for cancer targeting approaches. Silicon microparticles will serve here as essence of the system, carrying antibodies to target specific HER-2 positive breast cancer cells and covered with a protection shell that triggers its toxicological effect upon internalization by cancer cells *in vitro*.

CHAPTER 1

UNIVERSITAT ROVIRA I VIRGILI
NANO/MICROSYSTEMS FOR CANCER DIAGNOSIS AND THERAPY
Manuel García Algar

Theoretical background

Cancer is one of the most widespread diseases over the world and efforts towards its understanding and treatment at the molecular level are a hot topic in research. Cancer cells are consequence of the accumulation of various mutations on the genetic material that lead to the expression of aberrant phenotypes. In fact, these cells can even acquire the ability to invade other healthy tissues, generating metastatic processes, by colonizing the bloodstream. Nowadays, optical methods, such as fluorescence or Raman spectroscopy, applied to the medicine, may engineer new potential techniques and devices for the examination of the circulating tumor cells in peripheral blood guiding clinicians in their decision making.

1 Cancer

All cells from an organism are product of several rounds of cell growth and division, where each singular cell is capable to duplicate its content and divide in two, under a process known as *cell cycle* (Fig.1). [1]

To ensure an appropriate equilibrium within the organism and its organs and tissues, cell division is carefully controlled by intracellular programs, *e.g.* apoptosis or programmed cell death, and extracellular signals that modulate these programs.[1]

[1] Alberts B, J. A., Lewis J, et al. *Molecular Biology of the Cell*; 6 ed.; Garland Sciences, **2014**; Vol. 1.

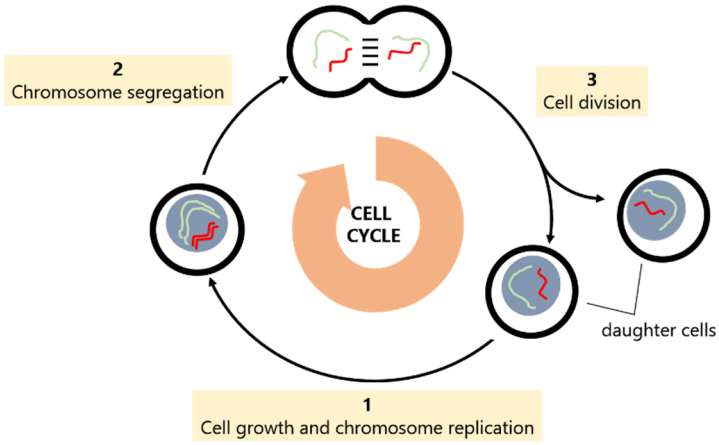

FIGURE 1.1 Schematic representation of the cell cycle. A haploid cell start growing and replicating its genetic content to become diploid. Diploid cell start mitosis segregating the chromosomes and dividing the cell membrane into two daughter cells.

In *cancer*, cells change the basic rules of cell behavior by overpassing the normal cell cycle controls and colonizing other tissues. [1] Without response to these *checkpoints* they continuously divide and proliferate resulting in a solid mass or tumor. [2, 3] This can happen from the abnormality of just one single cell which, after the accumulation of several number of genetic mutations in different genes, gradually evolved into an aberrant cell. This mutability in the tumor cells allows them to continue proliferating when normal cells would stop. Consequently, cancer cells acquire a collection of abnormalities, such as the ability to do not obey the cell death programs or to move away from the original place spreading and developing new tumors in other tissues. Cancer account for approximately 13% of deaths. This makes invasive cancer the leading cause of death in the developed world and the second leading in the developing world. [1-4]

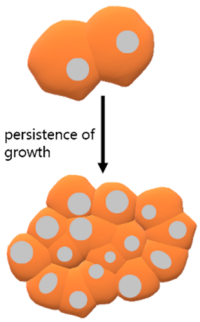

FIGURE 1.2 Cell division lead to a cell mass formation.

[2] *Nature Cell Biology* **2012**, *15*, 1.
[3] Coleman, W.; Rubinas, T. In *Molecular Pathology*, Elsevier, Ed. Oxford, **2009**, p 63
[4] Hanahan, D.; Weinberg, R. A. *Cell* **2011**, *144*, 646.

Cancer as a continuous cell division

The genetic information of living organism is registered in a molecule present inside all living cells, the DNA. DNA is subject to constant chemical damage due to its exposure to exogenous agents, but also due to errors during its replication in the cell cycle when generating new copies. These spontaneous mutations in the genetic material can accumulate in a same cell and be responsible of the subsequent aberrant behavior. [1-6]

Many genes are repeatedly mutated in human cancers and have been deeply identified and studied during last decades. These critical genes are classified into two different groups depending on the function they drive in the cell: (i) proto-*oncogenes*, which produce a gain-of-function for cancer evolution and (ii) *tumor suppressor genes*, which produce a loss-of-function. (**Fig. 1.3**). [1, 5, 6]

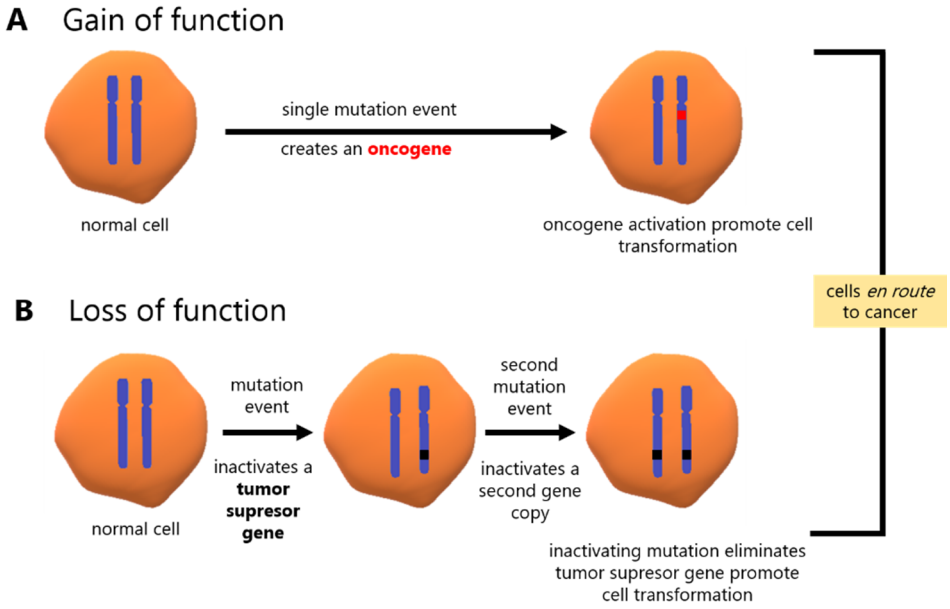

FIGURE 1.3 Mutations can fall into two distinguishable types of critical genes, (A) oncogene or (B) tumor suppressor gene, leading to cancer.

[5] Russell, P. J. *iGenetics A molecular approach*, 3 ed.; Pearson Education, **2010**; Vol. 1.
[6] Bertram, J. S. *Mol Aspects Med* **2000**, *21*, 167.

Proto-oncogenes become oncogenes when mutated and are normally involved in cell cycle regulation, stimulation to an infinite cell proliferation, development of resistance to program death or independency to growth stimulatory signals. On the other hand, mutations in tumor suppressor genes lead cells to unfollow the growth inhibitory signals. Depending of the processes where these genes are acting, their mutation may result in a continuous cell division that never ends.[5] **Fig. 1.4** describes different manners of how these mutated critical genes wind up stimulating cell growth and proliferation (**Fig. 1.4**).[1]

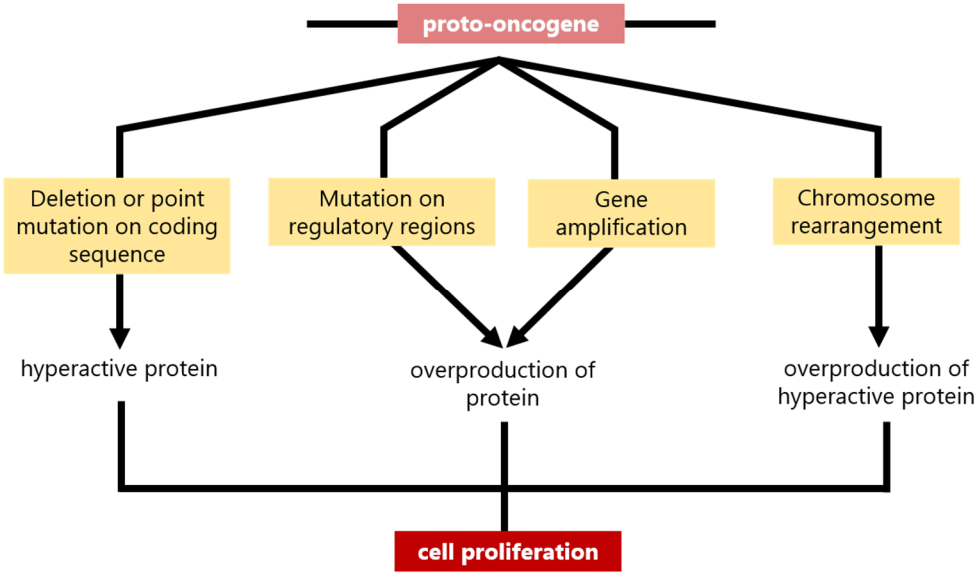

FIGURE 1.4 Types of mutations that can convert proto-oncogenes into oncogenes and the phenotypic result.

(i) Inappropriate activation of transcription factors

As described by the central dogma of the molecular biology, the genetic information content into DNA flows to RNA, in a process known as transcription. This last is translated to proteins, in a well-regulated and spatially determined process. Major regulation on the gene expression takes place during transcription step, where an enzyme -RNA polymerase- specifically produces a ribonucleotide-chain complementary to an original

DNA template. Herein, other proteins or *transcription factors* directly interact with the DNA strands and polymerases in a complex that activate or repress the expression of a target gene (**Fig. 1.5**). [1, 5-7]

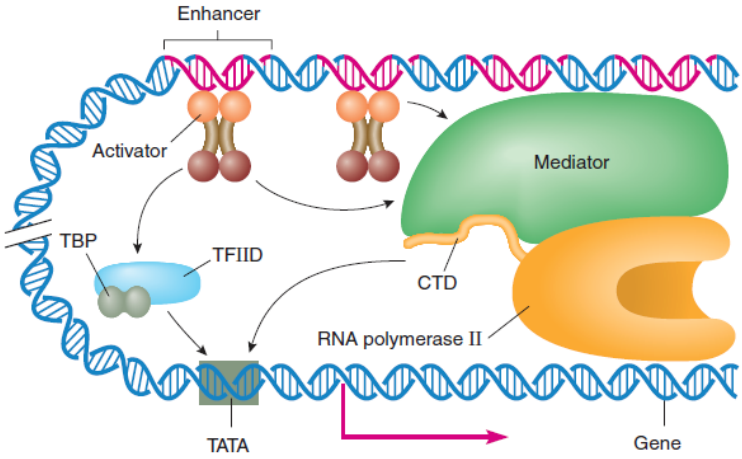

FIGURE 1.5 Schematic representation of action of transcription factors as mediators of gene expression.

One way of achieving uncontrolled cell growth is by the mutation of proto-oncogenes in which their products are involved in the activation of transcription factors through signaling pathways, *e.g.* SCR, ABL or RAS. Most of these signaling pathways begin with extracellular cell-surface receptors which after binding a ligand generate an activation of the intracellular domains serine or tyrosine-kinase dependent. Subsequently, cytoplasmatic proteins connected to these ligand-activated receptors continue a kinase cascade with a final activation of transcription factors involved in gene expression regulation. [1, 5-8]

Three different types of transcription factors have been described to be deregulated in human cancers: (i) steroid receptors (*e.g.* estrogen and

[7] Lehninger, A.; Nelson, D. L.; Cox, M. M. *Principles of Biochemistry*, 6 ed.; WH Freeman and Company, **2013**; Vol. 1.
[8] Darnell Jr, J. E. *Nature Reviews Cancer* **2002**, *2*, 740.

progesterone receptors); (ii) latent cytoplasmic transcription factors (*e.g.* NF-KB or Notch); and, (iii) resident nuclear proteins (e.g. c-Jun, FRA or c-Myc). [8] For example, the protein Ras-GTP, product of the RAS proto-oncogene, mutates in many cancers. When an extracellular ligand, the epidermal growth factor (EFG), binds to EGF cell-surface receptor, promotes its activation by phosphorylation. This induces the recruitment of cytoplasmatic proteins – GRB2 and SOS- which allows Ras-GDP to bind GTP. Ras-GTP initiates a signal cascade based on phosphorylations of proteins including ERK that moves to the nucleus of the cells and activates nuclear transcription factors. This process leads to the transcription of a set of cell division-stimulating genes. Mutated form of RAS oncogene, does not allow to release GTP maintaining Ras-GTP always on, inappropriately activating other transcription factors involved in the pathway and keeping the cell in continuous division (**Fig. 1.6**).[5, 8, 9]

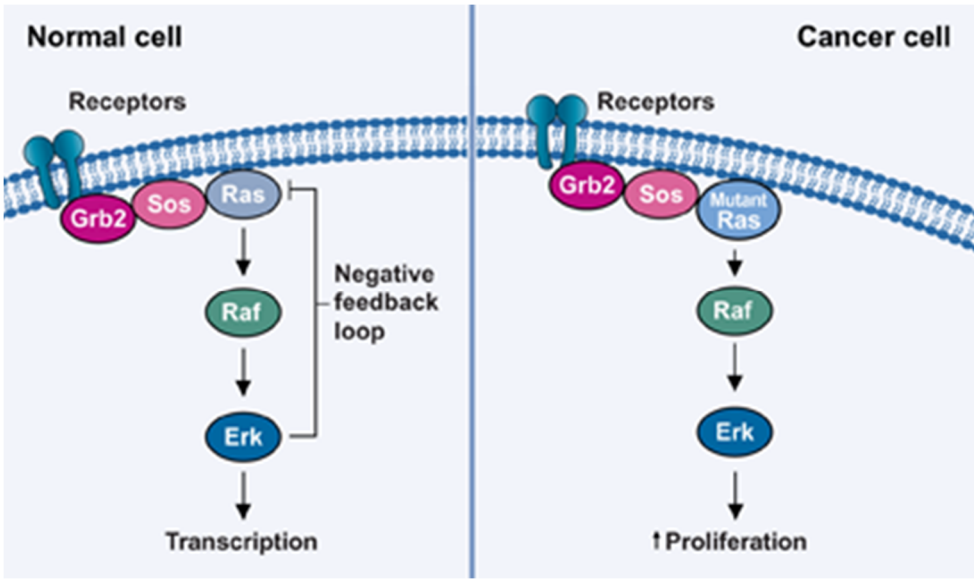

FIGURE 1.6 Schematic representation of Ras-GTP pathway in normal and in cancer.

[9] Dang, C. V. *Cell* **2012**, *149*, 22.

Nuclear transcription factors, e.g. c-JUN or c-MYC, act as transcription mediators by their direct interaction with DNA, when activated by Ras-GTP signaling cascade. They might be constitutively bound to DNA but need specific phosphorylation on serine or threonine residues, provided by Ras cascade, to be fully active in stimulating the transcription. Additionally, they act by association with other transcription factors forming complexes. As an example, c-Myc does not regulates transcription by itself, but dimerize with protein Max. The Myc-Max heterodimer interact with other cofactors, as TFIIH, TRAAP and GCN5, that ends with the expression of genes that stimulates the cell division (**Fig. 1.7**). [1, 5, 8-10]

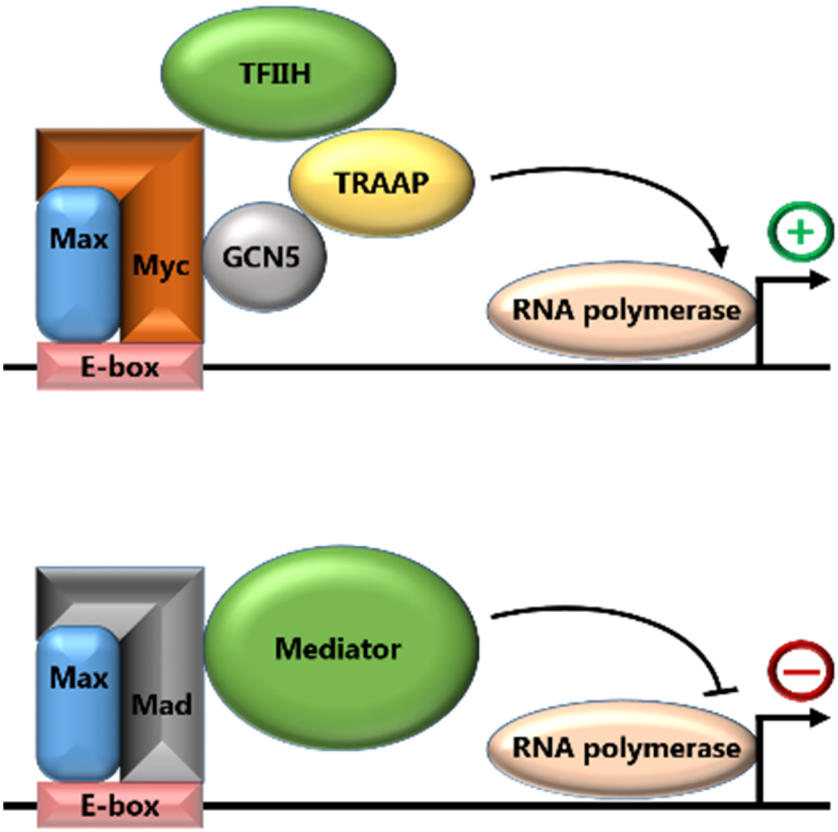

FIGURE 1.7 Schematic representation of gene expression regulated by Myc-Max heterodimer.

[10] Wang, Y. H.; Liu, S.; Zhang, G.; Zhou, C. Q.; Zhu, H. X.; Zhou, X. B.; Quan, L. P.; Bai, J. F.; Xu, N. Z. *Breast Cancer Res* **2005**, *7*, 17.

(ii) Inappropriate expression of growth factor receptors

Other mechanism for the conversion of a proto-oncogene into an oncogene may result in an overproduction of a protein by the mutation of regulatory regions or gene amplification events which may produce extra gene copies and, consequently, many copies of the protein.[1, 5-7] An example of these overexpressed proteins is the *growth factor receptors* (GFRs). GFRs expressed on the cell membranes and cytoplasm have an important role in cell growth, survival and further division as they are involved in the initiation of signaling pathways that avoid apoptosis and keep cells proliferating (**Fig. 1.8**). Consequently, their deregulation is directly implicated in an aberrant cell growth. Different families of GFRs have been described to be overexpressed in cancer as the epidermal growth factor receptor (EGFR), insulin-growth factor receptor (IGFR), transforming growth-factor beta receptor (TGF-βR), vascular endothelial growth factor receptor (VEGFR) or the fibroblast growth factor receptor (FGFR). [1, 11]

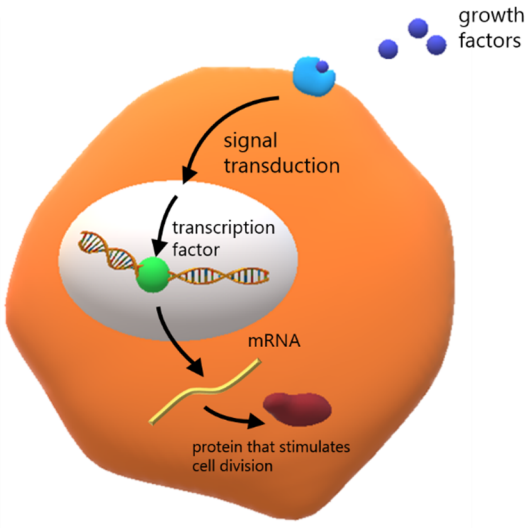

FIGURE 1.8 Schematic representation of growth factor activation of signal cascade ending with expression of survival genes.

[11] Tiash, S.; Chowdhury, E. H. *Journal of Cancer Metastasis and Treatment* **2015**, *1*, 190.

Specially, EGFR (also known as human epidermal receptor, HER) comprise a family of receptors playing an important role in the pathogenesis of different cancers, e.g. breast, ovarian or gastric cancer. HER family comprises four different receptors, HER-1, HER-2, HER-3 and HER-4, also called ErbB1, ErbB2, ErbB3 and ErbB4, all of them present as monomers on the cell surface, with an extracellular ligand-binding region, a transmembrane lipophilic segment and a cytoplasmic tyrosine-kinase domain. Upon binding of the ligand, the receptors form homo- or heterodimers promoting their activation and releasing signals for proliferation, survival and differentiation of the cell. [11,12,13] Thus, the overexpression of HER receptors will enhance the stimulation of the cell division. As an example, HER-2 receptor (**Fig. 1.9**) has recently emerged as an important target for treatment of breast cancer due to its overexpression in up to 30% of these cancers. When the cytoplasmic tyrosine kinase is activated by phosphorylation, a cascade of intracellular signaling pathways is initiated, involving Ras-GTP, and activating mitogen-activated protein kinase (MAPK), phosphatidylinositol-4,5-biphosphate 3-kinase (PI3K) and protein kinase C (PKC). This results in the expression of cell-cycle progression, proliferation and survival genes through nuclear transcription factors activation. In addition, to the mitotic effects, HER-2 has been demonstrated to increase the secretion of other receptors as VEGFR, which stimulates the angiogenesis necessary for the progression of tumor growth.[12]

[12] Iqbal, N. *Mol Biol Int* **2014**, *852748*, 7.
[13] Subik, K.; Lee, J. F.; Baxter, L.; Strzepek, T.; Costello, D.; Crowley, P.; Xing, L.; Hung, M. C.; Bonfiglio, T.; Hicks, D. G.; Tang, P. *Breast Cancer* **2010**, *4*, 35.

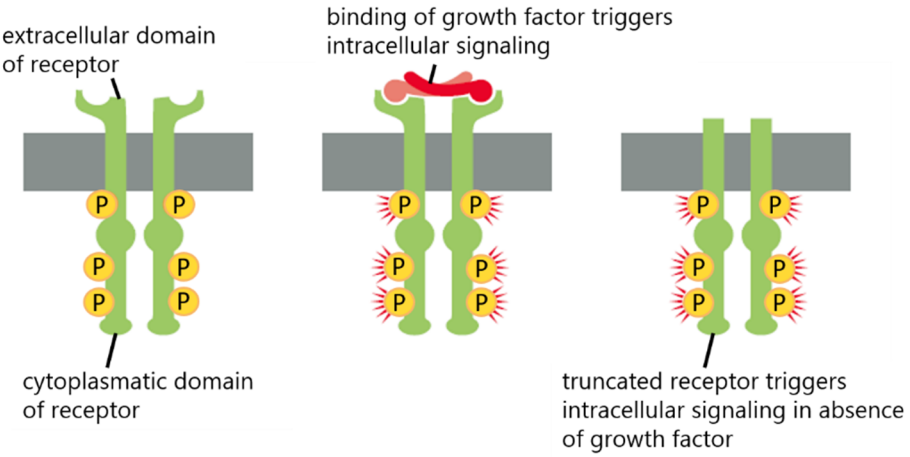

FIGURE 1.9 HER-2 receptor in its normal conformation and mutated in cancer.

(iii) Alteration of nutritional requirements

The alterations in the oncogenes and tumor suppressor genes confer most of tumors unique genetic characteristics with a vast heterogeneity. However, the resulting phenotypes have common features to consider, as altered metabolic activities adapted to facilitate the incorporation of nutrients needed to produce new cells. The reprogramming of bioenergetics or the enhancement of biosynthesis in the conventional metabolic pathways provide benefit to supply and fulfill the energetic demands from malignant cells. [1, 3, 5, 6, 7, 14, 15]

One of the classical examples of reprogrammed metabolic pathway in cancer is the aerobic glycolysis. In presence of oxygen, adult tissue cells oxidize sugars to generate available energy in ATP format through the glycolysis pathway, where a molecule of glucose is converted in simpler profitable metabolites for further catabolic and anabolic reactions. [1, 5, 7, 14, 15]

[14] DeBerardinis, R. J.; Chandel, N. S. *Sci Adv* **2016**, *2*.
[15] Martinez-Outschoorn, U. E.; Peiris-Pages, M.; Pestell, R. G.; Sotgia, F.; Lisanti, M. P. *Nat Rev Clin Oncol* **2017**, *14*, 11.

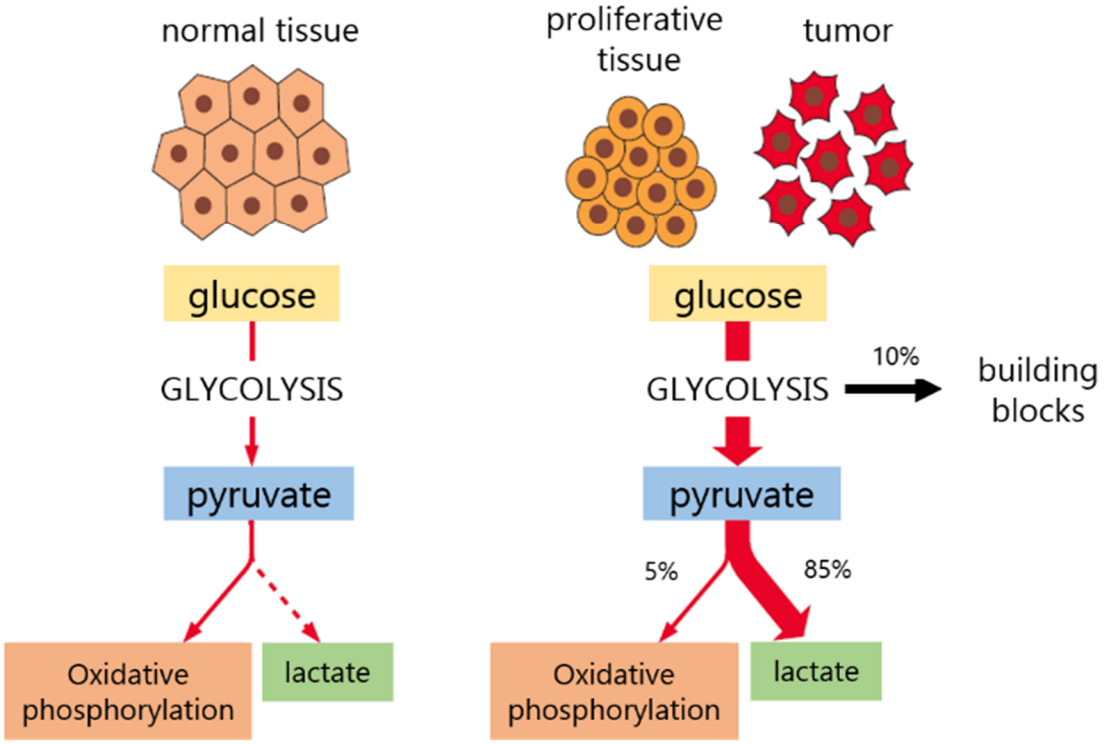

FIGURE 1.10 Schematic representation of glucose metabolism fate in normal tissues and in a proliferative tumor mass.

These biosynthetic or anabolic pathways are essential for cancer metabolism *as* enable cells to produce the macromolecules required for the replicative cell division during cell growth and tumor progression. In consequence, tumor cells display a high rate of glucose consumption, by its large importation from the extracellular space and its conversion through the glycolytic flux to intermediates that undergo aerobic and anaerobic transformations into ATP molecules (**Fig. 1.10**). [1] This effect, stated by Otto Warburg's, explains how tumor cells *can* metabolize glucose in a manner that differs from that of normal tissues cells. [1] This idea has already been validated in many human cancers with positron emission tomography (PET), using a

radioactive labeled glucose analog to image glucose uptake in tumors. [1, 14, 15, 16, 17]

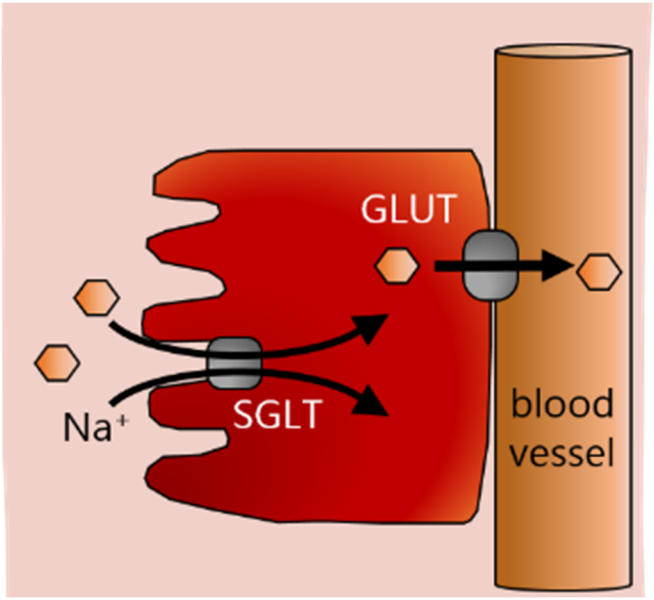

FIGURE 1.11 Glucose transporters SGLT and GLUT act importing sugars.

Since glucose is the most abundant nutrient in blood, its importation into cells to afford their energetic necessity should be assured. [1,7] Glucose transport across the cell membrane occurs via two different classes of hexose transporters: sodium-dependent glucose transporters (SGLT) family and facultative *glucose transporters* (GLUT) family. [7] SGLT are a type of symporters able to transport sugar against the concentration gradient using a Na^+ gradient maintained by a sodium-pump (**Fig. 1.11**). Specifically, SGLT1 is found overexpressed in several cancers (*e.g.* colorectal, head and neck and prostate) normally in association to EGFR protein, promoting not only large glucose uptake but also signal transduction cascades that lead to cell proliferation. In contrast, GLUT transporters are transmembrane proteins that

[16] O'Neil, R. G.; Wu, L.; Mullani, N. *Mol Imaging Biol* **2005**, *7*, 388.
[17] Vander Heiden, M. G.; Cantley, L. C.; Thompson, C. B. *Science* **2009**, *324*, 1029.

allow energy-independent transport of glucose across the plasma membrane down the concentration gradient. To note, increased levels of GLUT1 mRNAs and GLUT protein have been isolated in extracts of diverse human cancers (*e.g.* pancreatic, breast, lung, renal) due to its upregulation during oncogenesis of tissues to permit higher rates of sugar importation. [17, 18, 19]

On the other hand, cancer cells overcome the growth factor dependence by acquiring mutations that alter signaling pathways promoting cell survival and fuel cell growth. One example is the gain of function of oncogene c-MYC by its gene amplification, chromosomal translocation or single-nucleotide polymorphism which results in large amount of product. c-MYC acts as transcription factor for the expression of many genes that support and enhance anabolic growth, glycolysis, fatty acid synthesis or mitochondrial metabolism (**Fig. 1.12**). [14, 15, 17]

[18] Szablewski, L. *Biochim Biophys Acta* **2013**, *2*, 164.
[19] Macheda, M. L.; Rogers, S.; Best, J. D. *J Cell Physiol* **2005**, *202*, 654.

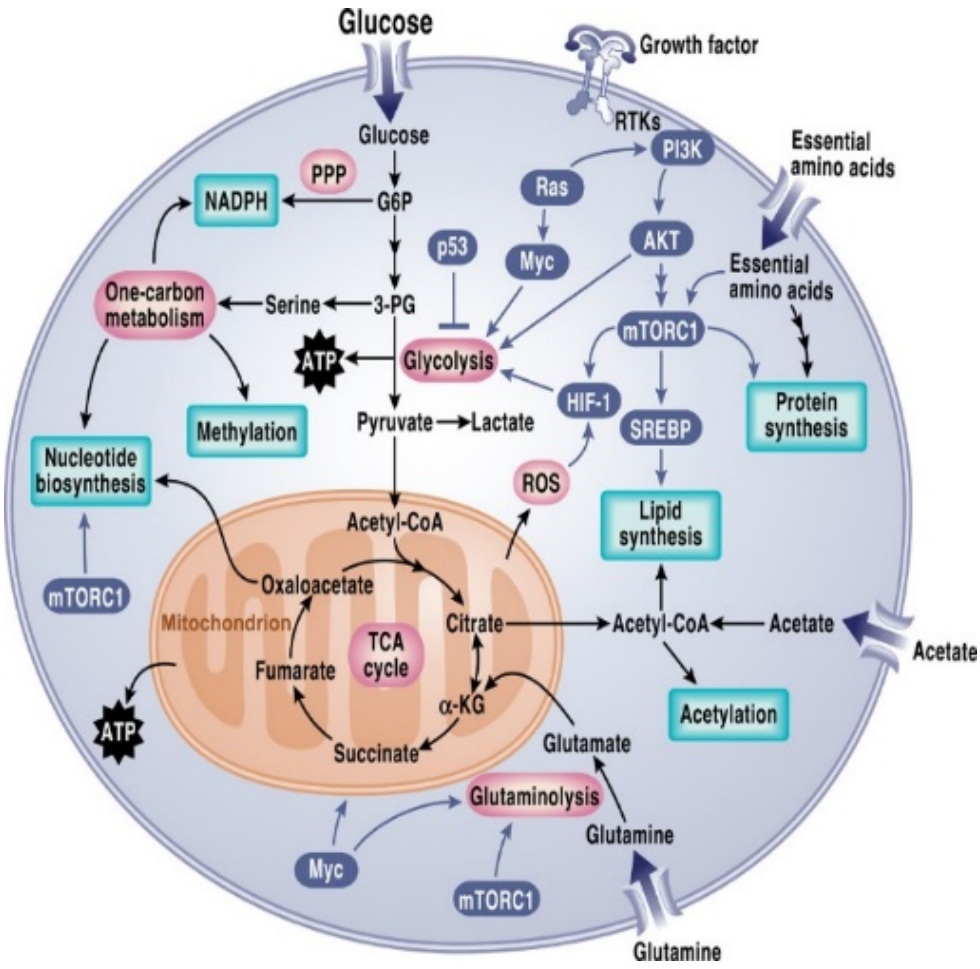

FIGURE 1.12 Schematic representation of crosstalk between different pathways involved in cancer progression.

Cancer can spread to other tissues

An abnormal cell that grows and proliferate out of control will build-up, at the end, a solid mass of numerous cells, more commonly known as tumor or *neoplasm*. As long as the number of cells increases they adhere and communicate each other through specialized intercellular junctions generating a benign tumor, without the ability to invade other surrounding tissues. [1, 3] Such neoplasms tend to grow in the inner part of the tissue in frontier with the epithelial barrier. In such cases, the local removal of the mass can serve to achieve a complete cure. However,

malignancy appears when cancer cells are able to break these junctions (**Fig. 1.13**), entering blood or lymphatic vessels and form secondary tumors in other sites of the body. This complex process known as *metastasis* is responsible of 90% of deaths by cancer. Metastasis involves different steps in which the aberrant cells need to switch from their original tissue phenotype to the mesenchymal-like one and gain motility through the change in their gene expression. [1, 3, 20]

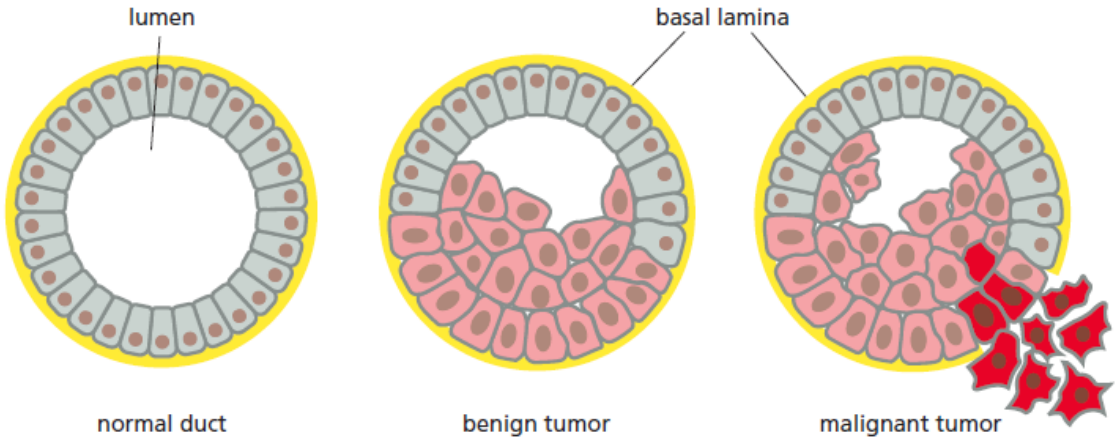

FIGURE 1.13 Schematic representation of benign and malignant tumor and the ability to invade tissues.[1]

Epithelia is a single cell monolayer or multilayer tissue present in most of surfaces of the organs and body accomplishing various functions as barrier for protection, absorption and transport of molecules. Epithelial tissue suppose the first important physical obstacle that tumor cells should overcome to metastasize and move to other sites of the body. [1] In fact, most common types of cancer (up to 80%) arise from epithelial cells, known as *carcinomas*, since they are more exposed to external physic and chemical damage to become aberrant. . In that way, it is easier for the cells to overpass the barrier and jump to blood vessels since they are part of it. [1]

[20] Gupta, G. P.; Massague, J. *Cell* **2006**, *127*, 679.

(i) Epithelial-mesenchymal-transition mechanism

Metastasis basically involves the movement of cells from one site to another (**Fig. 1.14**). This cell migration requires several changes in cell phenotype apart of its removal from the primary tumor. The activation of a series of specific transcription factors (as Snail, Twist and Slug) and the repression of the adhesion molecules expression (such as integrins) confers motility to the cells, in a broad process known as *epithelial-mesenchymal-transition* (EMT). [1, 20, 21]

Key events dictate the EMT, starting from the dissolution of the epithelial cell-cell junctions, the reorganization of cytoskeletal architecture and cell shape changes, the gaining in cell motility, the repression of epithelial genes expression and the activation of genes to define mesenchymal phenotype.[1, 21, 22]

Break of cellular adhesions. As mentioned, specialized cell surface adhesion molecules guarantee tissue integrity maintaining cell-cell interactions (*e.g.* tight junctions, desmosomes or gap junctions). In the first steps of EMT, the adhesiveness of cells is diminished and these cell contacts are disassembled or degraded due to downregulation of expression of cell junction proteins. [1, 20, 21] In E-cadherin, a cell membrane integrin which plays an important role in adhesion, its expression is repressed during EMT program by the binding of Snail transcription factor to the promoter region of E-cadherin gene. Independently, TWIST transcription factor acts recruiting histones to repress the expression of E-cadherin and activating N-cadherin promoters. In consequence, E-cadherin ligand, β-catenin, can no longer interact with it. Other factors, as desmosomes and gap junctions, disrupt their integrity by

[21] Lamouille, S.; Xu, J.; Derynck, R. *Nat Rev Mol Cell Biol* **2014**, *15*, 178.
[22] Joosse, S. A.; Gorges, T. M.; Pantel, K. *EMBO Molecular Medicine* **2015**, *7*, 1.

decreasing the connexin-protein levels leading to a loose of cell contacts. [21, 23, 24]

Cytoskeletal changes and gain of motility. The movement of cells from the origin is not achieved only by their disassembly from the tissue. Changes in cell morphology and reorganization of intracellular architecture are needed to enable migration.[1, 20, 21] Basically, actin fibers forming the cell cytoskeleton polymerize resulting in actin-rich membrane projections which elongate cell shape and provide contractility. These dynamic changes are mainly regulated by the action of Ras-homolog associated-kinase (ROCK) activated during EMT process. ROCK activates myosin by phosphorylation enhancing contractility following the activation of RAC1 and CDC42 transcription factors which activates, in turn, targets involved in the formation of membrane protrusions, cell spreading and motility. [21, 22]

Life in transit to distant organs. Once malignant cells have gained the ability to invade the circulatory system and disseminate to distant organs, they must overcome and survive to several stresses, as physical damage from hemodynamic forces and the action of immune system. Thus, metastasis depends on the direct interaction between tumor cells and the hostile microenvironment within the bloodstream, involving blood cells (*e.g.* lymphocytes and macrophages), components of the coagulation system (*e.g.* platelets) and other stromal cells (*e.g.* endothelial cells and fibroblasts).[1, 21, 22]

For over a century, the tendency of malignancy to induce a hypercoagulable state in the hosts has been clinically observed. This makes evident a relationship between cancer and coagulation. Mainly, platelets play an important role in metastasis, protecting tumor cells from action of immune

[23] Batlle, E.; Sancho, E.; Franci, C.; Dominguez, D.; Monfar, M.; Baulida, J.; Garcia De Herreros, A. *Nat Cell Biol* **2000**, *2*, 84.
[24] Cano, A.; Pérez-Moreno, M. A.; Rodrigo, I.; Locascio, A.; Blanco, M. J.; del Barrio, M. G.; Portillo, F.; Nieto, M. A. *Nature Cell Biology* **2000**, *2*, 76.

natural killers by their direct interaction with them. Activated platelets and leukocytes show an increase in adhesiveness by expression of a family of transmembrane cell adhesion molecules, selectins. These lasts, contain a conserved lectin domain able to recognize and bind glycoconjugates present on other cells as on metastatic tumor cells. Thus, they can directly bind with tumor cells forming heteroaggregates and transport cancer cells through the circulation acting as a shield to the immune system. During transport, platelet-heteroaggregates can induce the activation of receptors expression on tumor cells, such as protease-activated receptor (PAR) promoting the release of tissue factor protein and enhancing a coagulant activity needed for extravasation from circulation. [22-25, 26, 27, 28]

Extravasation and new colonization. Platelets not only protect tumor cells during their travel but also assist the attachment to wall vessels, the exit from bloodstream and the entrance in target tissues. Circulating heteroaggregates interact with endothelial cells of wall vessels through adhesion receptors expressed on platelets and leukocytes, in transient interactions until tumor cell adhere to some point within the vasculature. As platelets become activated through coagulation cascade, they release granules, microparticles, cytokines and other factors, as platelet-derived growth factors (PDGF), tumor growth factor (TGFβ), insulin-growth factor (IGF) or VEGF, that act modulating de permeability of vessels. How tumor cells scape from circulation to specific tissues may differ on the type of cancer, but in general the secretion of VEGF leads to a vascularization of vessels allowing a considerable growth of tumor within the intravascular space until physical lesion of the vessel occurs.

[25] Mlecnik, B.; Bindea, G.; Kirilovsky, A.; Angell, H. K.; Obenauf, A. C.; Tosolini, M.; Church, S. E.; Maby, P.; Vasaturo, A.; Angelova, M.; Fredriksen, T.; Mauger, S.; Waldner, M.; Berger, A.; Speicher, M. R.; Pagès, F.; Valge-Archer, V.; Galon, J. *Science Translational Medicine* **2016**, *8*, 327ra26.
[26] Gay, L. J.; Felding-Habermann, B. *Nat Rev Cancer* **2011**, *11*, 123.
[27] Smith, H. A.; Kang, Y. *J Mol Med* **2013**, *91*, 411.
[28] Mohme, M.; Riethdorf, S.; Pantel, K. *Nat Rev Clin Oncol* **2017**, *14*, 155.

Additionally, endothelial cells expose to VEGF activate the expression of Src kinase family, inducing the disruption of cell-cell junctions and in consequence, facilitating the extravasation. [20, 21] After colonization, tumor cells can revert the mesenchymal phenotype to epithelial state leading to the formation of secondary tumors phenotypically similar to the original one. [21, 28]

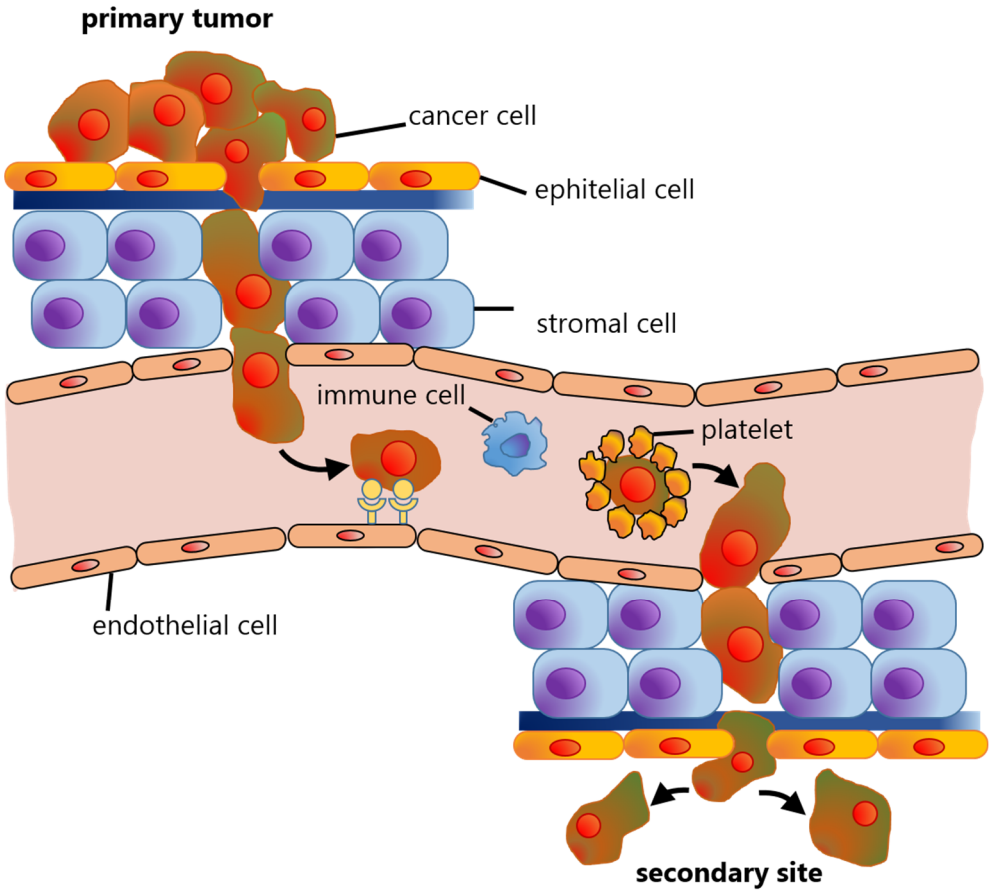

FIGURE 1.14 Schematic representation of a metastatic process involving the gain of intravasation capability to travel within the blood stream and to exit to secondary sites evading immune response.

Cancer trail in blood

A cancerous tumor typically contains millions or even billions of cells concealing large variety of genetic mutations leading them to grow, divide and invade neighboring tissues. [1] Some cells at the edges of tumor can move away by simple disruption from the mass or metastasize within the bloodstream, as have been previously discussed. But not only parts or entire cells can be found in circulation, but also other material (**Fig. 1.15**) can be encountered result of a constant release from the tumor. DNA, RNA, proteins or vesicles as well as circulating cells derived from tumors have been isolated in blood samples and gained relevance in clinical oncology due to their potential as biomarkers with valuable complementary information. [29, 30, 31]

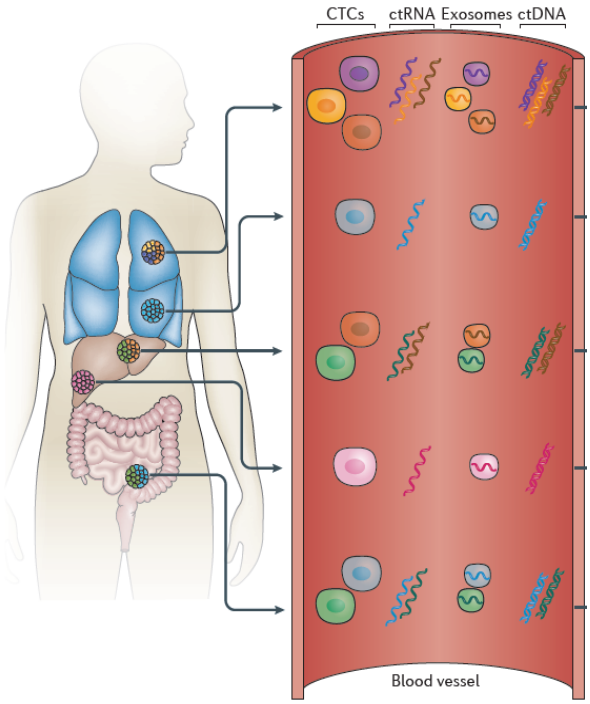

FIGURE 1.15 Schematic representation of different source of tissue-specific information that can be found floating in bloodstream.[30]

[29] Chi, K. R. *Nature* **2016**, *532*, 269.
[30] Siravegna, G.; Marsoni, S.; Siena, S.; Bardelli, A. *Nat Rev Clin Oncol* **2017**, *14*, 531.
[31] Perakis, S.; Speicher, M. R. *BMC Medicine* **2017**, *15*, 75.

(i) Circulating tumor cells

Most obvious tumor-released material that can be found in the bloodstream are entire cells. *Circulating tumor cells* (CTCs) are cancer cells that have intravasated or been shed from the primary tumor or metastatic lesions and remain lost into the bloodstream.[32, 33, 34] They were reported for the first time in 1869, and isolated in blood from cancer patients as single cells or forming clusters of 2 to more than 50 cells. [35] Since CTCs come directly from tumor mass, recently have gained relevance as they hold important information about the tumor. Their presence and further molecular characterization can serve for diagnosis and as a predictive value of response to a therapy, since the non-invasive method for their isolation permits several rounds of sample examinations and therapy monitoring in time. [32, 33]

Despite several advantages that suppose CTCs as markers of cancer progression, the tiny amount of these specimens in blood turn their analysis in a challenging work to achieve. It has been reported an abundance of CTCs of approximately 1 cell per $1x10^9$ white blood cells in patients with a mestastatic cancer. [29-31] Thus, a lot of efforts have been focused on their enrichment and capturing using specific surface markers, *e.g.* EpCAM membrane receptor, or other physical properties, *e.g.* buoyancy or size. Slightly larger than normal blood cells, CTCs can be isolated from a blood sample by gradient centrifugation in the same cell fraction as white blood cells. Once isolated, their enumeration can be used as a barometer to measure level of aggressiveness of a particular cancer and to discern the phenotypical pattern of tumor origin. [36, 37] More, by disruption of CTCs tumor

[32] Pantel, K.; Alix-Panabieres, C. *Nat Rev Gastroenterol Hepatol* **2017**, *14*, 73.
[33] Williams, S. C. *Proc Natl Acad Sci U S A* **2013**, *110*, 1304186110.
[34] Pantel, K.; Speicher, M. R. *Oncogene* **2015**, *35*, 1216.
[35] Hong, Y.; Fang, F.; Zhang, Q. *Int J Oncol* **2016**, *49*, 2206.
[36] Qian, W.; Zhang, Y.; Chen, W. *Small* **2015**, *11*, 3850.
[37] Gao, W.; Farokhzad, O. C. *Angew Chem Int Ed Engl* **2011**, *50*, 7220.

data can be liberated and with the emerging next generation sequencing (NGS), cell genetic material as DNA or RNA can be inspected to gain insight into cancer genetics. [38]

(ii) Circulating tumor nucleic acids

Aside from intern cellular genetic material, small portions of cell-free nucleic acids (cfNA) can be found floating into the bloodstream, product of a constant release from tissues. [29, 30, 38, 39] Actually, these cfNAs are even present in fluids from healthy people and can come from any part of the body. In cancer patients, Stroun and colleagues reported in 1989 that at least some fraction of cfNA found in plasma is originated from cancer cells. These *circulating tumor-associated nucleic acids* in DNA (ctDNA) or RNA (ctRNA) forms seem to be released into the blood from a combination of secretion and apoptosis or necrosis of the cancer cells conforming the tumor mass, which ends destructing the cell integrity and liberating their content. Despite tiny amount from total cfDNA, only <1% in some cancers, ctDNA has been demonstrated as a potential cancer biomarker for prognosis since by detecting and quantifying the concentration of ctDNA in plasma it is possible to directly correlate with the tumor size and disease stage. Additionally, messenger ctmRNA (ctmRNA) has been identified in the blood circulation of patients with solid tumors. ctmRNA analysis permits the determination of tumor-specific gene expression profiles as they carry post-translational epigenetic alterations not considered in DNA. [29, 31, 38, 39]

[38] Chen, Y. H.; Hancock, B. A.; Solzak, J. P.; Brinza, D.; Scafe, C.; Miller, K. D.; Radovich, M. *NPJ Breast Cancer* **2017**, *3*, 017.
[39] Wan, J. C. M.; Massie, C.; Garcia-Corbacho, J.; Mouliere, F.; Brenton, J. D.; Caldas, C.; Pacey, S.; Baird, R.; Rosenfeld, N. *Nat Rev Cancer* **2017**, *17*, 223.

(iii) Exosomes

A third type of target that can be found in blood transporting tumor information involves *exosomes*, a tiny membrane vesicles that are shed from different living cells including cancer cells. Ranging sizes from 30 to 200 nm, they content DNA, mRNA and proteins from the cells of origin and are continuously secreted in thousands supposing an important source of tumor-specific data. [29-31, 40]

The analysis of enumerated tumor material supposes new blood-based diagnosis approaches, termed as **liquid biopsy** in which by using minimally invasive methods as the sampling of blood or other body fluids (*e.g.* urine, saliva, and cerebrospinal fluid), it is possible to give clinical benefits as earlier diagnosis and prognosis, improvement of treatment selection and monitoring disease easily in time.[30]

Thus, noting the clear role of single cells and other tumor-associated material as nucleic acids or proteins as markers of cancer disease progression, *ex vivo* methods for the analysis of these biological specimens are required to accomplish diagnostic and prognostic in cancer. Several optical techniques are available and largely explored to identify and characterize probes of human diseases, including imaging and spectroscopy.

[40] Guo, W.; Gao, Y.; Li, N.; Shao, F.; Wang, C.; Wang, P.; Yang, Z.; Li, R.; He, J. *Oncol Rep* **2017**, *38*, 665.

2 Light in biomedicine

The use of the electromagnetic spectrum (**Fig. 1.16**) has provided a set of photonic tools for manipulating, detecting and interacting with biological systems.[41] Specially, the portion of ligth included in the spectral window between 1 μm to 100 nm (i.e., near-infrared, NIR; visible; and, ultraviolet, UV), is consistently used for diagnosis and therapy in biophotonics. [41,42] This region, can be controllably used to explore tissues or cellular structures and functions with high sensitivity and precision in a non-damaging way, turning light into a unique tool for modern medicine.[41] Exploring fundamental life processes or recognizing changes, even before symptoms appear, at the cellular or molecular level are examples of how the use of light can help to prevent and treat diseases.[41-43]

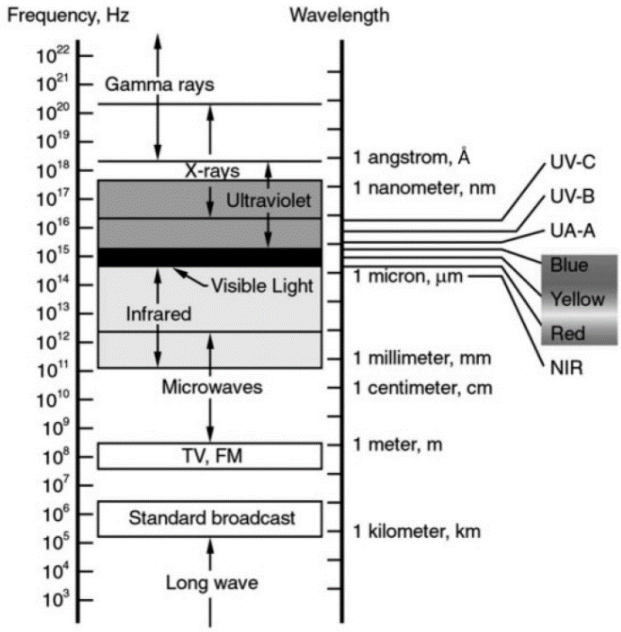

FIGURE 1.16 Electromagnetic spectrum. Light is presented as the region from Infrared to Ultraviolet.[41]

[41] Mobley, J.; Vo-Dihn, T. In *Biomedical Photonics Handbook*; CRC Press: **2003**; Vol. 1.
[42] Schmitt, M.; Mayerhöfer, T.; Popp, J. In *Handbook of biophotonics Vol 1: Basics and Techniques*; 1 ed.; Wiley-VCH, Ed. **2011**; Vol. 1, p 112.
[43] Prasad, P. N. In *Introduction to biophotonics*; Wiley Interscience: **2003**; Vol. 1, p 92.

The use of the electromagnetic spectrum (Fig. 15) has provided a set of photonic tools for manipulating, detecting and interacting with biological systems.[44] Specially, the portion of ligth included in the spectral window between 1 μm to 100 nm (i.e., near-infrared, NIR; visible; and, ultraviolet, UV), is consistently used for diagnosis and therapy in biophotonics. [41] Light-matter interaction has been deeply studied in fundamental photophysics to understand how an incident photon on a molecule can be absorbed and the electronically excited molecule can return to its lower energy state through radiative or non-radiative processes.[43]

Generally, when a source of monochromatic light (*e.g.* laser) interacts with mater, different events can take place: reflection or transmission, absorption or scattering.[43] As presented in **Fig. 1.17**, part of the light is unable to penetrate the material and is consequently *reflected* back with a certain angle (θr), equal to the angle of incidence (θi). The other part of light which is not reflected can then permeate and be *transmitted* with a certain angle (θt) which differs from the incident, for example passing through a transparent material.[45] These principles have been exploited in the development of conventional optical bright field microscopes that can operate to visualize specimens in either transmission or reflection of white light, or other spectroscopic techniques as reflectance and transmittance spectroscopy.

[44] Mobley, J.; Vo-Dihn, T. In *Biomedical Photonics Handbook*; CRC Press: **2003**; Vol. 1.
[45] Schmitt, M.; Mayerhöfer, T.; Popp, J. In *Handbook of biophotonics Vol 1: Basics and Techniques* **2011**, p 112.

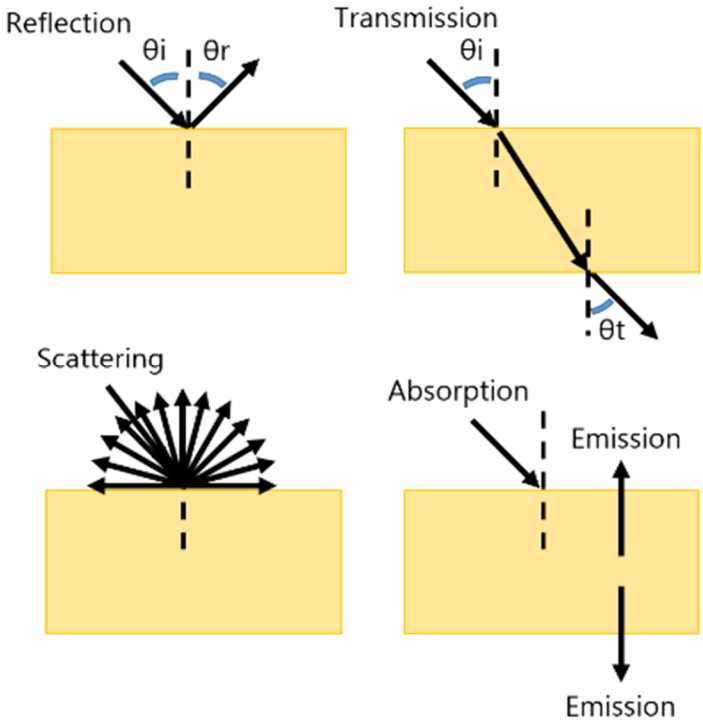

FIGURE 1.17 Fates of the light after interacting with the materia.

Interaction of light with mater can generate other light which is not reflected and not transmitted, but it is absorbed or scattered by the material. Molecular species forming the biological material, collect photon's energy and shift then from an internal lower and stable energy state (ground state, S_0) to a higher energy transition state by a process known as excitation. If the energy of the incident photon is enough to fulfill the energetic gap between the ground and an excited state (S_1) then molecule undergoes an *absorption* or *inelastic scattering* process. On the contrary, if the energy does not allow to complete the energetic requirement then *elastic scattering* occurs (**Fig. 1.18**). [46]

[46] Valeur, B. In *Molecular fluorescence: principles and applications* **2001**, p 3.

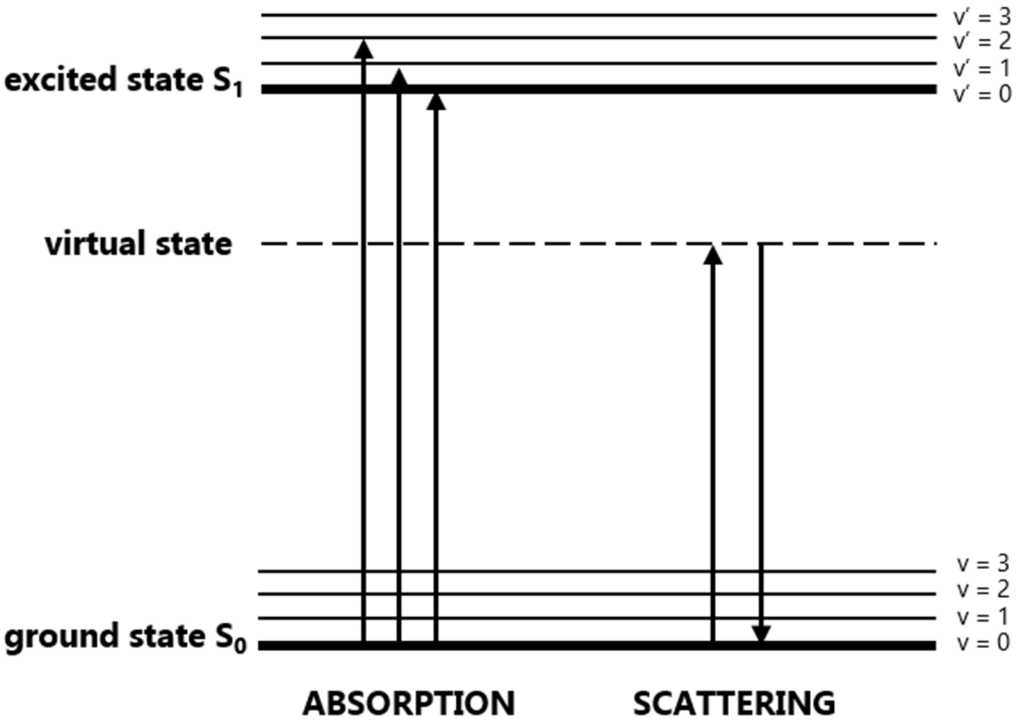

FIGURE 1.18 Jablonski diagram of absorption and scattering mechanisms.

3 Fluorescence

Certain molecules, *e.g.* dyes or chromophores, can absorb a photon of light promoting an electron from a molecular orbital at the ground state S_0 to an unoccupied orbital with higher energy S_n (**Fig. 1.19**).[45] The resulting excited state can be a singlet, when the spin of the excited electron remains unchanged, or a triplet, when undergoes conversion to parallel to the non-excited electron. The excited states in triplet are presented as T_n and show lower energy than the singlet states of the same configuration.[46]

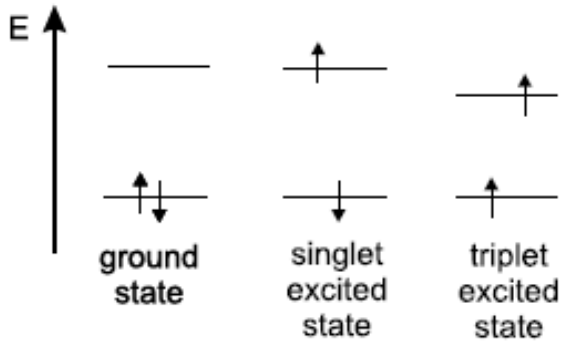

FIGURE 1.19 Electronic configuration possibilities upon excitation of a molecule.[48]

Regardless the type of transition state, excitation results in a short-time process causing a non-equilibrated electronic configuration of the molecule that rapidly returns to the ground state by its relaxation or deactivation.

The molecular relaxation of electronically excited species to the S_0 state results in emission of photons, a process known as *luminescence*.[47,48] Particularly, depending on the nature of the excitation, different types of luminescence can be described: electroluminescence when the excitation comes from an electric field,

[47] Cullum, B. M.; Vo-Dihn, T. In *Biomedical Photonics Handbook* **2003**, p 718.
[48] Schmitt, M.; Mayerhöfer, T.; Popp, J. In *Handbook of biophotonics Vol 1: Basics and Techniques* **2011**, p 182.

chemoluminescence and bioluminescence resulting from chemical or biological processes, and photoluminescence when the excitation is product of a photon absorption. Two main particular cases of photoluminescence exist as a function of how the photon emission occurs: fluorescence and phosphorescence. [49]

As presented in **Fig. 1.20**, if the excitation through absorption occurs to the electronic level S_2, a non-radiative internal conversion (IC) to the S_1 level is normally the dominating mechanism. IC process is then followed by the return of molecule to the electronic ground state S_0 through the emission of a photon radiatively. This emission of a photon from one excited state to another of the same spin multiplicity (S) is known as *fluorescence*. Alternatively, the excitation from S_1 can pass to a state of different spin T_1 through another non-radiative process called intersystem crossing (ISC). At last, relaxation occurs by turning to the T_0 state by a weaker emission process known as *phosphorescence*. [48]

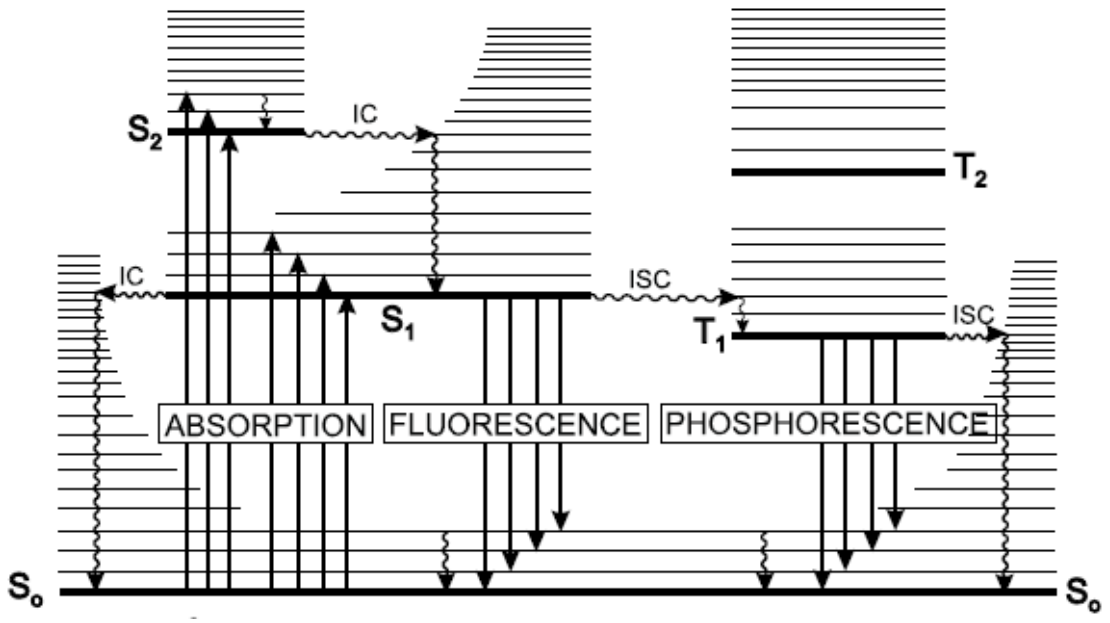

FIGURE 1.20 Jablonski diagram of the possible relaxation mechanisms after absorption. [46]

[49] Valeur, B. In *Molecular fluorescence: principles and applications*, p 21.

In particular, fluorescence supposes one of the most widespread used technique in biophotonics since allows for multiple of options to investigate from tissue and cellular structures to single molecules. Its detection and characterization offers a virtual background free with unique sensitivity, specificity and versatility useful to gain information in life sciences and medicine. Analysis of natural autofluorescence of biomolecules or the introduction of fluorescent probes to selectively interact with a target can allow for the identification and/or localization of that target within a cell using fluorescence microscopy or other spectroscopic approaches, *e.g.* flow cytometry.[47,48]

Absorption and emission spectra

The fluorescence spectrum is characteristic for each compound and can serve for its identification. Fluorescence emission spectrum is a direct result from the radiative decay S_n level to S_0, exhibiting the vibrational frequencies of the molecule at the ground state.[43,47,48] On contrary, the absorption spectrum is due to frequencies at the excited state after excitation with a light source, normally conventional lamps or lasers. For pure molecules, absorption and emission spectra are mirror images when the vibrational patterns at S_0 and S_1 are similar (**Fig. 1.21**). Since the emission suppose a loose of energy, the resulting emission bands are red-shifted to higher wavelengths in comparison to excitation spectrum. This shift between the peaks of absorption and emission are so-called Stokes shifts and suppose a measure of the relaxation process.[47,48]

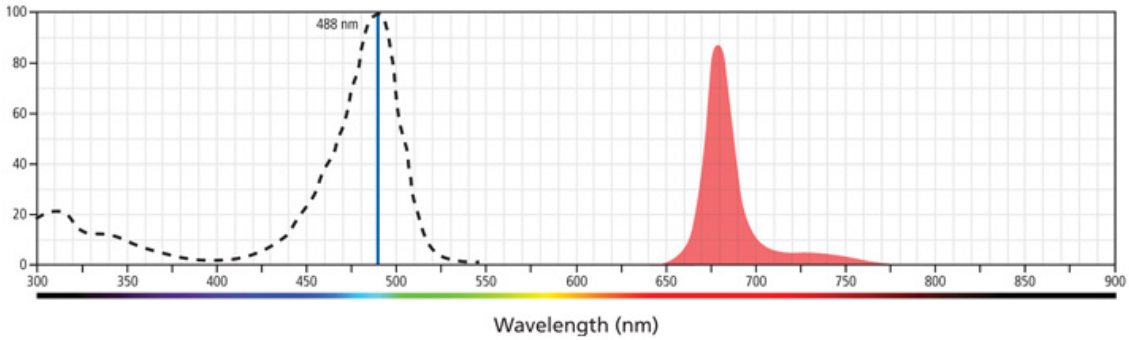

FIGURE 1.21 Fluorescence excitation and emission spectrum for a fluorescent dye. 488 nm laser is presented as blue line.

A maximum of excitation, and consequently, a maximum of fluorescence emission can be extracted from the characteristic spectrum and can serve for the selection of appropriate excitation sources (*e.g.* lasers with similar wavelengths as maximum) and emission collection filters (*e.g.* filters able to cut-off only the emission maxima) in fluorescence-based techniques.

Fluorescence quantum yield

Fluorescence emission has to compete favorably with intersystem crossing or deactivation through phosphorescence, consequently determining the intensity of the emitted fluorescence. It is possible to quantify the amount of photons that relax emitting fluorescence to the total photons absorbed, a parameter named as quantum yield (ϕ). In the most efficient case, all excited photons can undergo fluorescent emission in absence of any non-radiative decay supposing a quantum yield ϕ equal to 1. Therefore ideal fluorophores to be used in fluorescence techniques should present a quantum yield close to 1.[47]

Eq. 1 $$\phi = \frac{\text{number of emitted photons}}{\text{number of absorbed photons}}$$

Fluorescence-based techniques

(i) Fluorescence microscopy

Biomedical imaging suppose one of the most useful and reliable tools in healthcare for diagnosis and treatment of diseases. Herein, microscopy represents the essential technique for bioimaging of molecules, structures or living cells and the introduction of fluorescence has improved the resolution and sensitivity of conventional microscopes based on transmission or reflection.[50] Mainly, fluorescence microscopes differ from standard microscopes by the light of source used that produces UV-visible light, normally a xenon or mercury lamp. They follow epifluorescence excitation using a dichroic beam splitter that filters UV-light at a given wavelength that can be selected depending on the maximum excitation of the molecule in the fluorescence spectrum. The whole specimen is illuminated to absorb the excitation light through an objective lens that also collects the emitted fluorescence for imaging after its filtration at wavelengths close to the emission maximum.[49,51] In that way, observer visualize only the part of the specimen which is fluorescing by eye, a photographic film or a CCD camera (**Fig. 1.22**). Fluorescence microscopy gives large versatility to analyze several types of biological material but importantly, material depth suppose an obstacle for bioimaging. Generally, the depth field of an epifluorescence

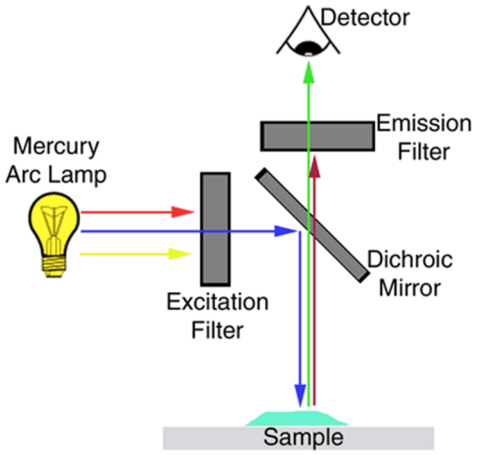

FIGURE 1.22 Schematic representation of a fluorescence microscope.

[50] Prasad, P. N. In *Introduction to biophotonics* **2003**, p 219.
[51] Bearman, G.; Levenson, R. In *Biomedical Photonics Handbook* **2003**.

microscope ranged from 2-3 μm and the maximal resolution to 0.2-0.3 μm using UV-visible radiation.[50]

(ii) Laser Scanning Confocal Microscopy

To overcome this major drawback of epifluorescence microscopy, thicker specimens (*e.g.* cancer cells are 20 μm in depth) can be analyzed using improved confocal microscopy. In specimens with thickness greater than 3-5 μm, most of the light is coming from regions that are out of the focused plane, generating blurred and non-defined images. Confocal microscopy overcomes this problem by using a confocal aperture or pinhole that transforms light path in a beam which eliminates out of focus background contributions. Contrary to epifluorescence microscopy, confocal mode uses laser as source of excitation and vibrating mirrors that allow the laser for scanning (**Fig. 1.23**). In this way, the laser beam spots on a section of the specimen and scans across it in all planes x, y and z introducing the capability of virtually constructing 3D images and enhancing the limit of resolution to 0.4-0.8 μm.[52,53,54]

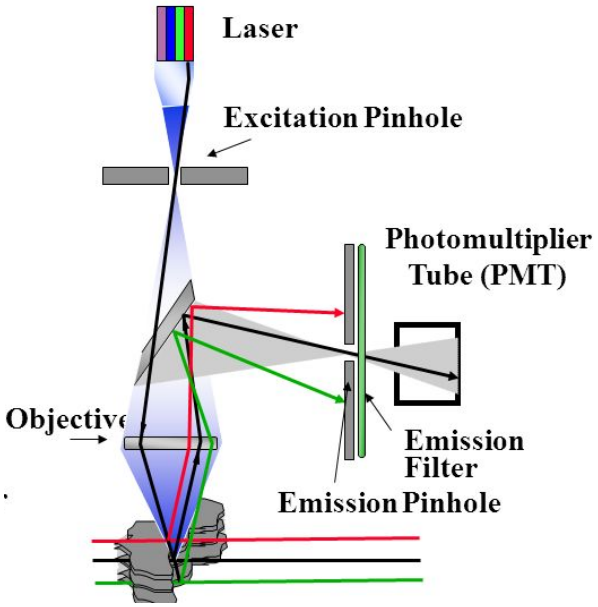

FIGURE 1.23 Schematic representation of a laser scanning confocal microscope.

[52] Inoué, S. *Handbook of Biological confocal microscopy*, **2006**.
[53] Wilson, T. In *Biomedical photonics handbook* **2003**.
[54] Voss, A.; Feller, K.-H.; Beckmann, D. In *Handbook of biophotonics: Basics and Principles* **2011**; Vol. 1, p 212.

(iii) Flow cytometry

Apart of microscopic techniques to visualize biological specimens, other fluorescence-based approaches are available for the analysis of single particles without necessity of imaging. One largely exploited and potential technique for the analysis of cells or other biological assemblies is flow cytometry.[55] The term *cytometry* refers to the analysis of physicochemical properties of cells, that modulate how they optically response to light, providing a set of parameters characteristic of each type of cell.[54,56] Then, depending on the parameters they show it is possible to identify and quantify cell types and correlate them with specific pathological conditions. Basically, flow cytometry is similar to microscopic techniques since a light source excites the specimen in a single point (such as in confocal microscopy) and the emitted light is collected using filters. But, instead of a laser moves scanning the cells to image them, cells flow one by one within a stream line of fluid, in time. This fact enables the possibility of analyze one individual cell at a time, reaching the analysis of up to 75,000 cells per second.[55,57]

[55] Shapiro, H. M. In *Practical Flow Cytometry* **2005**; Vol. 1, p 61.
[56] Prasad, P. N. In *Introduction to biophotonics* **2003**, p 390.
[57] Mandy, F.; Varro, R.; Recktenwald, D. In *Biomedical Photonics Handbook* **2003**; Vol. 1, p 635.

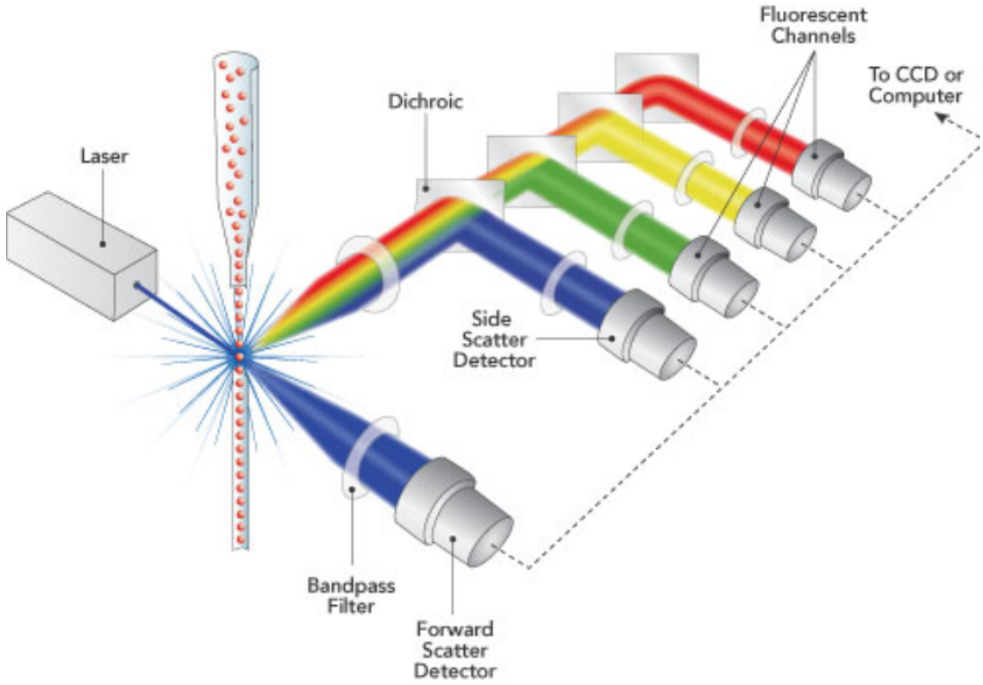

FIGURE 1.24 Schematic representation of optical and fluidic parts of a flow cytometer.[56]

To perform optical measurements of cells or particles from 50 μm to submicron size, a laser light beam intersects with the fluid stream, where the targets are located. The emitted light is collected by a train of optical ports that separate different optical responses or parameters (**Fig. 1.24**). These parameters are based on the pattern on how cells scatter the light, (i) forward scattering (FSC) which gives information about relative sizes, (ii) side scattering (SSC) which informs about granularity, and on various (iii) fluorescence signals defining the cell population.[55]

Flow cytometry has been widely used in the identification and discrimination of cell populations within a complex mixture of particles. To highlight, one application of flow cytometry in biomedicine is to classify blood cells types exploiting the use of antibodies carrying fluorescent molecules, known as *immunophenotyping*. Here, light scattering in forward and side, FSC and SSC, are used to select a cell population with similar patterns (**Fig. 1.25**) for further analysis of fluorescence. If the fluorescence is

present on the population means that the fluorescent antibody successfully recognized the cell, evidencing the type of cell in question.[55,56,58]

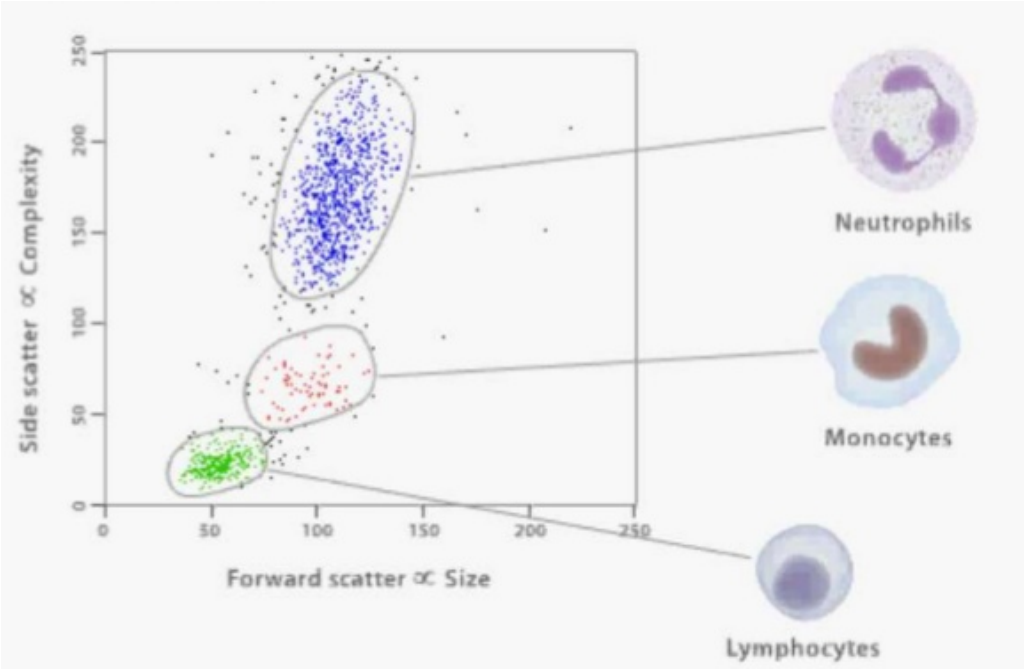

FIGURE 1.25 Typical 2D plot of flow cytometry for three blood cell populations. Forward scattering and side scaterring are presented in x and y axis, respectively.

[58] Brown, M.; Wittwer, C. *Clinical chemistry* **2000**, *46*, 1221.

4 Surface enhanced Raman scattering spectroscopy

As mentioned, a part of absorption when light interact with material, scattering mechanism can take place. Contrary to absorption, in scattering the photons do not have enough energy to match the gap between two energy levels of the molecule and consequently, electrons move to an energetic virtual state. For pure molecules, absorption and emission spectra are mirror images when the vibrational patterns at S_0 and S_1 are similar. [59,60]

Two different types of scattering of photons can occur depending on the interaction that incident light undergoes with a molecule. If the energy of the incident photons remains unaltered after distortion of electron cloud of the molecule, then the scattered photons contain the same energy as the incident photons and molecule relaxes without noticeable changes in energy. This elastic process is known as elastic scattering or *Rayleigh scattering*.[58] Other fraction of photons can be inelastically scattered if the energy of the scattered photons changes from the incident photon due to a transfer or energy between photons and the vibrational states of the molecule. This process is termed as inelastic or *Raman scattering* and the resulting scattered photons can gain energy from the molecule (anti-stokes scattering) or lose energy that is transfer to molecule (stokes scattering).[58-61]

In Raman stokes scattering, scattered photons lose energy by its transference to the molecule (**Fig. 1.26**), which is promoted from a low energy vibrational mode (v=0) to a higher energetic vibrational state (v=1). Consequently, these scattered

[59] Mahadevan-Jansen, A. In *Biomedical photonics Handbook* **2003**; Vol. 1, p 790.
[60] Smith, W. E.; Dent, G. *Modern Raman Spectroscopy: A pratical approach*; Wiley, **2005**; Vol. 1.
[61] Popp, J.; Tuchin, V.; Chiou, A.; Heinemann, S. In *Handbook of Biophotonics*; 1 ed. **2011**; Vol. 1, p 210.

photons content information about the vibrational changes undergone by the molecule, which are characteristic features for its identification. This vibrational description of specific targets is the basis for Raman effect spectroscopy.[58]

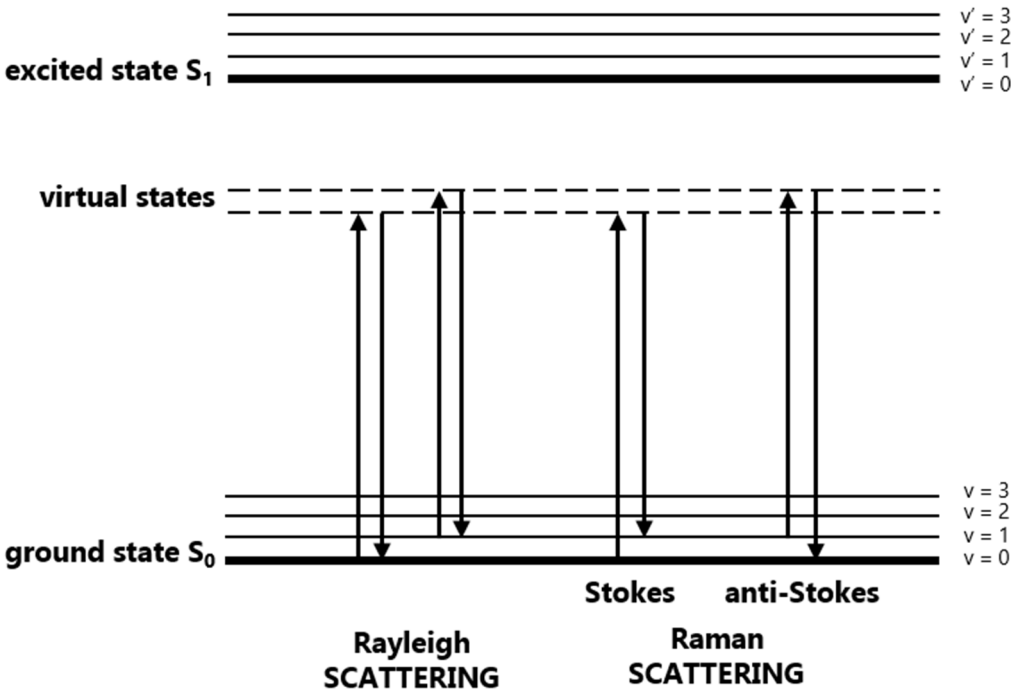

FIGURE 1.26 Jablonski diagram of electron transition for Rayleigh, stokes and anti-stokes Raman sacttering.

Raman spectrum

As mentioned, the energy transference between photons and the molecule are responsible of the molecular vibrations and, in consequence, the scattered photons present a difference in energy from the incident ones. Gain or lose, the energy difference of the scattered photon can be valuable information about the vibrational mode of the molecule. This energy exchange (Eq.2) or Raman shift (expressed as wavenumber, cm^{-1}) can be used in the Raman spectrum (**Fig. 1.27**) to represent the specific vibrational pattern of a given molecule front the intensity of the Raman scattering.[60]

$$\text{Eq.2} \qquad \Delta E_R = E_i - E_s$$

(E_i is the energy of incident photon and E_s of the scattered photon)

So, the Raman spectrum suppose a unique fingerprint of a molecule where each specific band informs about the vibrational modes of the molecule.

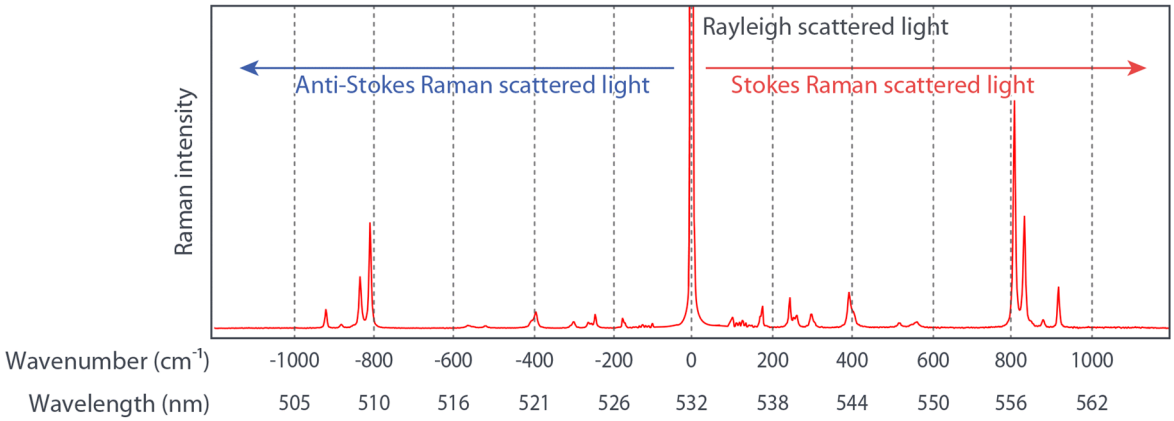

FIGURE 1.27 Raman spectrum of a molecule presenting the stokes and anti-stokes Raman scattering bands.

Raman cross-section

In a similar way of quantum yield for fluorescence, the number of photons that are scattered from the total incident photons can serve to quantify the amount of signal produced by a molecule in terms of intensity. The quantitative determination of the signal produced, termed as power *P* is directly dependent on the probability of the incident photons to collide with a molecule, known as Raman cross-section (σ) and the density of the incident power density, S_{Inc}. Therefore, the selection of good Raman-active molecules will depend on cross-section, as higher σ presents a given molecule, more probability of interaction with incident photons and, in consequence, large Raman signal production (Eq. 3).[59,60]

Eq. 3 $P = \sigma \times S_{Inc}$

Enhancement of the Raman signal

Raman spectroscopy has been used during years to study the chemistry of biological molecules since provides a specific fingerprint of the molecular structure and composition. Combination with conventional microscopy allows for the investigation of biological specimens as tissues or cells at the submicron level. Despite its high specificity, Raman offers a really low intensity, since only a small fraction of the total number of incident photons are inelastically scattered (10^6 to 10^8 photons), which complicates detection of molecules present in low concentrations.[62,63] One way to overcome this major drawback is the enhancement of the Raman signal using an electromagnetic field present at surface of metallic substrates. The surface-enhanced Raman scattering or SERS suppose a high sensitive technique since increases the Raman scattering of a molecule located near to surface of metallic nanostructures up to 10^{11} to 10^{14} times more, taking profit of the resonant interaction of the light with the metal.[61]

[62] Le Ru, E.; Etchegoin, P. *Principles of Surface-enhanced Raman Spectroscopy*, 1 ed. Oxford, **2009**; Vol. 1.
[63] Ding, S.-Y.; Yi, J.; Li, J.-F.; Ren, B.; Wu, D.-Y.; Panneerselvam, R.; Tian, Z.-Q. *Nature Reviews Materials* **2016**, *1*, 16021.

(i) Local surface plasmon resonance

When an electromagnetic radiation, as light, interacts with a metallic nanomaterial (e.g. gold or silver nanoparticles), the conduction electrons present on the surface of that material become excited and oscillate as a collective group though the surface. These oscillations termed as surface plasmons (**Fig. 1.28**), act as evanescent waves that propagate in a parallel direction to the metallic surface but decrease moving away from the surface, increasing the local field.[64] If a molecule is closely located to the metal surface then a resonance (local surface plasmon resonance, LSPR) between the plasmons and the molecule occurs, intensifying the vibrational modes of the molecule. This amplification of the molecular vibration permits specific and ultrasensitive detection of targets present even to single-molecule.[62,65,66,67]

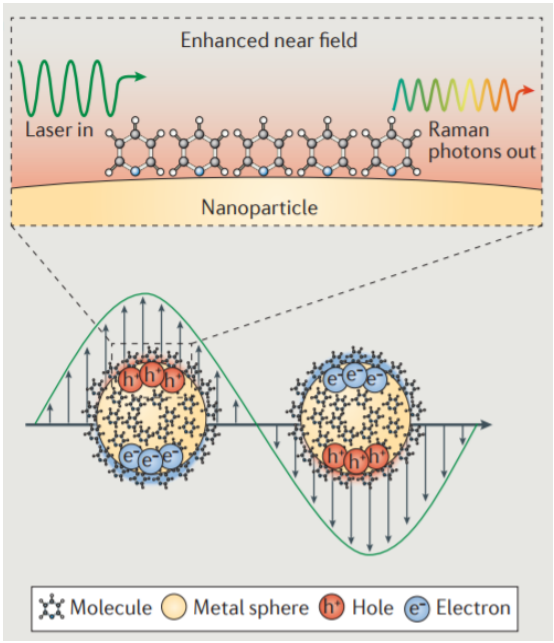

FIGURE 1.28 Schematic diagram of electromagnetic enhancement for molecules close to surface of spherical nanoparticles.[62]

Additionally to electromagnetic enhancement, if the molecule is directly absorbed on the metallic surface then a transfer of the electrons from

[64] Willets, K. A.; Van Duyne, R. P. *Annual review of physical chemistry* **2007**, *58*, 267.
[65] Abalde-Cela, S.; Aldeanueva-Potel, P.; Mateo-Mateo, C.; Rodriguez-Lorenzo, L.; Alvarez-Puebla, R. A.; Liz-Marzan, L. M. *Journal of the Royal Society, Interface* **2010**, *7 Suppl 4*, S435.
[66] Aldeanueva-Potel, P.; Carbo-Argibay, E.; Pazos-Perez, N.; Barbosa, S.; Pastoriza-Santos, I.; Alvarez-Puebla, R. A.; Liz-Marzan, L. M. *Chemphyschem : a European journal of chemical physics and physical chemistry* **2012**, *13*, 2561.
[67] González, A. L.; Noguez, C.; Beránek, J.; Barnard, A. S. *The Journal of Physical Chemistry C* **2014**, *118*, 9128.

the metal to the molecule and turning again to the surface takes place in a chemical enhancement mechanism.

(ii) Metallic substrates for SERS

To create a high confinement of electromagnetic energy, geometry of the nanostructure will directly impact on the LSPR. Thus, large efforts have been focused during years in synthesizing plasmonic nanomaterials in a controlled way.[62] Upon excitation with light at a given wavelength, these structures can show large electromagnetic fields confined at the edges, in the case of rod-like shapes, at the vertices for triangles or at the tips of apexes, for the case of sharp star-like structures (**Fig. 1.29**). Due to the several possibilities of constructing SERS-active materials, three main features should be taken into account for their fabrication and exploitation as ultrasensitive devices: nanostructure composition, size and morphology.[66,68]

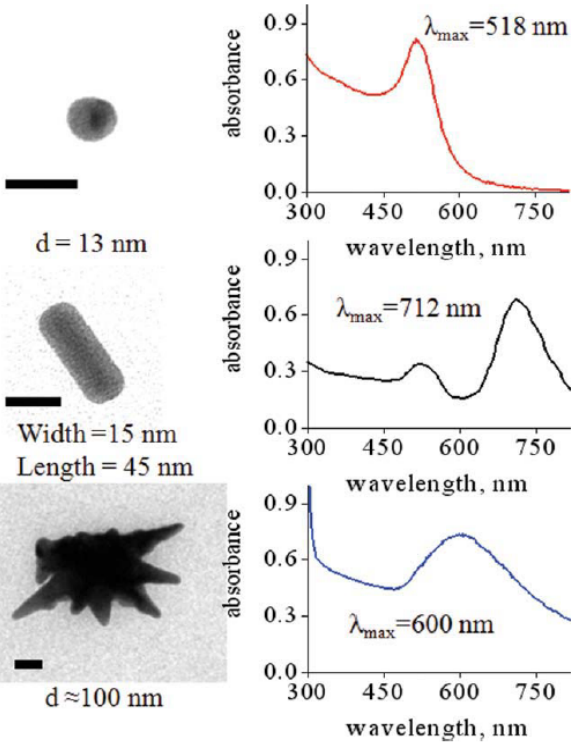

FIGURE 1.29 Au sphere, rod and star-like nanostructures and their corresponding LSPR optical response upon radiation with UV-visible light.[67]

Plasmonic nanostructures composed of noble metals as gold (Au) or silver (Ag), the two metals more used for SERS, suppose good SERS substrates since they present large number of free conduction electrons, allowing for

[68] Hutter, E.; Maysinger, D. *Microscopy Research and Technique* **2011**, *74*, 592.

LSPR. Nature of the material directly determines its plasmonic response and subsequent Raman signal amplification.[61] As an example, Ag nanoparticles are stated as more efficient amplifiers than comparing with similar nanostructures based on Au, from 10 to 100 times.[62,66,69] Additionally, Ag can be excited with a broad range of wavelengths from UV to near-IR while gold is restricted to near-IR or IR regimes, diminishing its versatility for further applications.[68,70] Notwithstanding, most of the current studies involving sensing or therapy with living cells have been focused on the use of Au nanoparticles instead of Ag materials, due to reported cytotoxic effects of the last ones in living systems.[71]

Since the intensity of the electromagnetic field is product of the electron cloud from the atoms conforming the nanostructures, it is obvious that with major number of atoms more electromagnetic enhancement, so it is strongly dependent on the size. However, a radiative attenuation on the Raman signal enhancement has been observed when increasing particles size, limiting the range of optimal amplification to sizes from 30-100 nm.[63,67] The third and most important feature that has been focus of attention is the shape of the structure. Controlling the morphology enables to tune the LSPR response of the material across the whole UV-IR regime, broadening its application in biomedicine as ultrasensitive platforms. Normally, confinement of the electromagnetic density on several regions (**Fig. 1.30**) of the particle results

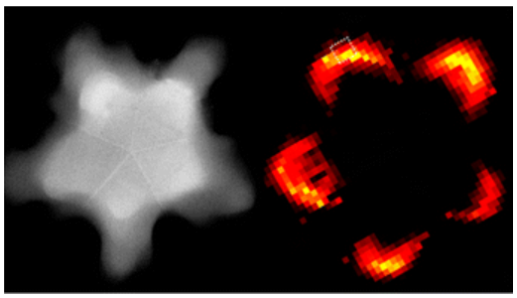

FIGURE 1.30 Au nanostar with energy density concentrated at the sharp tips.[73]

[69] Rodríguez-Lorenzo, L.; Álvarez-Puebla, R. A.; de Abajo, F. J. G.; Liz-Marzán, L. M. *The Journal of Physical Chemistry C* **2010**, *114*, 7336.
[70] Soenen, S. J.; Rivera-Gil, P.; Montenegro, J.-M.; Parak, W. J.; De Smedt, S. C.; Braeckmans, K. *Nano Today* **2011**, *6*, 446.
[71] Sperling, R. A.; Rivera Gil, P.; Zhang, F.; Zanella, M.; Parak, W. J. *Chemical Society Reviews* **2008**, *37*, 1896.

in substantial higher SERS enhancement.[72] So, it is possible to fabricate gold or silver nanorods with the electron density located at the edges or even star-like structures with sharp apexes concentrating the electromagnetic field.[73,74]

(iii) Hot-spots

As seen, particle shape and size play an important role in the LSPR responsible for SERS amplification. Generally, particles not larger than 100 nm are used for SERS purposes since above those dimensions a decay in the enhancement is registered.[64] However, particle aggregates of 200 nm have been reported to provide higher Raman amplification due to coupling events between LSPR from the different particles within the aggregates. These interstitial regions of plasmon coupling are named as *hot-spots* (**Fig. 1.31**) and if a target analyte is located in ther,e a large amplification of the Raman signature of the molecule will take place permitting its ultrasensitive identification.[62,69,73]

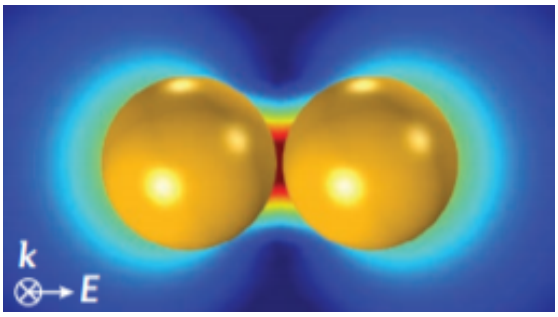

FIGURE 1.31 Au nanoshpeheres in sufficient contact to generate a plasmon coupling hot-spot region (highlighted in red).[62]

[72] Lee, K.-S.; El-Sayed, M. A. *The Journal of Physical Chemistry B* **2006**, *110*, 19220.
[73] Alvarez-Puebla, R. A.; Liz-Marzán, L. M. *Small* **2010**, *6*, 604.
[74] Morla-Folch, J.; Guerrini, L.; Pazos-Perez, N.; Arenal, R.; Alvarez-Puebla, R. A. *ACS Photonics* **2014**, *1*, 1237.

CHAPTER 2

UNIVERSITAT ROVIRA I VIRGILI
NANO/MICROSYSTEMS FOR CANCER DIAGNOSIS AND THERAPY
Manuel García Algar

Detection and quantification of tumor cells through metabolic pathway

Detection of circulating tumor cells (CTCs) in blood samples from cancer patients is still challenging. Most of the methods proposed in the recent years are phenomenological and rely on the use of antibodies labelled with fluorophores, magnetic particles, or immobilized on surfaces to capture the CTCs. Herein, we designed and optimized a method that employs a glucose analogue labelled with a fluorophore which takes advantage of the different metabolic pathways of cancer cells to discern them from normal ones. Notably, we demonstrate that fluorescence signal in tumor cells can be greatly maximized by applying hyperoxia conditions without damaging the cells. These results are demonstrated by means of confocal fluorescence and flow-cytometry measurements in peripheral blood mononuclear cells (PBMC) extracted after Ficoll of human blood samples and spiked with a known concentration of MCF-7 tumour cells.

1 Introduction

Quantification of circulating tumour cells (CTCs) in blood samples from cancer patients is a non-invasive approach to monitoring the status of the disease, as we have described and proved in previous chapters. In recent years, many devices and methods have been proposed for the detection and quantification of CTCs.

Notably, most of these methods rely on the use of antibodies labelled with fluorophores, magnetic particles, or immobilized on surfaces to capture the CTCs. [1,4] However, the number of known antibodies (or aptamers) targeting specific membrane receptors of cancer cells is still very limited, which includes the HER family (EGFR, HER2 and HER3), GD2, PSAm, and PDGF.[5] Thus, most of the methods, including the only FDA-approved (CellSearch®, Janssen Diagnostics), uses antibodies against epithelial receptors such as the epithelial cell adhesion molecule (EpCAM).[6,7] It is well known that, in metastatic cancer, tumour cells experience the epithelial-mesenchymal transition (EMT). In the EMT, epithelial cells lose their cell polarity and cell-to-cell adhesion, while gaining migratory and invasive properties of mesenchymal stem cells.[8,9] In this situation, a significant fraction of the CTCs does not express any residual epithelial receptors and, thus, it remains undetected. [7,8,10] Furthermore, the loss of epithelial characteristics (cytokeratins, for example) is often described as EMT. In these situations, CTC detection based on predefined markers excludes most populations and tumor phenotypes as a consequence of the intratumoral heterogeneity. A solution to this drawback relies on the use of the intrinsic metabolic properties of tumour cells that differ from those of the healthy ones. Specifically, the Warburg effect describes the increase of aerobic glycolysis and glucose uptake in cancer cells.[11] This phenomenon is, for instance, exploited in the positron emission tomography (PET) imaging of tumours in patients by utilizing 2-[^{18}F]fluoro-2-deoxy-D-glucose (^{18}F-FDG).[12] This radioactively-labelled glucose

[1] Pallaoro, A.; Hoonejani, M. R.; Braun, G. B.; Meinhart, C. D.; Moskovits, M. *ACS Nano* **2015**, *9*, 4328.
[2] Alix-Panabieres, C.; Pantel, K. *Lab on a Chip* **2014**, *14*, 57.
[3] Joosse, S. A.; Gorges, T. M.; Pantel, K. *EMBO Mol. Med.* **2015**, *7*, 1.
[4] Pelaz, B.; Alexiou, C.; Alvarez-Puebla, R. A.; Alves, F.; Andrews, A. M.; Ashraf, S.; Balogh, L. P.; Ballerini, L.; Bestetti, A.; Brendel, C.; Bosi, S.; Carril, M.; Chan, W. C. W.; Chen, C.; Chen, X.; Chen, X.; Cheng, Z.; Cui, D.; Du, J.; Dullin, C.; Escudero, A.; Feliu, N.; Gao, M.; George, M.; Gogotsi, Y.; Grünweller, A.; Gu, Z.; Halas, N. J.; Hampp, N.; Hartmann, R. K.; Hersam, M. C.; Hunziker, P.; Jian, J.; Jiang, X.; Jungebluth, P.; Kadhiresan, P.; Kataoka, K.; Khademhosseini, A.; Kopeček, J.; Kotov, N. A.; Krug, H. F.; Lee, D. S.; Lehr, C.-M.; Leong, K. W.; Liang, X.-J.; Ling Lim, M.; Liz-Marzán, L. M.; Ma, X.; Macchiarini, P.; Meng, H.; Möhwald, H.; Mulvaney, P.; Nel, A. E.; Nie, S.; Nordlander, P.; Okano, T.; Oliveira, J.; Park, T. H.; Penner, R. M.; Prato, M.; Puntes, V.; Rotello, V. M.; Samarakoon, A.; Schaak, R. E.; Shen, Y.; Sjöqvist, S.; Skirtach, A. G.; Soliman, M. G.; Stevens, M. M.; Sung, H.-W.; Tang, B. Z.; Tietze, R.; Udugama, B. N.; VanEpps, J. S.; Weil, T.; Weiss, P. S.; Willner, I.; Wu, Y.; Yang, L.; Yue, Z.; Zhang, Q.; Zhang, Q.; Zhang, X.-E.; Zhao, Y.; Zhou, X.; Parak, W. J. *ACS Nano* **2017**.

analogue is internalized by tumour cells in much higher quantities than by normal cells. The PET signal from the tumour cells consequently is higher than in the surrounding tissues and, thus, this can be used to determine the position of the tumour within the body. Similarly, *in vitro* assays have been developed, exploiting the higher internalization rate of nanoparticles by invasive cells as compared to non-invasive ones. [13,14]

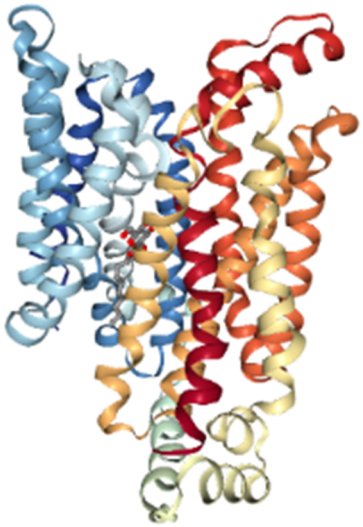

FIGURE 2.1 Molecular structure of human glucose transporter 1 overexpressed in cancer cells.

In this chapter, a method for detection of cancer cells that employs a glucose analogue labelled with a fluorophore 2-[N-(7-nitrobenz-2-oxa-1,3-diazol-4-yl)amino]-2-deoxy-D-glucose (2-NBDG) is designed and optimized.[15] Due to higher glucose uptake, the fluorescence signal of tumour cells is significantly

[5] Grimm, D.; Bauer, J.; Pietsch, J.; Infanger, M.; Eucker, J.; Eilles, C.; Schoenberger, J. *Curr. Med. Chem.* **2011**, *18*, 176.
[6] Baccelli, I.; Schneeweiss, A.; Riethdorf, S.; Stenzinger, A.; Schillert, A.; Vogel, V.; Klein, C.; Saini, M.; Bauerle, T.; Wallwiener, M.; Holland-Letz, T.; Hofner, T.; Sprick, M.; Scharpff, M.; Marme, F.; Sinn, H. P.; Pantel, K.; Weichert, W.; Trumpp, A. *Nat. Biotech.* **2013**, *31*, 539.
[7] Gorges, T. M.; Kuske, A.; Röck, K.; Mauermann, O.; Müller, V.; Peine, S.; Verpoort, K.; Novosadova, V.; Kubista, M.; Riethdorf, S.; Pantel, K. *Clin. Chem.* **2016**, *62*, 1504.
[8] Yu, M.; Bardia, A.; Wittner, B. S.; Stott, S. L.; Smas, M. E.; Ting, D. T.; Isakoff, S. J.; Ciciliano, J. C.; Wells, M. N.; Shah, A. M.; Concannon, K. F.; Donaldson, M. C.; Sequist, L. V.; Brachtel, E.; Sgroi, D.; Baselga, J.; Ramaswamy, S.; Toner, M.; Haber, D. A.; Maheswaran, S. *Science* **2013**, *339*, 580.
[9] Chaffer, C. L.; Weinberg, R. A. *Science* **2011**, *331*, 1559.
[10] Lecharpentier, A.; Vielh, P.; Perez-Moreno, P.; Planchard, D.; Soria, J. C.; Farace, F. *Br J Cancer* **2011**, *105*, 1338.
[11] Vander Heiden, M. G.; Cantley, L. C.; Thompson, C. B. *Science* **2009**, *324*, 1029.

larger than that of healthy ones, which allows their discrimination and quantification by standard flow-cytometry. Notably, the signal difference was maximized under high oxygen level conditions (i.e., hyperoxia). For this study, we compared peripheral blood mononuclear cells (PBMC), extracted after Ficoll of human blood samples, with MCF-7 tumour cells. MCF-7 are human epithelial breast cancer cells which have been widely used for breast cancer research, especially for their expression of the estrogen receptor.[16] Furthermore, the expression of both, the glucose transporter 1 (GLUT1, **Fig. 2.1**) and the EGFR receptor, is elevated in MCF-7 as compared to normal cells.[17,18]

2 Results and Discussion

Sensing strategy

2-[N-(7-nitrobenz-2-oxa-1,3-diazol-4-yl)amino]-2-deoxy-D-glucose (2-NBDG) is a commercial, non-toxic fluorophore characterized by a quantum yield of 0.55 and a blue absorption at 465 nm, which generates an intense emission at 540 nm upon excitation with a blue laser line (**Fig. 2.2A**).[19] After incubation with this fluorophore, normal PBMCs and tumour cells (MCF-7) displayed differences in fluorescence intensity which are too small to univocally distinguish the various types of cells (**Fig. 2.2B**). Note that to identify PBMCs, samples were also incubated with the anti-leukocyte common antigen (CD45) labelled with allophycocyanin (CD45-APC), where APC is a fluorophore characterized by a quantum yield of 0.68 and a red absorption centered at 650 nm, which yields an intense emission at 660 nm upon excitation with a red laser line (**Fig. 2.2A**).[20]

[12] Fletcher, J. W.; Djulbegovic, B.; Soares, H. P.; Siegel, B. A.; Lowe, V. J.; Lyman, G. H.; Coleman, R. E.; Wahl, R.; Paschold, J. C.; Avrill, N.; Einhorn, L. H.; Suh, W. W.; Samson'O, D.; Delbekell, D.; Gorman, M.; Shields, A. F. *J. Nucl. Med.* **2008**, *49*, 480.
[13] Pellegrino, T.; Parak, W. J.; Boudreau, R.; Le gros, M. A.; Gerion, D.; Alivisatos, A. P.; Larabell, C. A. *Differentiation* **2003**, *71*, 542.
[14] Parak, W. J.; Boudreau, R.; Le Gros, M.; Gerion, D.; Zanchet, D.; Micheel, C. M.; Williams, S. C.; Alivisatos, A. P.; Larabell, C. *Adv. Mater.* **2002**, *14*, 882.
[15] Zou, C.; Wang, Y.; Shen, Z. *J. Biochem. Biophys. Methods* **2005**, *64*, 207.
[16] Holliday, D. L.; Speirs, V. *Breast Cancer Res.* **2011**, *13*, 1.
[17] Millon, S. R.; Ostrander, J. H.; Brown, J. Q.; Raheja, A.; Seewaldt, V. L.; Ramanujam, N. *Breast Cancer Res. Treat.* **2011**, *126*, 55.

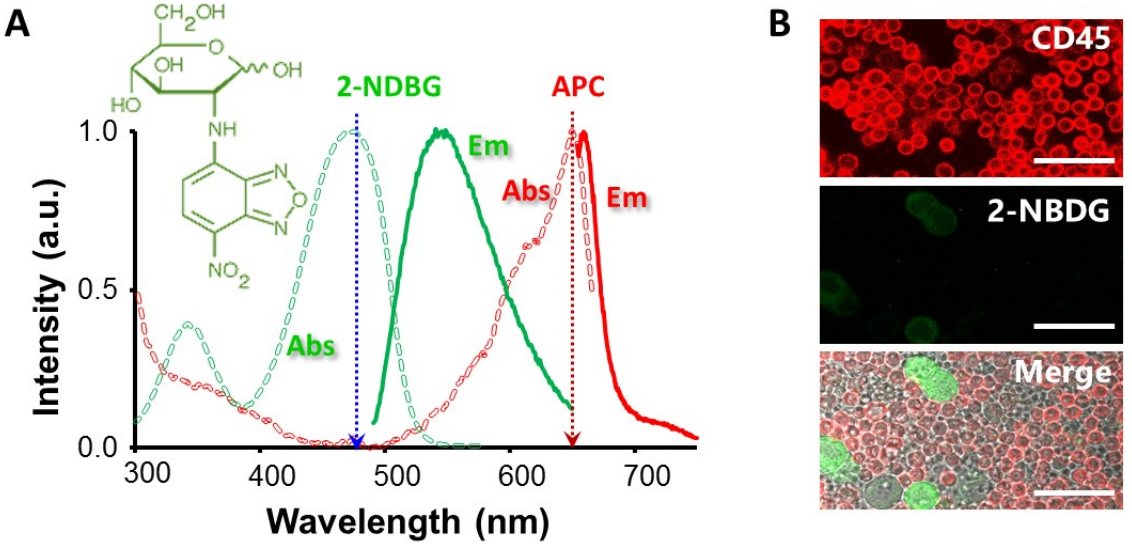

FIGURE 2.2 (A) Absorption and emission profiles of 2-NBDG and APC. Dotted arrows indicate the excitation lines. Molecular structure of 2-NBDG. (B) Laser scanning confocal microscopy images of 2-NBDG uptake for PBMC and MCF-7 incubated with 300 μM 2-NBDG for 30 minutes in samples containing cell ratios of 1:10 MCF-7:PBMC. The bars indicate 40 μm.

Several experimental parameters (incubation time, ionic strength, pH, temperature and oxygen content) were investigated to maximize the difference in fluorescence emission between healthy and tumour cells. Notably, alterations of ionic strength, pH, and temperature did not produce any relevant effect. Regarding the incubation time, no plateau was reached within 30 minutes. However, larger incubation times did increase the fraction of cells undergoing apoptosis or autophagy due to the depletion of growth factors.[21] In fact, 2-deoxy-D-glucose (2DG), the non-fluorescent form of 2-NBDG, induces oxidative stress and apoptosis in cancer cells.[22] More interesting is, however, the case of the oxygen concentration. In fact, in our initial screening measurements, the influence of the oxygen content on the glucose uptake was clearly visible for both PBMC and MCF-7 cells. Therefore, we designed a set of experiments performed at different incubation times (from 0 to 30 min) and different oxygen concentration (hypoxia, normoxia, and hyperoxia) with the aim of understanding the simultaneous effect of these parameters on both

PBMC and MCF-7 cells. Overall, in the investigated period, fluorescence displays a general increase with both time and oxygen content (**Fig. 2.3A**). For all the cases, no cell death was observed within the maximum experimental period (30 min). For PBMC, fluorescence increases slightly over time. Also, the concentration of oxygen in the sample does not have any relevant effect on the emission signal. For MCF-7, although fluorescence increases considerably with time both in hypoxia and normoxia, in the case of hyperoxia such increase is significantly larger. **Fig. 2.3B** shows the ratiometric difference in 2-NBDG fluorescence emission between PBMC and MCF-7 obtained by dividing the signal intensity of the tumour cells by that of the healthy ones as a function of the oxygen conditions. These results were corroborated by confocal fluorescence imaging (**Fig. 2.4**). In this later panel, a remarkable increase in the intensity of the cells can be observed as compared with **Fig. 2.3B**.

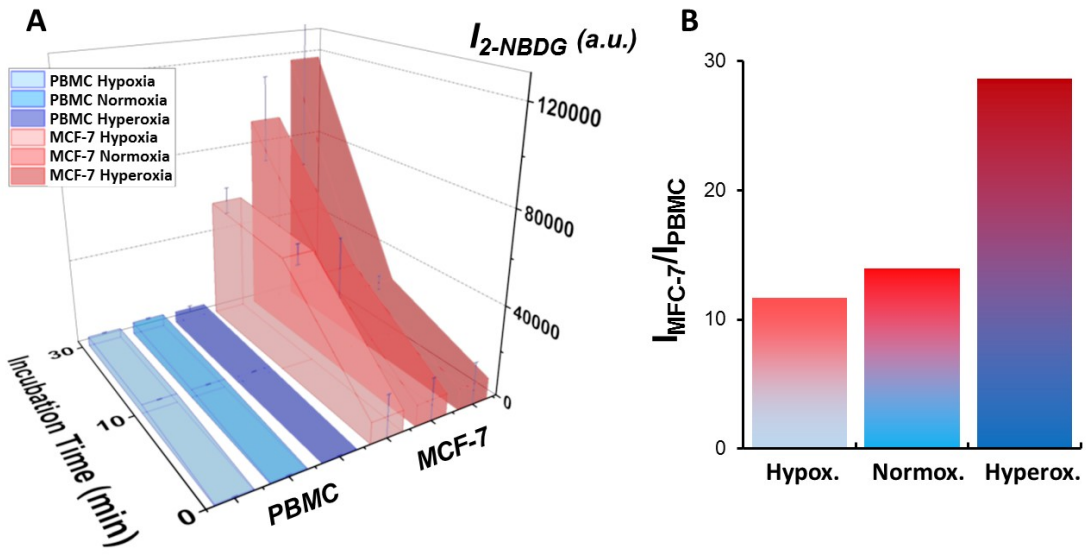

FIGURE 2.3 (A) Optimization of 2-NBDG incubation time under different microenvironments: hypoxia, normoxia, and hyperoxia. 3D Walls graph with the oxygen condition for each cell line in z-axis, incubation time (min) in x-axis, and intensity of 2-NBDG/a.u. in y-axis. The results are presented as mean ± standard deviation of three independent experiments (*n=3*) for samples containing cell ratios of 1:10 MCF-7:PBMC. The median values of 10,000 cytometry events were recorded for each sample.

Incubation of cancer cells in the absence of oxygen has been frequently employed in the literature for the culture of tumour cells in order to expand them or even to establish a cell line.[23,24] Contrarily, hyperoxia is rarely employed or studied. One reason is that long-term treatment in hyperoxia has shown to have adverse effects on cells.[25,26] As opposed to what was hypothesized until recently, the Warburg effect is not explained by the increase of glycolysis rate of tumour cells due to mitochondrial damage. Rather, such increase is ascribed to their high replication rate, a process that requires more biomass synthesis than energy. This characteristic is common to all tumour cells that, despite their enormous heterogeneity, share the property of dedicating the resources of the tricarboxylic acid cycle to the synthesis of biomolecules.[27,28] Thus, the larger increase of fluorescence intensity in MCF-7 cells under high oxygen content may be explained considering that hyperoxia competes with this biosynthetic flux giving rise to a compensatory increase in glycolysis. On the other hand, the replication rate of normal cells is low and, thus, the need for new biomass is limited.

[18] Subik, K.; Lee, J.-F.; Baxter, L.; Strzepek, T.; Costello, D.; Crowley, P.; Xing, L.; Hung, M.-C.; Bonfiglio, T.; Hicks, D. G.; Tang, P. *Breast Cancer* **2010**, 35.
[19] Natarajan, A.; Srienc, F. *Metab. Eng.* **1999**, *1*, 320.
[20] Sauer, M.; Hofkens, J.; Enderlein, J. *Handbook of Fluorescence Spectroscopy and Imaging*; WILEY-VCH Verlag: Weinheim, Germany, 2011.
[21] Eisenberg-Lerner, A.; Bialik, S.; Simon, H. U.; Kimchi, A. *Cell Death Diff.* **2009**, *16*, 966.
[22] Zhang, D.; Li, J.; Wang, F.; Hu, J.; Wang, S.; Sun, Y. *Cancer Lett.* **2014**, *355*, 176.
[23] Cayrefourcq, L.; Mazard, T.; Joosse, S.; Solassol, J.; Ramos, J.; Assenat, E.; Schumacher, U.; Costes, V.; Maudelonde, T.; Pantel, K.; Alix-Panabières, C. *Cancer Res.* **2015**, *75*, 892.
[24] Yu, M.; Bardia, A.; Aceto, N.; Bersani, F.; Madden, M. W.; Donaldson, M. C.; Desai, R.; Zhu, H.; Comaills, V.; Zheng, Z.; Wittner, B. S.; Stojanov, P.; Brachtel, E.; Sgroi, D.; Kapur, R.; Shioda, T.; Ting, D. T.; Ramaswamy, S.; Getz, G.; Iafrate, A. J.; Benes, C.; Toner, M.; Maheswaran, S.; Haber, D. A. *Science* **2014**, *345*, 216.
[25] Allen, C. B.; White, C. W. *Am. J. Physiol. Lung Cell. Mol. Physiol.* **1998**, *274*, L159.
[26] Das, K. C. *Plos One* **2013**, *8*, e73358.
[27] DeBerardinis, R. J.; Chandel, N. S. *Science Advances* **2016**, *2*, e1600200.
[28] Raa, A.; Stansberg, C.; Steen, V. M.; Bjerkvig, R.; Reed, R. K.; Stuhr, L. E. *BMC Cancer* **2007**, *7*, 23.

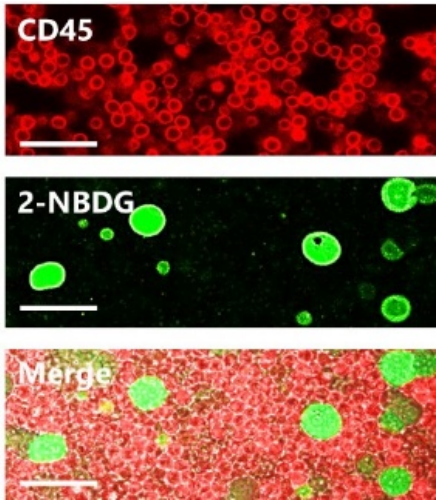

FIGURE 2.4 Laser scanning confocal microscopy images of 2-NBDG uptake for PBMC and MCF-7 under optimized conditions for samples containing cell ratios of 1:10 MCF-7:PBMC. Scale bars = 40 µm.

Sensing performance and cancer cells detection in human blood

Based on the previous results, we selected 30 min of incubation time and hyperoxia as the optimized conditions for the rest of the study. Then, in the next step, we analysed samples prepared by diluting tumour cells into suspensions of peripheral blood mononulear cells (PBMCs) from healthy donors blood. Specifically, MCF-7 cells were spiked into PBMCs cells at ratios between 1:1 and 1:10,000, and the assay was performed with the optimized conditions (i.e., 300 µM 2-NBDG in phosphate buffered saline, PBS, for 30 minutes under hyperoxia). The range of investigated cell ratios was determined down to 1:10,000 to simulate the frequency of CTCs in blood samples from patients after enrichment steps, for instance after applying a Ficoll gradient step. Suspensions of MCF-7 and PBMC cells at different ratios were then mixed with 2-NBDG and, also, CD45-APC, to additionally recognize

PBMCs under hyperoxia. After 30 minutes of incubation, the samples were washed and measured in the flow-cytometer. A blue (488 nm) and a red (640 nm) lasers were used to detect either the MCF-7 (blue) or the PBMC (red) cells, as shown in **Fig. 2.5**. Positive events were considered for cells showing only green fluorescence. On the other hand, cells displaying red or both green and red fluorescence were considered as negative events (PBMC). Notably, the data show a very good agreement with the expected number of cells in the samples (**Fig. 2.6A**) by monitoring the emission produced during the cell metabolism of 2-NBDG upon oxygen enrichment. In this regard, it is possible to extract, for any cell ratio, an average signal for the intrinsic fluorescence developed by individual cells. This can be achieved by dividing the total fluorescence intensity, resulting from the treatment of PBMC and MCF-7 cells with 2-NBDG, by the corresponding number of events for every cell line in each sample. These results are plotted in **Fig. 2.6B**.

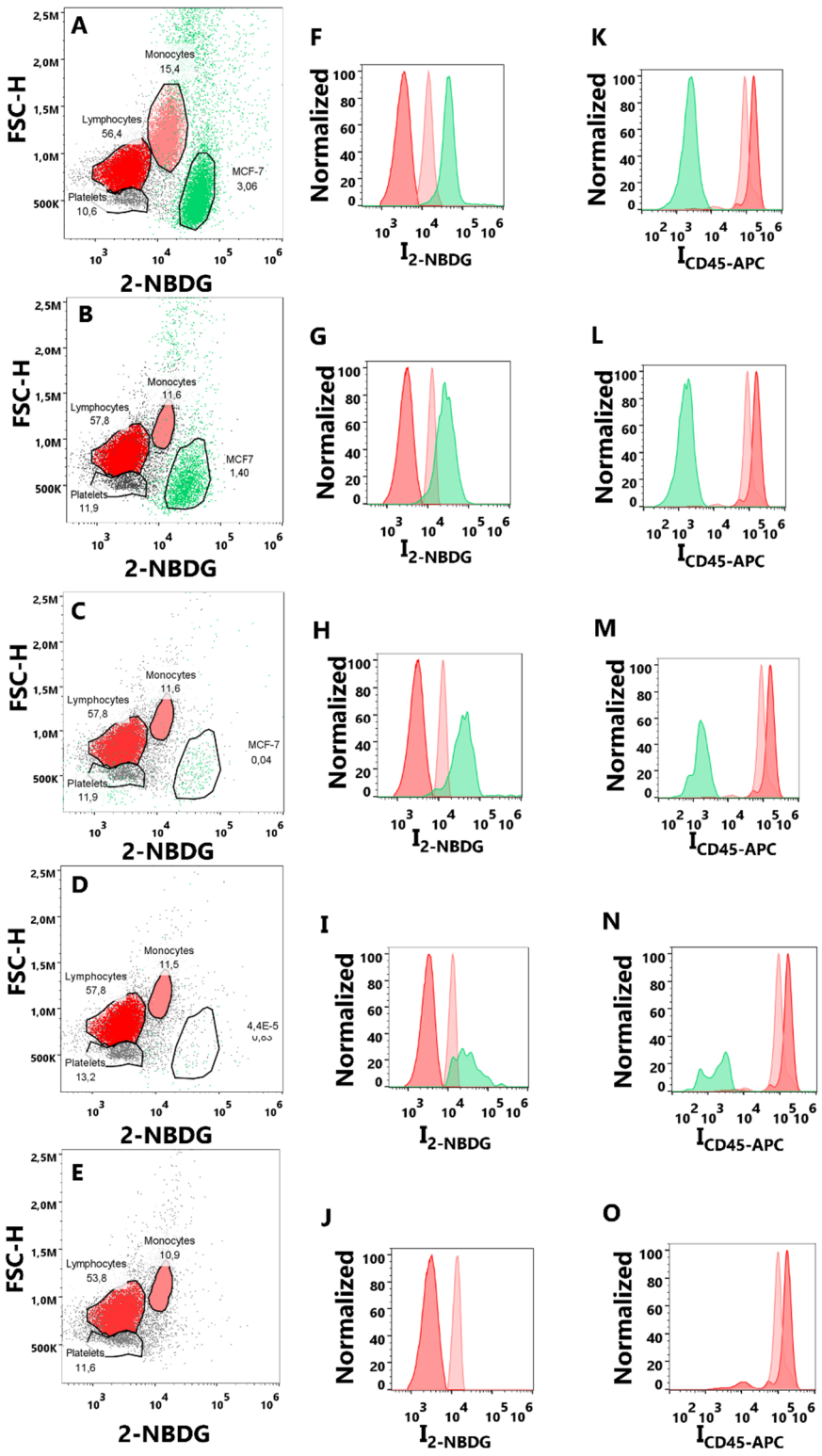

FIGURE 2.5 (A-E) Flow cytometry plots of MCF-7 and PBMCs samples with cell ratios (A) 1:10, (B) 1:100, (C) 1:1000, (D) 1:10000 and (E) only PBMCs; upon incubation with 2-NBDG and CD45-APC for 30 minutes under hyperoxia conditions. (F-O) Distributions of fluorescence intensities for (F-I) 2-NBDG and (K-O) CD45-APC, for each MCF-7:PBMC ratio; and (J) 2-NBDG and (O) CD45-APC, in a sample of PBMC.

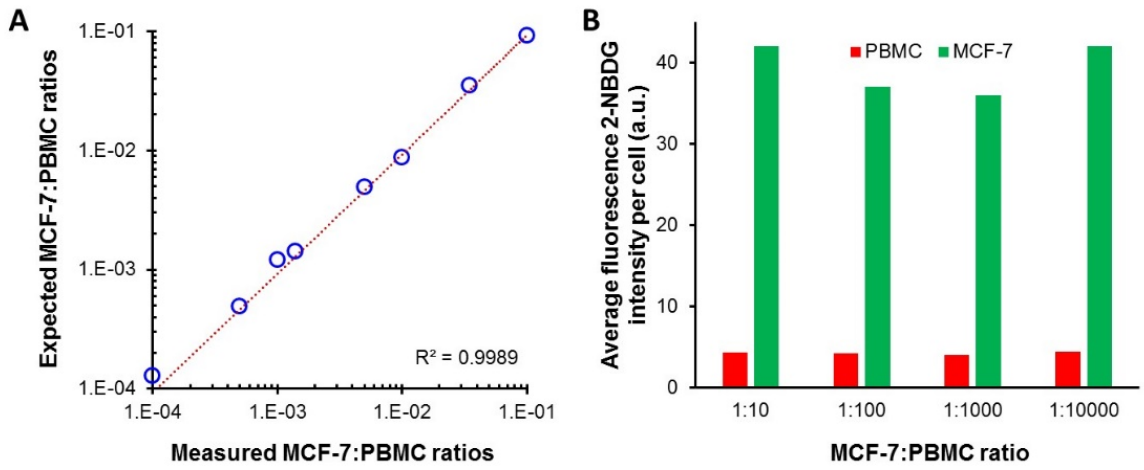

FIGURE 2.6 (A) Comparison between the expected and measured MCF-7:PBMC ratios for the samples incubated with 2-NBDG and CD-45 for 30 min under hyperoxia. (B) Normalized fluorescence intensities per cell for PBMC and MCF-7 treated with 2-NBDG under optimized oxygen content and incubation time conditions. Samples with cell ratios of 1:10, 1:100, 1:1000, and 1:10000.

Outstandingly, these data show that at any cell ratio the fluorescence of tumour cells is considerably larger than that of normal cells, allowing for single event recognitions even at highly diluted regimes.

3 Conclusions

In summary, we have demonstrated the feasibility of using 2-NBDG to discriminate tumour cells from normal cells in a flow cytometric assay under optimized experimental conditions (incubation time and hyperoxia). This method paves the way for the development of the next generation of liquid biopsies as it relies on the intrinsic and universal metabolic property of the tumour cells, rather than on a phenomenological characteristic, such as the presence of a receptor on a tumour cell membrane. We envision that this metabolic alternative to receptor-based liquid biopsies will help to solve the problems derived from the cell heterogeneity resulting from the epithelial-mesenchymal-transition. In fact, the possibility of also detecting CTCs belonging to the mesenchymal lineage, will increase the sensitivity and, thus, allow their potential detection even at earlier stages of the disease.

4 Experimental section

Cell Cultures

MCF-7 cancer cells derived from mammary breast were obtained from the American Tissue Culture Collection (ATCC, Manassas, VA, USA) and cultured in Eagle's Minimum Essential Medium (EMEM) with 10 % fetal bovine serum (FBS) and 0.01 mg/ml human recombinant insulin, at 37º C in a humidified 5 % CO_2 environment.

2-NBDG Uptake optimization

A certain amount of MCF-7 cancer cells were spiked into collected PBMCs from healthy donors. Cells were pelleted and placed in 100 µL PBS 10% FBS, 4 µL anti-CD45-APC (for PBMCs) and 100 µL of 2-NBDG 300 µM for different incubation times and oxygen availability: 0 min, 10 min and 30 min; hypoxia, normoxia and hyperoxia. Hypoxia environment was constructed by bubbling nitrogen gas into 2-NBDG solution, for 20 min and, oxygen gas was used for the hyperoxia condition. After, cells were washed twice by centrifugation at 250g for 10 min and suspended in cold-PBS. Additionally, different amounts of MCF-7 cancer cells were selected and spiked into the blood: 100,000; 10,000; 1,000 and 100 cells for $1x10^6$ PBMCs. The same amounts of stains were added, as previously described, and 300 µM, 30 min of time and hyperoxia environment were used for the 2-NBDG incubation, as the optimized condition.

Sample measurement with the flow-cytometer

Flow cytometry of the samples was carried out in a NovoCyte Flow Cytometer (from AceaBiosciences), equipped with a 488 nm and 640 nm excitation lasers and 530/30 nm and 675/30 nm detection filters. Cytometric data were analyzed with NovoExpress and FloJo VX software.

Laser Scanning Confocal microscopy analysis

MCF-7 cells were harvested from culture dishes with cell dissociation buffer and 100,000 cells were spiked into $1x10^6$ PBMCs. The same amounts of stains were added, as previously described, and 300 µM and 30 min of time were used for the 2-NBDG incubation under hyperoxia environment, as the optimized condition; and 10 min under normoxia were used as non-optimized condition. After, cells were washed twice by centrifugation at 250g for 10 min and suspended in cold-PBS. Finally, 100µL of cell solution were disposed onto 8-well µ-Ibidi plates and analysed under laser scanning confocal microscopy using 488 nm and 532 nm excitation lasers and 515/30 nm and 650LP filters to collect fluorescence. Same exposure conditions were applied to compare 2-NBDG fluorescence intensities between samples: 40x macrolense, 69.3% laser power, 13.20 pixel dwell and middle pinhole.

Statistical Analysis

Statistical analysis was performed to check whether intensity differences between cell line, oxygen condition and incubation time were significant. A total of 10,000 cytometric events (*n=10,000)* were chosen per sample. The normality of the data was checked using a Kolmogorov-Smirmow test showing a non-normal distribution, hence, the data is presented as medians. For comparison of more than 2 non-parametric groups Krustal-Wallis and *post hoc* tests were selected in SPSS 22 software. Significancy was set up at $P < 0.01$.

CHAPTER 3

UNIVERSITAT ROVIRA I VIRGILI
NANO/MICROSYSTEMS FOR CANCER DIAGNOSIS AND THERAPY
Manuel García Algar

Disease monitoring and staging of lung cancer with metabolic liquid biopsy

Quantification of circulating tumor cells (CTCs) in blood samples from cancer patients is a non-invasive approach to monitoring the status of the disease. Here, findings suggest that the metabolic liquid biopsy (MLB) coupled with statistical and probabilistic data analysis is a promising non-invasive approach for diagnosis and staging of patients. In fact, MLB can not only quantify the disease burden but also classify the disease extension before CT and PET scans and with lower uncertainty.

1 Introduction

Lung cancer is the second most common tumor malignancy and is a leading cause of cancer death worldwide in both women and men (1.69 million deaths in 2015). [1] According to American Cancer Society, the incidence of this disease was about 225.500 new diagnosed cases with 154.050 deaths in 2017. [2] The prevalence of the disease is very low due to its high mortality resulting from the early dissemination of cancer cells to secondary sites which are not detectable by conventional procedures. [3] Notably, for stages I and IV, 5-year survival is 80% and

[1] Coleman, W.; Rubinas, T. In *Molecular Pathology*, Elsevier, Ed. Oxford, **2009**, p 63
[2] Hanahan, D.; Weinberg, R. A. *Cell* **2011**, *144*, 646.
[3] *Cancer survival and prevalence in Australia: period estimates from 1982 to 2010*, Australian Institute of Health and Welfare: Canberra, **2012**.

10%, respectively. [4] Thus, early stages (I-II) are defined by the curability. However, even with radical surgery, between 30-50% of patients at early stages relapse. [5] Stages III are even more heterogeneous, with a 5-year survival between 13% and 36%. Reason for these high recurrence rates, even after radical surgery, are believed to be related with the presence of micrometastasis or lesions not detected by the diagnostic staging. That is, an inadequate staging. [6] Thus, methods that perform adequate staging are not only essential in the diagnosis, but also for detecting relapses or monitoring the response to therapy.

Currently, the lung cancer staging is based on (i) the tumor-node-metastasis (TNM) staging system, which typically relies on images acquired via computerized tomography (CT) and the positron emission tomography (PET); and (ii) the anatomopathological diagnosis. [7] However, CT and PET scans suffer from major limitations in terms of resolution and accuracy. Among others, radiological lesions compatible with cancer are not always evident. [8] Further, inflammatory or nonspecific lesions can be erroneously identified as tumors in CT or PET. [9] Mediastinal lesions (N2 or T4), which are critical factors in determining resectability of the cancer, are characterized by an unsatisfactory diagnostic accuracy. In this regard, a meta-analysis including 45 studies has concluded that, with a standardized uptake value (SUV) cut-off of 2.5, the sensitivity and specificity of PET-CT were 77.4% and 90.1%, respectively. [10]

[4] Chi, K. R. *Nature* **2016**, *532*, 269.
[5] Uramoto, H.; Tanaka, F. *Translational Lung Cancer Research* **2014**, *3*, 242.
[6] Hardingham, J. E.; Grover, P.; Winter, M.; Hewett, P. J.; Price, T. J.; Thierry, B. *Molecular Medicine* **2015**, *21*, S25.
[7] Kay, F. U.; Kandathil, A.; Batra, K.; Saboo, S. S.; Abbara, S.; Rajiah, P. *World Journal of Radiology* **2017**, *9*, 269.
[8] McWilliams, A.; Tammemagi, M. C.; Mayo, J. R.; Roberts, H.; Liu, G.; Soghrati, K.; Yasufuku, K.; Martel, S.; Laberge, F.; Gingras, M.; Atkar-Khattra, S.; Berg, C. D.; Evans, K.; Finley, R.; Yee, J.; English, J.; Nasute, P.; Goffin, J.; Puksa, S.; Stewart, L.; Tsai, S.; Johnston, M. R.; Manos, D.; Nicholas, G.; Goss, G. D.; Seely, J. M.; Amjadi, K.; Tremblay, A.; Burrowes, P.; MacEachern, P.; Bhatia, R.; Tsao, M.-S.; Lam, S. *New England Journal of Medicine* **2013**, *369*, 910.
[9] Feng, M.; Yang, X.; Ma, Q.; He, Y. *Medicine* **2017**, *96*, e7415.
[10] Schmidt-Hansen, M.; Baldwin, D. R.; Hasler, E.; Zamora, J.; Abraira, V.; Roqué i Figuls, M. *Cochrane Database of Systematic Reviews* **2014**.

During the last years, precision medicine has undergone a great change in lung cancer treatment by describing very individualized new disease categories[11,12,13] capable of effectively predicting the response to new treatments. [14] However, the application of precision medicine requires of the fine description of the patient disease at each specific state of the treatment, a task for which PET and CT scans often result insufficient. Thus, current clinical practice demands the definition of new biomarkers to resolve the limitations of CT and PET techniques.

Early and accurate diagnosis of lung metastasis is a pressing clinical need. Lung cancer is prevalent and, in many cases, difficult to detect or staging with accuracy by conventional imaging, as mentioned before. Failing to accurately establish the existing stage of the disease severely impact the quality of diagnosis, as the actual threshold guides the therapeutic strategy from potentially curative to palliative. Important limitations of the imaging techniques, such as at determining the presence of lymph nodes and mediastinal metastasis or discriminating real tumor from reactive process, makes necessary the development of new diagnostic biomarkers, which could also be useful to evaluate the responses to treatment and, once validated, even for early diagnosis.

In this scenario, the quantification of circulating tumor cells (CTCs) in peripherical blood from cancer patients (liquid biopsy, LB) emerges as a non-invasive

---

[11] Reck, M.; Popat, S.; Reinmuth, N.; De Ruysscher, D.; Kerr, K. M.; Peters, S. *Annals of Oncology* **2014**, *25*, iii27.
[12] Abbosh, C.; Birkbak, N. J.; Wilson, G. A.; Jamal-Hanjani, M.; Constantin, T.; Salari, R.; Le Quesne, J.; Moore, D. A.; Veeriah, S.; Rosenthal, R.; Marafioti, T.; Kirkizlar, E.; Watkins, T. B. K.; McGranahan, N.; Ward, S.; Martinson, L.; Riley, J.; Fraioli, F.; Al Bakir, M.; Grönroos, E.; Zambrana, F.; Endozo, R.; Bi, W. L.; Fennessy, F. M.; Sponer, N.; Johnson, D.; Laycock, J.; Shafi, S.; Czyzewska-Khan, J.; Rowan, A.; Chambers, T.; Matthews, N.; Turajlic, S.; Hiley, C.; Lee, S. M.; Forster, M. D.; Ahmad, T.; Falzon, M.; Borg, E.; Lawrence, D.; Hayward, M.; Kolvekar, S.; Panagiotopoulos, N.; Janes, S. M.; Thakrar, R.; Ahmed, A.; Blackhall, F.; Summers, Y.; Hafez, D.; Naik, A.; Ganguly, A.; Kareht, S.; Shah, R.; Joseph, L.; Marie Quinn, A.; Crosbie, P. A.; Naidu, B.; Middleton, G.; Langman, G.; Trotter, S.; Nicolson, M.; Remmen, H.; Kerr, K.; Chetty, M.; Gomersall, L.; Fennell, D. A.; Nakas, A.; Rathinam, S.; Anand, G.; Khan, S.; Russell, P.; Ezhil, V.; Ismail, B.; Irvin-Sellers, M.; Prakash, V.; Lester, J. F.; Kornaszewska, M.; Attanoos, R.; Adams, H.; Davies, H.; Oukrif, D.; Akarca, A. U.; Hartley, J. A.; Lowe, H. L.; Lock, S.; Iles, N.; Bell, H.; Ngai, Y.; Elgar, G.; Szallasi, Z.; Schwarz, R. F.; Herrero, J.; Stewart, A.; Quezada, S. A.; Peggs, K. S.; Van Loo, P.; Dive, C.; Lin, C. J.; Rabinowitz, M.; Aerts, H. J. W. L. *Nature* **2017**, *545*, 446.
[13] Kalia, M. *Metabolism* **2015**, *64*, S16.
[14] Reck, M.; Rabe, K. F. *New England Journal of Medicine* **2017**, *377*, 849.

approach capable of overcoming the drawbacks associated with the conventional imaging techniques. [15] This new concept of biopsy relies on the assumption that CTCs detach from primary solid tumors, enter bloodstream and, after extravasation, act as seeds for metastatic colonies. [16] In this regard, it is worth noticing that not all tumor locations are disseminated or invaded in the same way. [17] Quantification of CTCs has shown to have independent prognostic value in colon, breast and prostate cancer. [18] Differently, studies of pancreatic cancer patients only displayed a general trend toward an association between CTC detection and disease progression. [19]

To date, the main goal of conventional LBs is identifying the relationship between the number of CTCs and the patient prognostic by either measuring progression free survival (PFS) or overall survival (OS). [20] In this way, it had been possible to determine thresholds for CTC content from which prognostic is clearly differentiated. [21] Conversely, the correlation between the clinically defined tumor burden and the number of CTCs has never been established. Although many approaches for CTC quantification have been developed in recent years, all of them are antigen-dependent, that is they rely on antibodies against epithelial receptors such as the epithelial cell adhesion molecule (EpCAM). [22,23,24] Therefore, these

[15] Menis, J.; Hasan, B.; Besse, B. *European Respiratory Review* **2014**, *23*, 367.
[16] Karachaliou, N.; Mayo-de-las-Casas, C.; Molina-Vila, M. A.; Rosell, R. *Annals of Translational Medicine* **2015**, *3*.
[17] Pantel, K.; Brakenhoff, R. H. *Nat. Rev. Cancer* **2004**, *4*, 448.
[18] Miller, M. C.; Doyle, G. V.; Terstappen, L. W. M. M. *Journal of Oncology* **2010**, *2010*.
[19] Tjensvoll, K.; Nordgård, O.; Smaaland, R. *Int. J. Cancer* **2014**, *134*, 1.
[20] Bidard, F.-C.; Peeters, D. J.; Fehm, T.; Nolé, F.; Gisbert-Criado, R.; Mavroudis, D.; Grisanti, S.; Generali, D.; Garcia-Saenz, J. A.; Stebbing, J.; Caldas, C.; Gazzaniga, P.; Manso, L.; Zamarchi, R.; de Lascoiti, A. F.; De Mattos-Arruda, L.; Ignatiadis, M.; Lebofsky, R.; van Laere, S. J.; Meier-Stiegen, F.; Sandri, M.-T.; Vidal-Martinez, J.; Politaki, E.; Consoli, F.; Bottini, A.; Diaz-Rubio, E.; Krell, J.; Dawson, S.-J.; Raimondi, C.; Rutten, A.; Janni, W.; Munzone, E.; Carañana, V.; Agelaki, S.; Almici, C.; Dirix, L.; Solomayer, E.-F.; Zorzino, L.; Johannes, H.; Reis-Filho, J. S.; Pantel, K.; Pierga, J.-Y.; Michiels, S. *The Lancet Oncology* **2014**, *15*, 406.
[21] Krebs, M. G.; Sloane, R.; Priest, L.; Lancashire, L.; Hou, J.-M.; Greystoke, A.; Ward, T. H.; Ferraldeschi, R.; Hughes, A.; Clack, G.; Ranson, M.; Dive, C.; Blackhall, F. H. *Journal of Clinical Oncology* **2011**, *29*, 1556.
[22] Baccelli, I.; Schneeweiss, A.; Riethdorf, S.; Stenzinger, A.; Schillert, A.; Vogel, V.; Klein, C.; Saini, M.; Bauerle, T.; Wallwiener, M.; Holland-Letz, T.; Hofner, T.; Sprick, M.; Scharpff, M.; Marme, F.; Sinn, H. P.; Pantel, K.; Weichert, W.; Trumpp, A. *Nat. Biotech.* **2013**, *31*, 539.
[23] Gorges, T. M.; Kuske, A.; Röck, K.; Mauermann, O.; Müller, V.; Peine, S.; Verpoort, K.; Novosadova, V.; Kubista, M.; Riethdorf, S.; Pantel, K. *Clin. Chem.* **2016**, *62*, 1504.
[24] Pedrol, E.; Garcia-Algar, M.; Massons, J.; Nazarenus, M.; Guerrini, L.; Martínez, J.; Rodenas, A.; Fernandez-Carrascal, A.; Aguiló, M.; Estevez, L. G.; Calvo, I.; Olano-Daza, A.; Garcia-Rico, E.; Díaz, F.; Alvarez-Puebla, R. A. *Sci. Rep.* **2017**, *7*, 3677.

methods are unable to detect cells that do not express the preselected markers. [25] Thus, due to the high heterogeneity of CTCs, comprising epithelial tumor cells, cells that underwent the epithelial-mesenchymal transition (EMT), tumor stem cells and even clusters of tumor cells, current LB approaches "simply" enumerate a single subpopulation of CTCs while failing to fully describe the whole ensemble. Further, available LBs [26] intrinsically underestimate the number of CTCs in blood due to their antigen-based approach which limits the count of positive events to the sole recognition of cells with epithelial receptors in their membrane (i.e., EpCAM)[27], while mesenchymal, tumor stem cells or fluctuating phenotypic CTCs [28,29] are completely disregarded. This represents a major issue; for example, a recent study conducted in patients with lung cancer undergoing radical surgery (early stages) showed that the highest preoperative clinical staging was related to the increased presence of mesenchymal CTCs but not with epithelial cells. [30] In addition, a comparative enumeration of CTCs of the same sample obtained by using EpCAM with CellSearch® (the only FDA approved LB) and cytometry showed that the former technique only accounts for a third of CTCs events yielded by cytometry. [31] Thus, to date, it is unknown whether the prognostic value revealed by these CTC quantification studies reflects the radiologic volume/stage of the disease or is correlated with other biological characteristics, such as those associated with aggressiveness, invasiveness or the type of CTC detected. [32,33]

---

[25] Mego, M.; Reuben, J.; Mani, S. A. In *Liquid Biopsies in Solid Tumors*; Cristofanilli, M., Ed.; Springer International Publishing: Cham, 2017, p 67.
[26] Joosse, S. A.; Gorges, T. M.; Pantel, K. *EMBO Molecular Medicine* **2015**, *7*, 1.
[27] Grimm, D.; Bauer, J.; Pietsch, J.; Infanger, M.; Eucker, J.; Eilles, C.; Schoenberger, J. *Current Medicinal Chemistry* **2011**, *18*, 176.
[28] Gupta, Piyush B.; Fillmore, Christine M.; Jiang, G.; Shapira, Sagi D.; Tao, K.; Kuperwasser, C.; Lander, Eric S. *Cell* **2011**, *146*, 633.
[29] Al-Hajj, M.; Wicha, M. S.; Benito-Hernandez, A.; Morrison, S. J.; Clarke, M. F. *Proceedings of the National Academy of Sciences* **2003**, *100*, 3983.
[30] Xie, Z.; Gao, X.; Cheng, K.; Yu, L. *Oncology Letters* **2017**, *14*, 5825.
[31] Coumans, F. A. W.; Ligthart, S. T.; Uhr, J. W.; Terstappen, L. W. M. M. *Clinical Cancer Research* **2012**, *18*, 5711.
[32] Micalizzi, D. S.; Maheswaran, S.; Haber, D. A. *Genes & Development* **2017**, *31*, 1827.
[33] Normanno, N.; De Luca, A.; Gallo, M.; Chicchinelli, N.; Rossi, A. *Expert Review of Anticancer Therapy* **2016**, *16*, 859.

Alternatively, instead of using markers targeting specific membrane receptors[34], CTCs can be labeled by profiting from their characteristic metabolic activity (Warburg effect). [35]

In this chapter, it is presented a metabolic approach to the liquid biopsy that can sensitively, specifically, and safely detect the presence of CTCs in model patients with lung cancer at stage IV. This approach is based on the previous method discussed on Chapter 2. A glucose analogue labelled with a fluorophore is added to the cell sample containing CTCs, then, the larger uptake of dye-labelled glucose molecules by tumor cells as compared with normal cells enables their detection by fluorescence spectroscopy.

[34] Grimm, D.; Bauer, J.; Pietsch, J.; Infanger, M.; Eucker, J.; Eilles, C.; Schoenberger, J. *Current Medicinal Chemistry* **2011**, *18*, 176.
[35] Fernandez-Carrascal, A.; Garcia-Algar, M.; Nazarenus, M.; Torres-Nuñez, A.; Guerrini, L.; Feliu, N.; Parak, W. J.; Garcia-Rico, E.; Alvarez-Puebla, R. A. *Oncotarget* **2017**, *8*, 76108.

2 Results and Discussion

Sensing strategy

The previously described fluorophore 2-NBDG can be used for optical detection purposes as has been already presented in previous chapters. In this way, peripheral blood mononuclear cells (PBMCs) fractions (lymphocytes and monocytes), extracted through a Ficoll process from human blood samples obtained from healthy donors, were spiked with of a lung cancer cell line (adenocarcinoma human alveolar basal epithelial cells, A549) in a 1:100 ratio (cancer:healthy), and later incubated with cocktail of: (i) 2-NBDG, (ii) anti-leukocyte common antigen (CD45) labelled with allophycocyanin (CD45-APC, absorption: 650 nm, emission: 660 nm), and (iii) anti-cluster of differentiation 14 (CD14) labelled with Peridinin-chlorophyll/Cyanine5.5 (CD14-PerCP/Cy5.5; absorption: 482 nm, emission: 676 nm). **Fig. 3.1A** shows the cytometry results for this sample measured under conventional conditions (300 μM concentration of 2NBDG, 30 minutes of incubation time, and normoxia). The cytogram exhibits three populations. Specifically, CD45+/CD14-/2NBDG-, CD45+/CD14+/2NBDG+ and CD45-/CD14-/2NBDG+ events are ascribed to lymphocytes, monocytes (macrophages and dendritic cells) and cancer cells (A549), respectively. Grey events, negative for all labels, are considered debris.

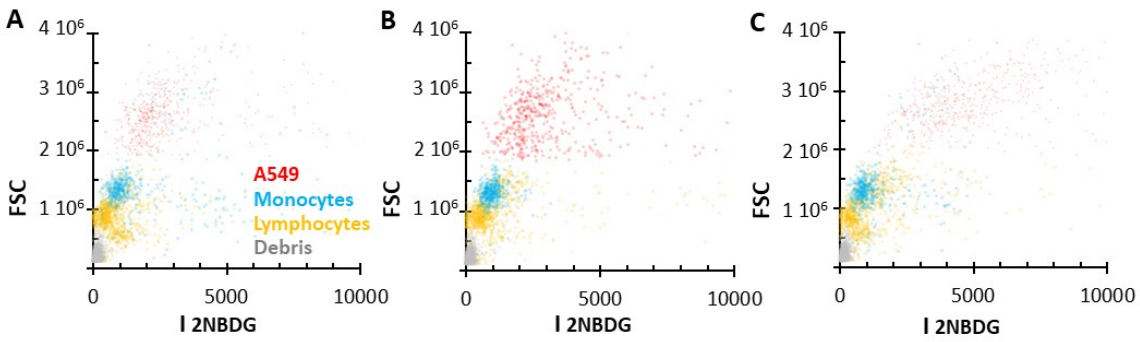

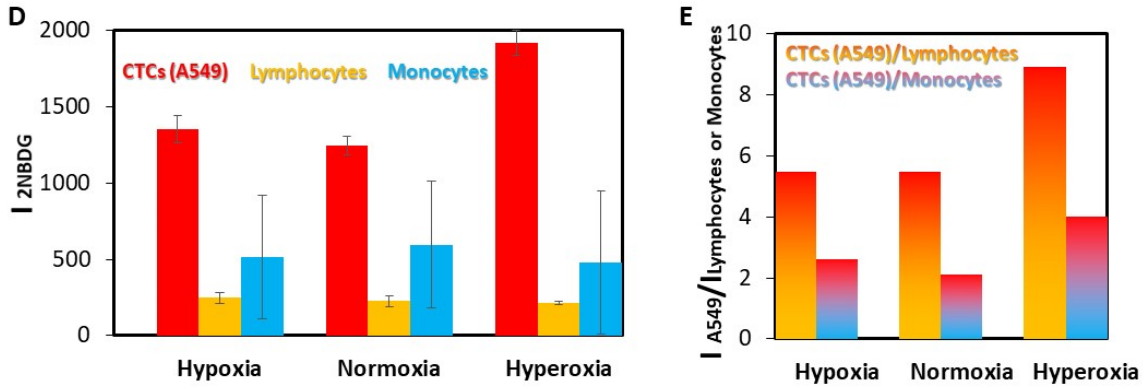

FIGURE 3.1 Flow cytometry of a PBMC obtained from human blood from a healthy donor sample spiked with A549 cells (1:100 ratio, cancer:healthy) as a function of the oxygen conditions. (A) normoxia; (B) hypoxia; and, (C) hyperoxia. (D) Average 2-NBDG fluorescence emission per cell for the different oxygen conditions. (E) Ratiometric differences in 2-NBDG fluorescence emission for cancer cells (A549) and PBMCs (lymphocytes and monocytes) under the three oxygen conditions.

Normal PBMCs and tumor cells display clear differences in 2-NBDG fluorescence intensity which are consistent with their different metabolic activity. As previously demonstrated,[35] the 2-NBDG uptake can be further increased by adjusting the oxygen concentration. In this regard, while the oxygen content has no remarkable effect on the 2-NBDG fluorescence of PBMCs, both hypoxia (**Fig. 3.1B**) and hyperoxia (**Fig. 3.1C**) conditions yield larger fluorescence signals for A549, being significantly larger in the latter case (**Fig. 3.1D**). On the other hand, ratiometric 2-NBDG fluorescence emission measurements for cancer cells vs. PBMCs (Figure 1E) clearly show that hyperoxia conditions (300 μM concentration of 2-NBDG, 30 min incubation time) are the best suited to maximize the fluorescence ratios (i.e., higher discrimination capabilities). It is worth noting that, although larger incubation times and/or 2-NBDG concentrations may increase the fluorescence signals, they also promote apoptosis or autophagy due to the depletion of growth factors.

Sensing performance and cancer cells detection in human blood

The detection limits of the method were tested by analyzing samples containing progressively diluted tumor cells spiked into PBMCs suspensions, from 1:10^2 to 1:10^5 A549:PBMC cells ratios. These suspensions were then incubated with 2-NBDG, CD45-APC and CD14-PerCP/Cy5.5, under hyperoxia conditions. As in the previous cases (**Fig. 3.1A-C**), cytogram show four populations composed by CTCs, lymphocytes, monocytes, and debris (**Fig. 3.2A**, 1:10^4 ratio). However, the representation of the 2-NBDG fluorescence intensity vs. the forward scattering (**Fig. 2B**) reveals that, for samples containing a small fraction of CTCs, the differentiation between A549 and monocytes is no longer accomplished based solely on the 2-NBDG marker. This is likely because some of these PBMC cells may consume large quantities of glucose generating false positives. [35] Such issue is overcome by integrating the CD45 signal as an additional discrimination parameter. In fact, by representing the fluorescence intensity of 2NBDG against that of CD45 (**Fig. 3.2C**), a panel is generated were the different populations can be unambiguously classified in four different quadrants: *up-left* (CD45+/2NBDG-), lymphocytes and monocytes; *up-right* (CD45+/2NBDG+), activated monocytes; *down-left* (CD45-/2NBDG-) debris; and *down-right* (CD45-/2NBDG+), CTCs. **Fig. 3.2D** shows the representation of the number of A549 spiked into the PBMC sample vs. the number of expected CTCs at different cell ratios. Outstandingly, these data show that, for all samples, cells with positive 2-NBDG response and lack of CD45 signal (i.e., CTCs) display such a larger 2-NBDG fluorescence emission as compared to normal cells that single event recognition is achieved even at highly diluted regimes.

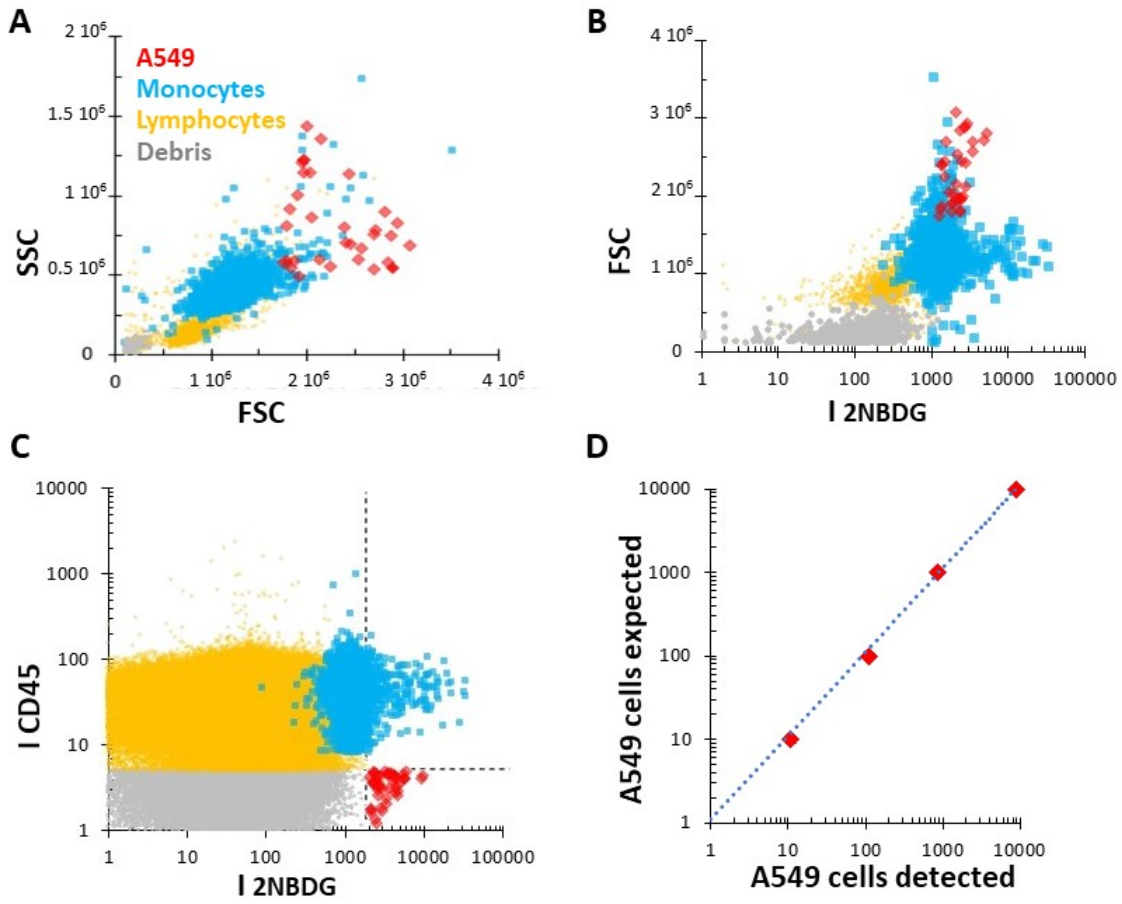

FIGURE 3.2 Flow cytometry distribution of cells PBMC sample obtained from human blood from a healthy donor sample spiked with A549 cells (1:10^4 ratio, cancer:healthy) as a function of the (A) cell complexity and size; (B) 2-NBDG fluorescence emission and size; and, (C) 2-NBDG and CD45 fluorescence emissions. (D) Correlation between detected and expected A549 cells per million of cells for different cancer:healthy cells ratios (1:10^2, 1:10^3, 1:10^4, and 1:10^5).

Clinical diagnosis using MLB

Proof of concept clinical application of this method was demonstrated by quantifying CTCs in real blood samples obtained from different healthy donors (three) and selected lung cancer patients (five). All patients were diagnosed with metastatic lung cancer but with different histology and disease distribution. Their

clinical characteristics at the time of the blood extraction are summarized in **Table 3.1**, while **Fig. 3.3A** shows the correspondent disease extension through CT and PET scans. Samples (8 mL) from healthy donors and patients were treated through density gradient (Ficoll) to extract the peripheral blood mononuclear cells, and subsequently stained with CD45 and 2-NBDG, before running them into the flow cytometer. **Fig. 3.4** shows the results obtained as a function of the fluorescence intensities of 2-NBDG vs. CD45. As in the case of spiked samples, positive CTC recognition events were defined for CD45-/2NBDG+ response. As expected, healthy donors show no evidence of CTCs while patients display, for all the cases, a variable number of tumor cells. These data correlate well with those obtained with conventional diagnosis at the time of sample extraction (**Table 3.1** and **Fig. 3.3A**). First, patients at partial response (CP1) or complete remission (CP5) exhibit a very low number of CTCs. Conversely, those patients with bulky disease at the beginning of the treatment (CP2 and CP3) show a considerably larger number of CTCs. Notably, for CP4 some disagreement appears between the PET scan (Figure 3A) and its high SUV, and the low number of CTCs (**Table 3.1**). However, CP4 represents a clear example of the paradoxical radiological response of some patients when treated with immunological drugs (i.e., pseudoprogression). In these cases, although the patient's clinical situation may appear as a progression of the disease, in reality, the tumor is in remission as clearly demonstrated by CT monitoring over the time after several treatment cycles (**Fig. 3.3B**). [36]

Interestingly, the cytometric panels in **Fig. 3.4** reveals different patterns of PBMCs population distribution between healthy donors and cancer patients, which can be clearly discerned even by the naked eye. For instance, it is evident that the PBMCs population presents a more compact distribution in patients as compared with healthy donors.

[36] Wong, A. N. M.; McArthur, G. A.; Hofman, M. S.; Hicks, R. J. *European Journal of Nuclear Medicine and Molecular Imaging* **2017**, *44*, 67.

TABLE 3.1 Clinical characteristics and tumor extension at the time of blood extraction.

	Anatomopathological diagnostic	**UICC Stage**	**PET SUV**	**PrimaryTumor**	**Metastasis localization**	**CTCs/10^7 PBMCs**
CP1	Adenocarcinoma	IV	7.44	Multimetastatic [a] Non-Bulky	Lung Mediastinal Subcutaneous Skin	20
CP2	Small-cell lung cancer	IV	15.5	Paucimetastatic [b] Bulky	Mediastinal Lung	160
CP3	Undifferentiated CA	IV	6.23	Paucimetastatic Bulky	Mediastinal Lung	120
CP4	Epidermoid CA	IV	19.8	Paucimetastatic Bulky (False)	Mediastinal Lung Adrenal	10
CP5	Adenocarcinoma	IV	6.41	Paucimetastatic Non-Bulky	Mediastinal Lung	10

To check the potential information hidden in these patterns, several statistical and probabilistic data analysis methods were applied. As a first approach, all raw data, including debris, PBMCs and CTCs (**Fig. 3.5A**), were profiled by using kernel

density estimates of their distribution (**Fig. 3.5B**). [37] In these distributions, healthy individuals show two cell populations (corresponding to the two peaks of the distribution) as compared with the single, broader cell cluster exhibited by the patients. Motivated by the observation of distinct cell populations, especially in the case of healthy individuals, Gaussian mixtures were used to model each distribution (**Fig. 3.5C**). [37] These models uncover several characteristic fingerprints. First, all healthy donors present a cell population at high CD45 intensities (over 1000). Second, two other populations are clustered at intensities in the 10-100 range for both 2-NBDG and CD45. In contrast, the high CD45 intensity population is absent for all patients while the single collection at lower CD45 intensity showed in **Fig. 3.5B** results in three subgroups that are characteristic of the patient diagnostic/prognostic.

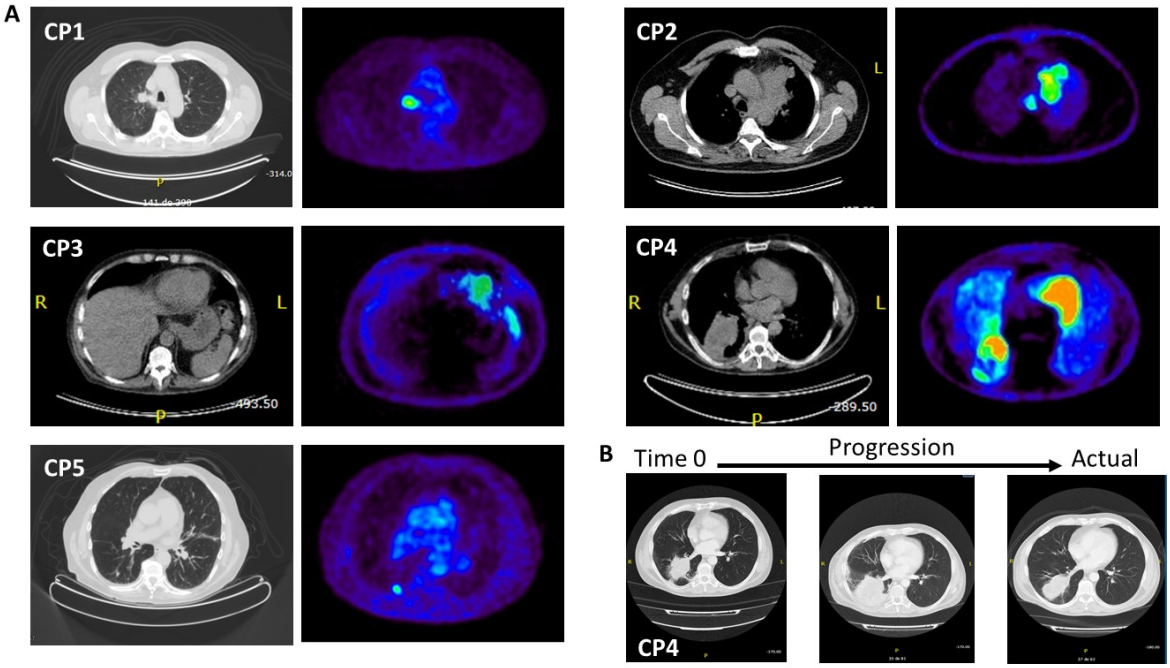

FIGURE 3.3 (A) Cross-sectional CT and PET-CT scans corresponding to the maximum size of the primary tumor from five patients. All patients are in stage IV (metastatic) but with different extensions and size of the primary tumor. CP1, adenocarcinoma patient with a non-bulky primary tumor, but with a very wide metastatic extension (subcutaneous); CP2 and CP3, CA patients with large primary tumors (bulky) but with limited extensions of metastasis; CP4, *a priori*, patient with a large primary

[37] Pedregosa, F.; Varoquaux, G.; Gramfort, A.; Michel, V.; Thirion, B.; Grisel, O.; Blondel, M.; Prettenhofer, P.; Weiss, R.; Dubourg, V.; Vanderplas, J.; Passos, A.; Cournapeau, D.; Brucher, M.; Perrot, M.; Duchesnay, E. *J. Mach. Learn. Res.* **2011**, *12*, 2825.

tumor (bulky) with limited extension of metastasis (see B); CP5, patient with a non-bulky primary tumor with limited extension of metastasis. (B) CT scan cross-sections showing the tumor progression of CP4 with treatment.

Notably, according to these graphs, the cancer patients can be subcategorized in three different groups: CP1, CP2-3, and CP4-5. Independently, the distributions of the raw data were compared by using the two-dimensional KS statistic[38,39] to acquire an unsupervised clustering of individuals (**Fig. 3.6**). In particular, the distance between pairs of distributions was computed. Then, hierarchical clustering was applied to group the individuals. Again, healthy individuals are clearly separated from patients while patients are classified in the same three subgroups as before: CP1, CP2-3, and CP4-5. Notably, this categorization in three subgroups only partially agrees with that arising from CTC quantification (i.e., CP1, CP4-5: *low CTC content*; vs. CP2-3: *high CTC content*; see **Table 3.1**). Notwithstanding, these different interpretations of the cytograms may reveal two complementary dimensions of the disease. The first one, CTC enumeration, takes account of the disease burden while the other, the analysis of the cell population pattern, appears to correlate well with the disease extension. This latter observation is clearly corroborated by the results of the CT and PET scans images and the volume of the primary tumor (**Fig. 3.3A**).

[38] Fasano, G.; Franceschini, A. *Mon. Not. Roy. Astron. Soc.* **1987**, *225*, 155.
[39] Press, W. H.; Teukolsky, S. A.; Vetterling, W. T.; Flannery, B. P. *Numerical Recipes in C: The Art of Scientific Computing*; Cambridge University Press, 1992.

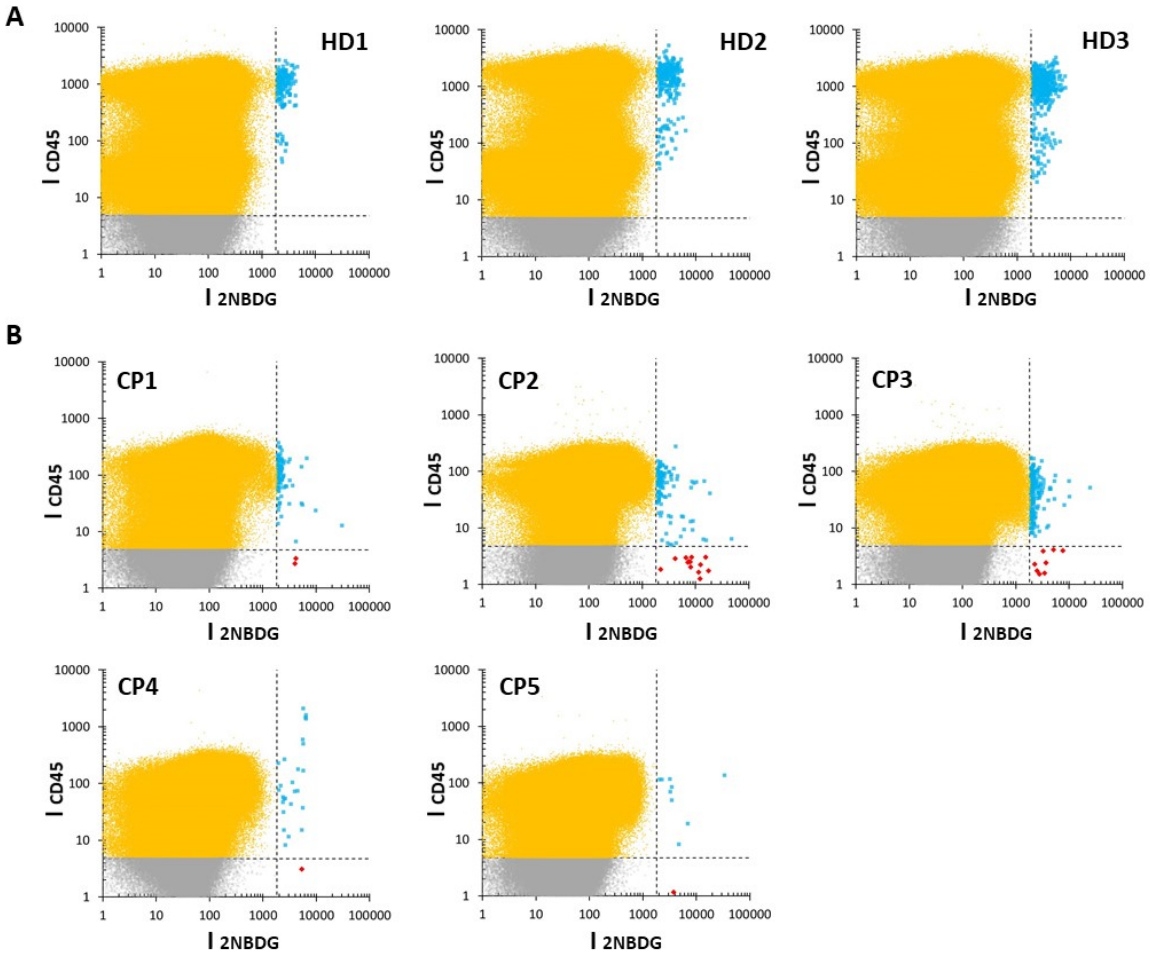

FIGURE 3.4 Flow cytometry data of samples obtained from (A) healthy donors and (B) lung cancer patients, as a function of 2NBDG and CD45 fluorescence emissions.

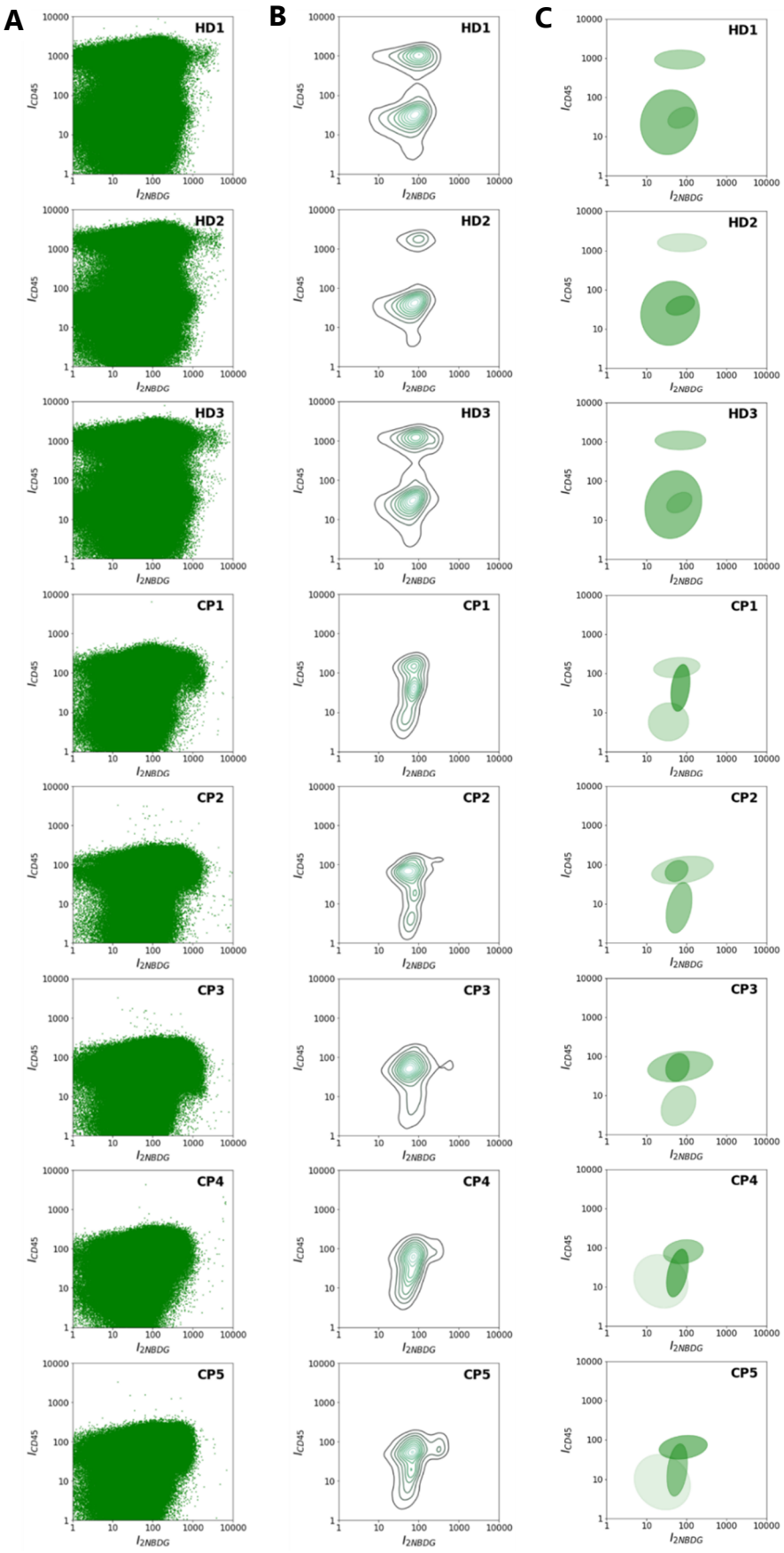

FIGURE 3.5. (A) Uncategorized flow cytometry raw data, as a function of 2-NBDG and CD45 fluorescence emissions; (B) kernel density estimate of the distribution and (C) Gaussian mixture models, of PBMC samples obtained from healthy donors (HD) and lung cancer patients (CP).

In this regard, by applying conventional radiological criteria, the disease can be defined as multimetastatic (extensive) or paucimetastatic (limited), while the volume of the primary tumor can be differentiated as bulky or non-bulky. Following these conventionalisms, CP1 presents a more extended disease (multimetastatic, lung, mediastinal, subcutaneous and skin) with no dominant localization, not even in the primary tumor (non-bulky). The rest of the patients (CP2-5), however, display a limited disease (paucimetastatic) but with different volumes in the primary tumor, bulky for CP2-3 (active disease) and non-bulky for CP5 (in remission). In the case of CP4, again, the monitoring of the disease with imaging techniques (**Fig. 3.3B**) revealed that the initial bulky disease shown in the CT and PET scans (**Fig. 3.3A**) was paradoxical and that could be ascribed to the immunotherapy (clinical evolution showed that a considerable part of the supposed tumor mass was due inflammation and infection, **Fig. 3.3B**).

This metabolic liquid biopsy (MLB) radically redefines the sensing strategy, profiting from the different consummation of glucose by tumor cells as compared with healthy ones (Warburg effect). [35] With this approach, two complementary layers of information are provided. Firstly, by using a metabolic feature universally shared by all tumor cells, MLB has the capability of discriminating and quantifying all CTCs (mesenchymal and epithelial) rather than only the epithelial subgroup as for conventional phenotypical LBs. Secondly, as MLB also labels all PMBCs, it is possible to extract metabolic patterns using appropriate statistical and probabilistic analysis which informs about the impact of the CTC presence on the rest of the non-cancer cells. Thus, by applying two independent statistical approaches to the cytometric data, another dimension of the disease is profiled by revealing a new class of adaptive metabolic pattern biomarker (AMPB), which describes the extension of the disease as a function of the number of metastasis. Within our cohort, were selected patients with lung cancer at the same disease stage but different disease distribution (defined radiologically with CT and PET scans). The selection was made based on (i)

the presence or not of a bulky tumor (massive primary tumor), and (ii) the extent of the metastasis. This last feature was defined as the presence of more or less than 3 metastatic sites (multi- vs. pauci-metastatic disease) that would correspond to the stages M1a/M1b. Based on the CTC enumeration, patients were discriminated into those with high (CP2-3) and low (CP1, CP4-5) load of tumor cells. Subsequently, the AMB extracted from MLB clearly defined, for patients at the same clinical stage, the presence or absence of a primary tumor mass (bulky); a condition which is mostly related to the overall number of CTCs. It is worth reminding that CP4 is the patient who presented a paradoxical response in the PET because of immunotherapy and inflammation.

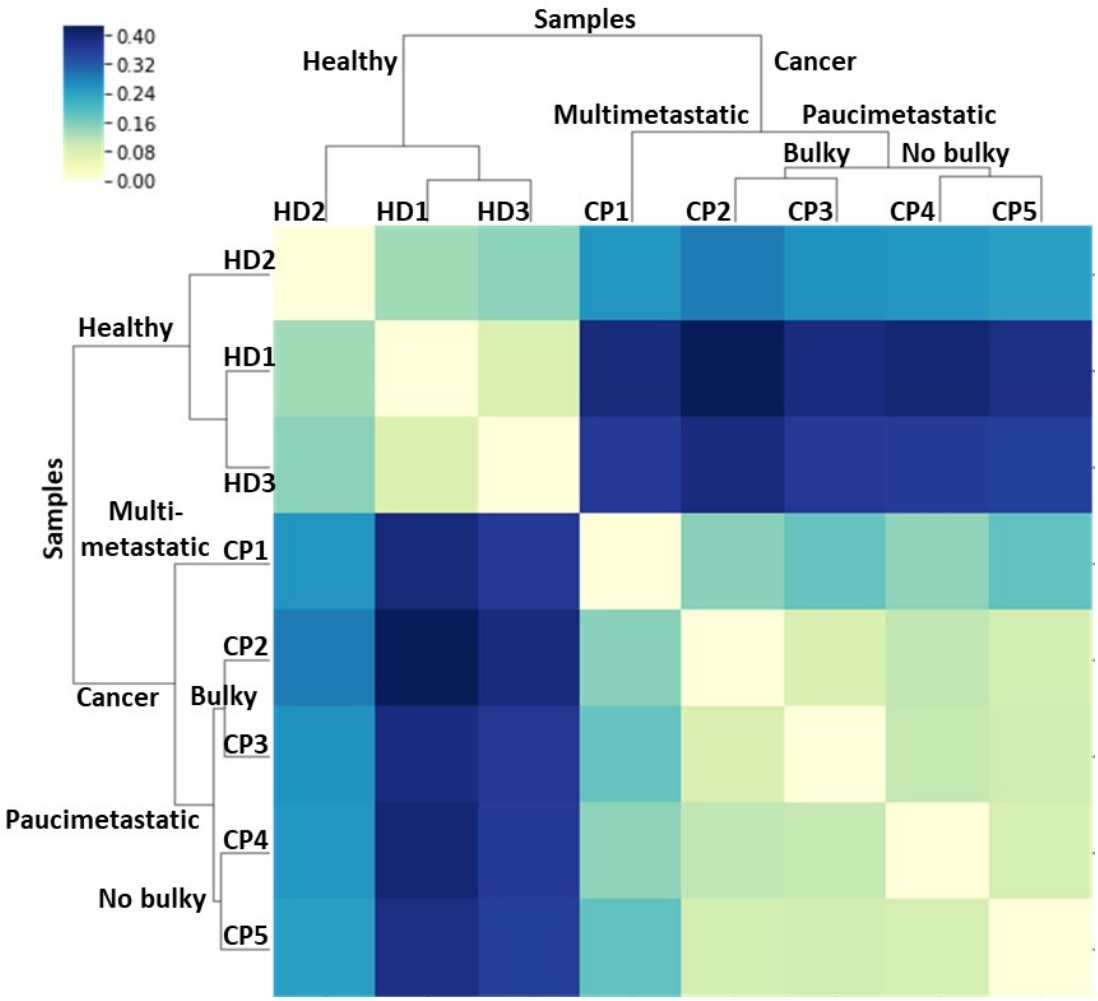

FIGURE 3.6 Unsupervised hierarchical clustering of healthy donors and cancer patients. From the distribution of the raw data, distances between all pairs of samples were calculated using the two-dimensional KS statistic.[38] Then individuals where grouped using hierarchical clustering.

While described for diagnosis and stratification in patients with radiologically stage IV lung cancer, can be believe that this MLB approach may be also amenable to the detection of true stages IV when the radiological diagnosis inaccurately establishes a stage I or II (30%-40% of relapses after radical surgery). In these situations, unnecessary surgery could be avoided. On the other hand, in stages III, where a very heterogeneous prognosis occurs (from 13% to 36% of 5-years survival rate), MLB would allow to rescue those patients susceptible of curative surgery. Joining a list of recent next-generation diagnostics (circulating tumor cell assays,

biomarker monitoring), MLB-coupled to big data analysis (adaptive metabolic biomarker, AMB) aims to build toward early identification, prognosis and staging of metastatic disease that may result in improved patient outcomes and decreased treatment toxicities. With a growing population of patients at risk of developing lung metastasis, a highly sensitive, nonsurgical, nonradioactive method for repeated monitoring may be clinically useful. Validation of our findings with prospective clinical trials testing therapeutic strategies based on MLB assessment will be required to establish clinical utility.

3 Conclusions

Here, it is demonstrated the applicability of this unbiased detection strategy to (i) establish a more precise correlation between CTCs quantification and the actual burden of disease, therefore improving the accuracy of staging based on current imaging techniques (TNM), and (ii) recognize different categories of disease within a single stage (stage IV). Firstly, the conditions were optimized for the selective labeling of CTCs, extracted from human blood samples through a partial enrichment method (Ficoll), for their identification and quantification independently of their phenotypic features. With this approach, all subpopulations of CTCs can be detected regardless of the histological characteristics of the primary tumor and the molecular variability associated with different stages of the EMT process. Secondly, by applying statistical analysis techniques and probabilistic models to the metabolic status and distribution of peripheral blood mononuclear cell (PBMC) populations "perturbed" by the presence of CTCs, a new category of adaptive metabolic pattern biomarker (AMPB) is described and unambiguously correlated to the different clinical stages of the patients.

4 Experimental section

Study Design and Patients

The set of patients selected for this study was identified from patients treated between 2016 and 2017. Five of them were recruited with the primary goal of analyzing the association of the number of CTCs and the metabolic distribution of PBMCs with the diagnostic of lung cancer. Eligible patients included in this study were age ≥ 18 years with treated primary lung cancers at stage IV with either non-small cell lung cancer (NSCLC) (adenocarcinoma and squamous cell carcinoma) or small cell lung cancer (SCLC) histology and receiving treatment with chemotherapy or immunotherapy. Eligible patients underwent pretreatment imaging by chest CT and whole-body PET-CT. All patients underwent pretreatment brain MRI. Patients were chosen based on the volume of their primary tumor, considering two categories were considered: (i) tumor size (bulky, > 4 cm, and non-bulky, < 4 cm); and (ii) metastasis extension (extended or multimetastatic, >3 M1a/M1b, and not-extended or paucimetastatic, <3 M1b). Healthy adult blood donors were recruited through the Grupo HM Hospitales. Personal and clinical data were recorded according to standard clinical procedures. All samples were collected with informed consent and institutional review board approval in accordance with the Declaration of Helsinki.

Clinical samples

Personal and clinical data were recorded according to standard clinical procedures. All specimens were obtained with informed consent. The study was approved by the local Ethics and Clinical Research Committee. 8 mL of blood was

drawn in 10 mL vacutainer tubes containing EDTA and processed in the first 24 h. Results for CTCs were linked to clinical data.

Cell Cultures

A549 lung cancer cells were obtained from the American Tissue Culture Collection (ATCC, Manassas, VA, USA) and cultured in RPMI 1640 media supplemented with 10% fetal bovine serum. Cells were maintained at 37ºC in a humidified 5% CO_2 atmosphere.

Preparation of samples

Blood samples from cancer and healthy patients were obtained from the Servicio de Oncología Clínica of the HM Hospital Universitario Torrelodones-Madrid. Peripheral blood mononuclear cells (PBMCs) were isolated from the whole blood using Ficoll-Paque PLUS (purchased from GE Healthcare Life Science). 15 mL of Ficoll solution was added to a 50 mL Leucosep Centrifuge tubes (Greiner Bio One) and blood was disposed as a layer onto Ficoll. Samples were centrifuged at 800g for 15 min at 18^0C, and the resulting PBMCs layer was separated from the rest of phases. PMBCs were washed twice in 10 mL PBS by centrifugation at 250g for 10 min and finally suspended in RPMI 1640 supplemented with 10% FBS, until use.

Cell Lines Uptake

A certain amount of A549 cancer cells were spiked into collected PBMCs from healthy donors. Cells were pelleted and placed in 100 µL PBS 10% FBS, 4 µL anti-CD45-APC (for leucocytes staining) or anti-CD14-PerCP/Cy5.5 (for monocytes), were added. Additionally, 100 µL of 2NBDG at different concentrations were studied, 50 µM, 300 µM and 600 µM; in time, 10 min, 30 min and 60 min. After, cells were washed twice by centrifugation at 250g for 10 min and suspended in cold-PBS. Same procedure was followed to study the oxygen availability (normoxia, hyperoxia or hypoxia) effect on the uptake, choosing 300 µM 2NBDG and 30 min as optimal conditions. More, different amounts of A549 cancer cells were selected and spiked into the blood: 10,000; 1,000; 100 and 10 cells for 1×10^6 PBMCs. The same amounts of stains were added and 300 µM and 30 min of time under hypoxia conditions were used for the 2NBDG incubation.

Healthy and Cancer patient blood uptake

PBMCs from cancer patients enrolled in the study were directly pelleted and placed in 100 µL PBS 10% FBS. 100 µL of 2NBDG 300 µM and 4 µL of anti-CD45-APC (for leukocyte staining), were added for 30 min, under hyperoxia at RT. After, cells were washed twice by centrifugation at 250 g for 10 min and suspended in cold-PBS.

Sample measurement with the flow-cytometer

Flow cytometry of the samples was carried out in a NovoCyte Flow Cytometer (from AceaBiosciences), equipped with a 488 nm and 640 nm excitation lasers and 530/30 nm and 675/30 nm detection filters. 488 nm blue laser and 530/30 nm filter were used for the excitation and collection of 2NBDG staining, 675/30 nm filter was used to collect fluorescence from PerCP/Cy5.5 excited with the same laser. 640 nm red laser and 675/30 nm filter were used for excitation and emission collection from APC dye. Cytometric data were analyzed with NovoExpress and FloJo VX software and Microsoft Excel.

Statistical analysis and probabilistic modelling

The kernel density estimates and the Gaussian mixture models were obtained using the Scikit-learn Python module. [37] The Gaussian mixture models were fitted (including full covariances) using variational inference with a fixed number of components (n=3). The two-dimensional KS statistic was calculated using our own implementation of the algorithm described in ref. 38, based on the implementation in ref. 39. Because calculation of the two-dimensional KS statistic is computationally demanding, we used 50% of each dataset for all pairwise comparisons.

CHAPTER 4

UNIVERSITAT ROVIRA I VIRGILI
NANO/MICROSYSTEMS FOR CANCER DIAGNOSIS AND THERAPY
Manuel García Algar

Proteomic liquid biopsy through detection of c-MYC transcription factor

The oncoprotein *c-MYC*, a transcription factor that has been shown to be deregulated in up to 70% of human cancers, can be used as a robust proteomic signature for the successful diagnosis of cancer disease. Herein, the development of a rapid, highly specific and sensitive surface-enhanced Raman scattering (SERS) assay for the quantification of *c-MYC* in real blood samples, will be presented and discussed. The sensing scheme relies on the use of specifically designed hybrid plasmonic materials and their bioderivatization with a selective peptidic receptor modified with a SERS transducer. Peptide/*c-MYC* reorganization events translate into measureable alterations of the SERS signature associated with a molecular reorientation of the transducer. The efficiency of the sensor is demonstrated in tumor cellular lines and blood from healthy donors and a cancer patient.

1 Introduction

Description and characterization of tumor molecular basis is routinely applied in clinical oncology practices in order to guide treatment decisions. Typically, these biochemical analyses are performed on solid tissues which have been acquired through an invasive biopsy. Due to surgery procedures, this challenging methodology becomes costly, painful and potentially risky for the patient. Thus, new noninvasive methods to detect and monitor tumors suppose a major need in

oncology. In this scenario, blood-based biomarkers or liquid biopsy[1], have a considerable potential to solve this problem. As mentioned in Chapter 1, circulating tumor cells[2] and circulating tumor DNA/RNA[3] are options, alongside protein markers. However, the protein expression patterns in plasma circulating tumor cells as well as in peripheral blood mononuclear cells fractions remain largely unexplored.[1]

Recognition and quantification of proteins in blood is commonly performed with conventional immunological and molecular biology methods,[4] such as western blotting (WB) or enzyme linked immunosorbent assay (ELISA). Although robust, these techniques are tedious, lengthy, time-consuming, expensive and with low sensitivity in the case of WB, especially for the usually low concentrations in blood of some analytes. Thus, many efforts have moved to develop new analytical tools able to overcome these limitations.

Since, surface-enhanced Raman scattering (SERS) spectroscopy[5] has emerged as an excellent alternative technique for the interrogation of specific analytes, has been successfully used for the direct ultrasensitive quantification of prionic,[6] green[7] or yellow proteins[8], among other examples[9]. However, several limitations in reproducibility, sensitivity and selectivity can appear when measuring high molecular weight molecules, i.e. proteins[10], due to changes in the interaction with plasmonic surfaces, poor SERS cross section of these targets and the complexity of

[1] Buder, A.; Tomuta, C.; Filipits, M. *Current Opinion in Oncology* **2016**, *28*, 130.
[2] Ignatiadis, M.; Lee, M.; Jeffrey, S. S. *Clinical Cancer Research* **2015**, *21*, 4786.
[3] Crowley, E.; Di Nicolantonio, F.; Loupakis, F.; Bardelli, A. *Nature Reviews Clinical Oncology* **2013**, *10*, 472.
[4] Garner, M. M.; Revzin, A. *Nucleic Acids Research* **1981**, *9*, 3047.
[5] Schlucker, S. *Angewandte Chemie-International Edition* **2014**, *53*, 4756.
[6] Alvarez-Puebla, R. A.; Agarwal, A.; Manna, P.; Khanal, B. P.; Aldeanueva-Potel, P.; Carbo-Argibay, E.; Pazos-Perez, N.; Vigderman, L.; Zubarev, E. R.; Kotov, N. A.; Liz-Marzan, L. M. *Proceedings of the National Academy of Sciences of the United States of America* **2011**, *108*, 8157.
[7] Habuchi, S.; Cotlet, M.; Gronheid, R.; Dirix, G.; Michiels, J.; Vanderleyden, J.; De Schryver, F. C.; Hofkens, J. *Journal of the American Chemical Society* **2003**, *125*, 8446.
[8] Singhal, K.; Kalkan, A. K. *Journal of the American Chemical Society* **2010**, *132*, 429.
[9] Lin, L.; Tian, X. D.; Hong, S. L.; Dai, P.; You, Q. C.; Wang, R. Y.; Feng, L. S.; Xie, C.; Tian, Z. Q.; Chen, X. *Angewandte Chemie-International Edition* **2013**, *52*, 7266.
[10] Han, X. X.; Zhao, B.; Ozaki, Y. *Trac-Trends in Analytical Chemistry* **2012**, *38*, 67.

biological fluids matrixes. A possible solution relies on the functionalization of the plasmonic substrate with chemical species, or *chemoreceptors*, displaying high SERS cross section and binding affinity and specificity for the target protein.[11] This indirect approach, bases the detection on the spectroscopic changes in the chemoreceptor SERS signature leaded by its molecular reorientation when binding with the target.[12] Species such as antibodies, aptamers or peptides can be used as a chemoreceptors. Despite their remarkable small SERS activity which severely limits their application for direct ultradetection, by derivatizing their molecular structure with terminal moieties with higher SERS cross section and affinity for the target and the plasmonic substrate, this issue can be solved.[13] However, the molecular structure of chemoreceptors plays an important role for their interaction with protein target and their affinity should not result affected by addition of terminal moieties.

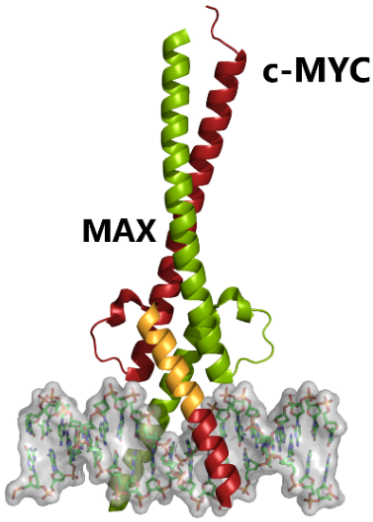

FIGURE 4.1 Structure of proto-oncogene *c-MYC* protein (in red) interacting with *MAX* (in green). H1 domain used in the sensing platform is highlighted in yellow.

[11] Alvarez-Puebla, R. A.; Liz-Marzan, L. M. *Chemical Society Reviews* **2012**, *41*, 43.
[12] Guerrini, L.; Arenal, R.; Mannini, B.; Chiti, F.; Pini, R.; Matteini, P.; Alvarez-Puebla, R. A. *Acs Applied Materials & Interfaces* **2015**, *7*, 9420.
[13] Guerrini, L.; Pazos, E.; Penas, C.; Vazquez, M. E.; Mascarenas, J. L.; Alvarez-Puebla, R. A. *Journal of the American Chemical Society* **2013**, *135*, 10314.

In this chapter, a proteomic-based liquid biopsy method is described for the efficient detection and quantification of the oncogenic protein *c-MYC*. The protein *c-MYC* (**Fig. 4.1**) consists in a helix-loop-helix leucine zipper (bHLHZ) transcription factor encoded by the corresponding *c-myc* gene that plays an important role in coordinating cellular metabolism with cell cycle and has been shown to be elevated or deregulated in up to 70% of human cancers.[14] Oncogenicity of c-MYC has been observed to be associated with loss of transcriptional control leading its overexpression and accumulation in tumor cells.[15] Additionally, it works as a universal gene expression amplifier of all active promoters during transcription events.[16] Thus, the evaluation of the concentration of c-MYC protein in cells circulating in blood can serve as a criteria for the diagnosis and monitoring of tumors. Taking into consideration all issues mentioned above, a SERS-active peptide-conjugated sensor has been constructed for the efficient recognition and quantification of c-MYC in blood.

[14] Dang, C. V. *Cell* **2012**, *149*, 22.
[15] Helm, F.; Kammertoens, T.; Lehmann, F. M.; Wilke, A.; Bruns, H.; Mautner, J.; Bornkamm, G. W.; Gerbitz, A. *Plos One* **2013**, *8*.
[16] Nie, Z. Q.; Hu, G. Q.; Wei, G.; Cui, K. R.; Yamane, A.; Resch, W.; Wang, R. N.; Green, D. R.; Tessarollo, L.; Casellas, R.; Zhao, K. J.; Levens, D. *Cell* **2012**, *151*, 68.

2 Results and Discussion

Sensing strategy

For the construction of the sensing platform, positively charged silica microbeads (8 µm diameter) were homogenously coated with citrate-stabilized silver nanoparticles (AgNP, 65 nm diameter) biofunctionalized with a chemoreceptor. Electrostatic deposition of AgNPs onto silica microbeads offers large surface area, close adsorbent-adsorbate interaction and high density of electromagnetic hot spots formed between plasmonic particles, which allows to increase SERS intensity. In **Fig. 4.2** is observed how AgNPs can be successfully deposited onto microbeads (SiO_2@AgNP) as localized surface plasmon resonance (LSPR) profile shifts to an intense and broader feature at longer wavelengths.

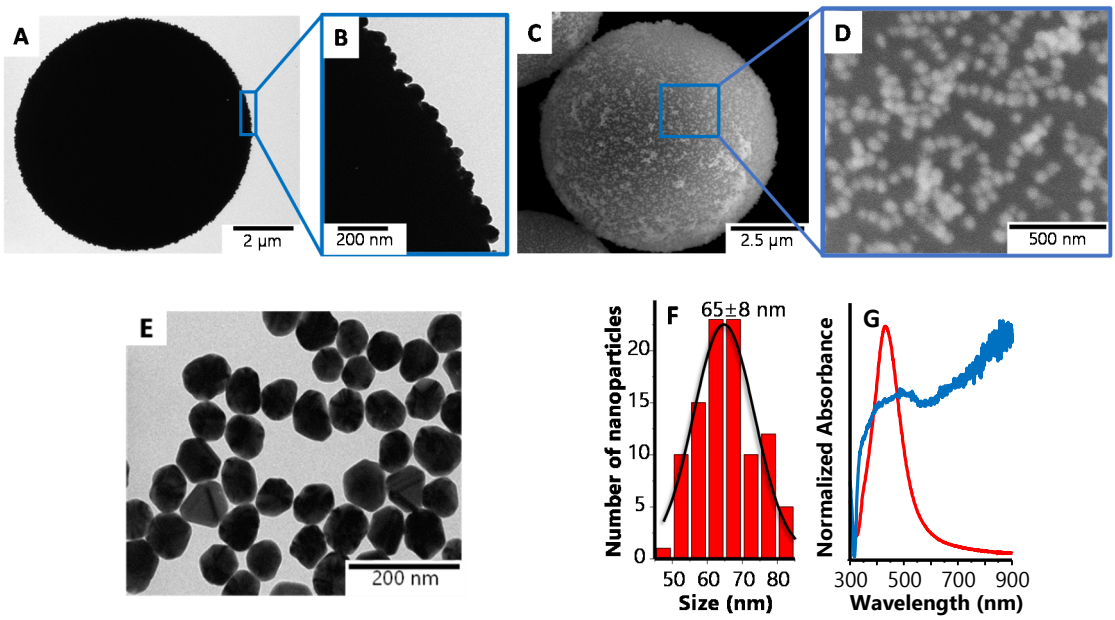

FIGURE 4.2 Characterization of silica microbeads with silver nanoparticles deposited onto. (A, B) TEM micrographs and (C, D) ESEM images show the homogeneous coverage of AgNPs through the microbead surface. (E) TEM micrograph of citrate-capped monodisperse AgNPs and (F) size distribution of 65±8 nm diameter. (G) UV-visible absorbance of AgNPs in solution (in red) and deposited onto microbeads (in blue).

In this particular case, our collaborator Prof. Mascareñas (Universidad de Santiago de Compostela), synthesized the selected chemoreceptor (H1). This last is based on a double mutant peptide (residues Ser^{520} → Ala, Phe^{522}→ Ala), derived from the chain 1 of the helix-loop-helix region (**Fig. 4.3**) of c-MYC structure, which is known to interact with the protein with high selectivity and affinity.[17] The low SERS cross section of the selected H1 receptor can be overcome by the addition of a SERS moiety 4-mercaptobenzoyl (MB) to the side chain amino group of a Lys residue appended at the C-terminus of the H1 peptide. Such modification should not alter the intrinsic helical propensity of the peptide, or its c-MYC binding properties. Mercapto-group present in MB unit from the MB-H1 receptor, tends to show high affinities for metallic surfaces[18], i.e. silver, resulting in a covalent anchorage of MB-H1 to deposited silver nanoparticles. Detected SERS signature for MB when studying the resulting complex SiO_2@AgNP@MB-H1 with a good signal-to-noise ratio, indicate the attachment of MB-H1 to SiO_2@AgNP (**Fig. 4.4**).

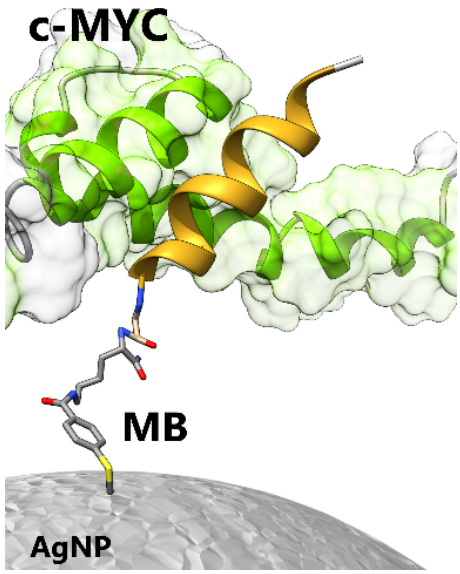

FIGURE 4.3 Scheme of the sensing platform for the c-*MYC* protein detection. H1 peptide (in yellow) recognizes c-*MYC* homologous domain (in green). MB SERS moiety is used to attach the structure to AgNP surface through a covalent interaction.

[17] Draeger, L. J.; Mullen, G. P. *Journal of Biological Chemistry* **1994**, *269*, 1785.
[18] Mir-Simon, B.; Reche-Perez, I.; Guerrini, L.; Pazos-Perez, N.; Alvarez-Puebla, R. A. *Chem. Mat.* **2015**, *27*, 950.

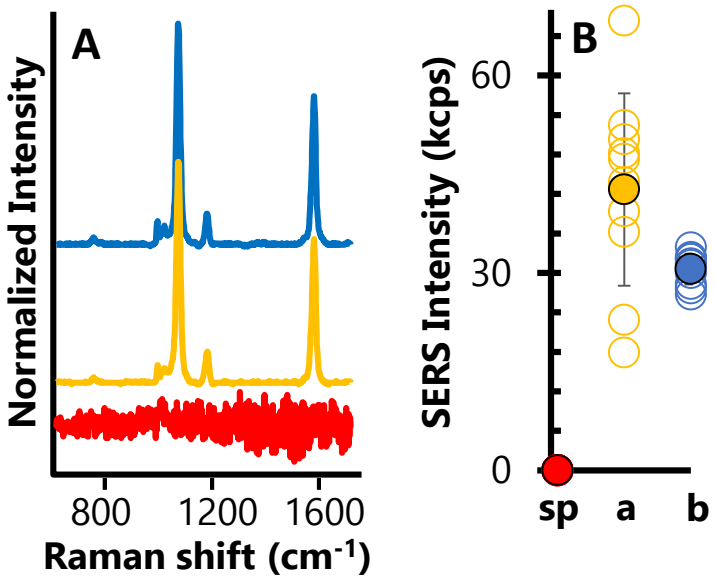

FIGURE 4.4 SERS measurement for SiO_2@AgNP@MB-H1. (A) SERS signature of MB moiety is detected when AgNPs are deposited (in blue) onto silica microbeads which is comparable to aggregate particles onto a glass slide (yellow) to form hot-spots. No SERS signal is observed when non-aggregated evidencing the necessity of interparticle hot-spot coupling. (B) Similar SERS intensities are registered for deposited particles as aggregating them in a glass slide. *sp = single particles; a= aggregated; b=deposited*.

Sensor performance and c-MYC detection in human blood

The large size of these beads allows for their easy localization and measurement with a low magnification objective (i.e. x5) for the laser scanning with a higher resolution objectives (i.e. x50 or x100). This paves the way for a drastic reduction of the amount of plasmonic material required for sensing, which in turns improve the sensitivity by increasing the number of molecules per bead ratio. As an example, SERS signature of MB-H1 is distinguishable down to 10 pM when measuring a particle concentration of 2400 beads/mL, while lower amounts 240 beads/mL allow for detection down to 1 pM (**Fig. 4.5**).

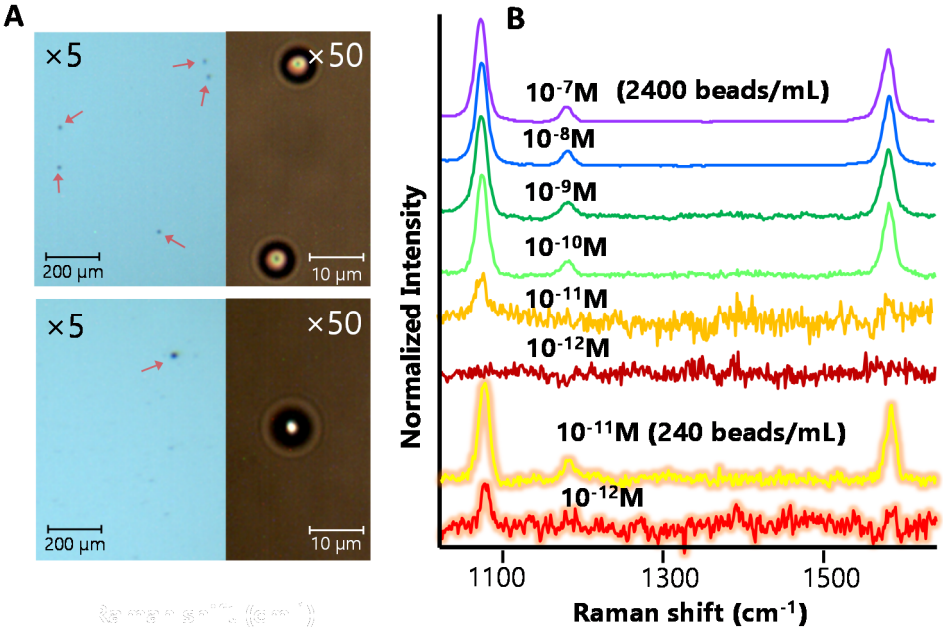

FIGURE 4.5 (A) Optical images of microbeads at low (x5) and high (x50) magnification at 2400 beads/mL (upper panel) and 240 beads/mL (bottom panel) of concentration. (B) SERS signatures for MB-H1 at different concentrations of MB.

Capturing of c-MYC by SiO_2@AgNP@MB-H1 could result in a large set of different perturbations on the SERS signature of the MB moiety due to the massive size of the protein (57 kDa), from subtle shifts of vibrational features to the

appearance of new bands. In fact, a drastic intensity increase of the N-C stretching mode (characteristic band at 1022 cm^{-1}) upon conjugation with c-MYC can be observed. Taking into account that the SERS spectra results from the contribution of interacting (associated to 1075 cm^{-1} band) and non-interacting (associated to 756 cm^{-1} band) MB-H1 molecules, instead of monitoring the absolute intensity, a ratiometric measurement of the intensities at I_{756}/I_{1075} was used for the quantification of c-MYC amount (**Fig. 4.6**).

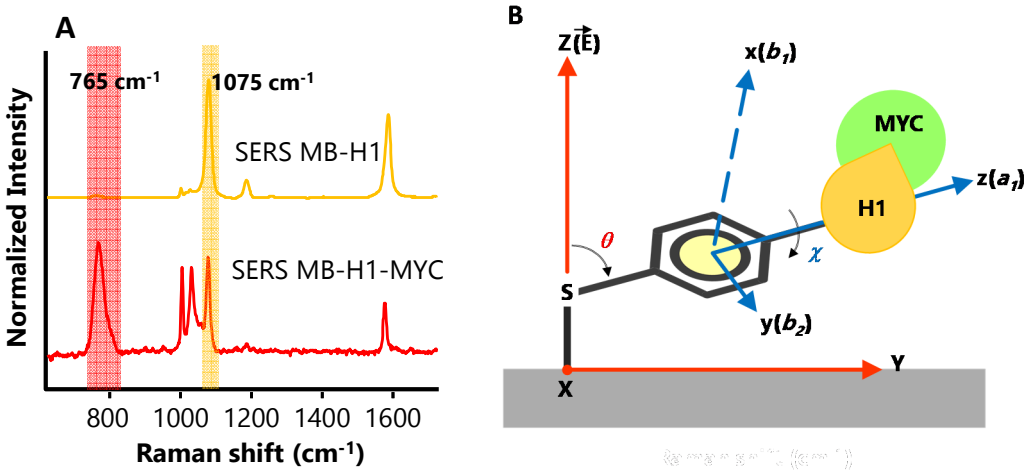

FIGURE 4.6 (A) SERS profile for MB-H1 peptide (yellow) and after c-MYC binding (red). Characteristic band for free peptide is maintained at 1075 cm^{-1} even after protein interaction, band at 765 cm^{-1} appear as binding indicator. (B) Estimation model of the molecular orientation of MB-H1-MYC.

Feasibility of the developed sensor for liquid biopsy applications can be demonstrated with both tumor cell lines and real human samples from patients, by comparing results with conventional ELISA quantification assay (**Fig. 4.7**).

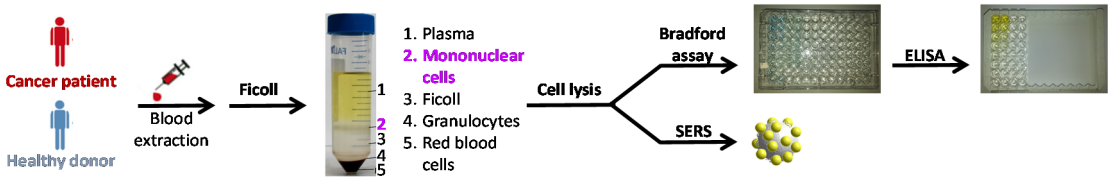

FIGURE 4.7 Schematic representation of c-MYC amount quantification in blood cells from a cancer patient and a healthy donors both using conventional ELISA assay and SERS sensor.

In fact, ELISA and SERS show adequate correlation coefficients (**Fig. 4.8**) with analogous c-MYC detection limits when measuring c-MYC standards of known concentration, with a slightly larger standard deviation for the developed optical method. However, SERS results are obtained in shorter preparation times than ELISA which requires lengthy 4-5h of assay. Notably, successful detection and quantification of the protein is achieved when measuring tumor cells (i.e. MCF-7 cells).

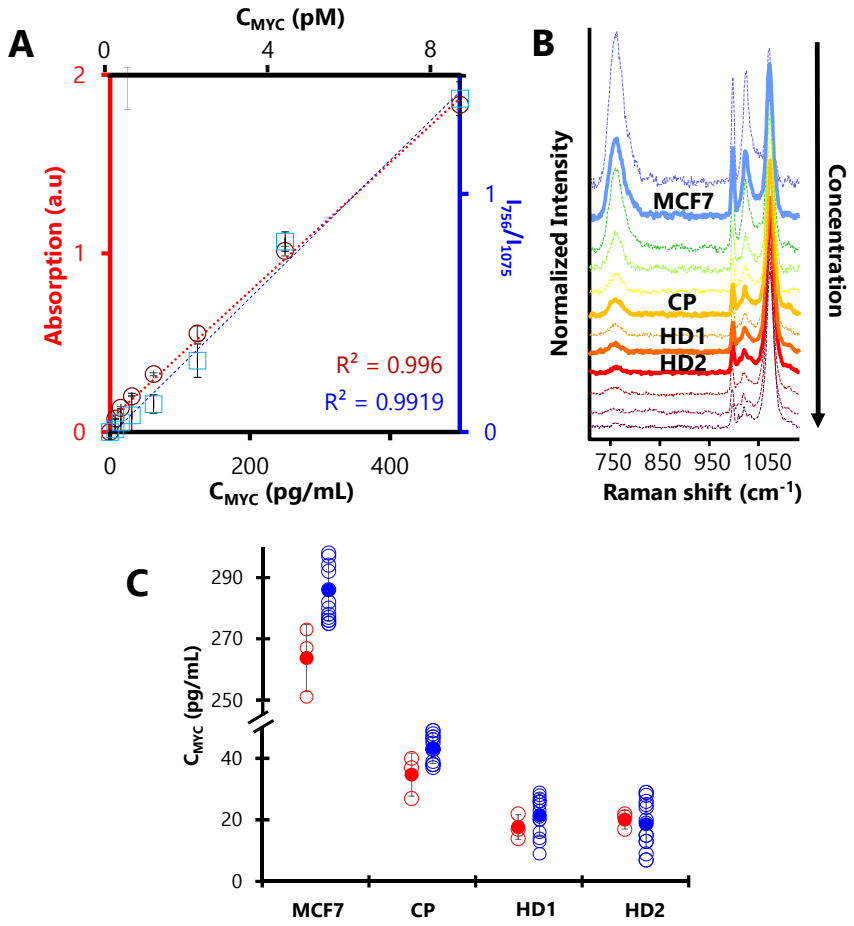

FIGURE 4.8 (A) Calibration curve for ELISA (red) and optical SERS sensor (blue). (B) Corresponding SERS spectra recorded for each standard of the calibration curve and real samples measured. (C) Quantification of MCF-7 cell line, a cancer patient (CP) and two healthy donors (HD) with both ELISA and sensor.

As shown in **Fig. 4.8C**, the evaluation of proteome for MCF-7 tumor cells reveals high concentration for c-MYC protein due to the cancerous nature of those

cell line. Despite a drastic reduction in c-MYC amount is observed when analyzing protein content from real human samples, remarkable differences can be found. Since blood from patient suffering cancer disease can contain a small fraction of tumor cells (CTCs) show slightly higher c-MYC levels, in contrast to low values encountered for healthy donors.

3 Conclusions

In this chapter, a rapid, high specific and sensitive SERS sensing platform has been described for the efficient detection of oncoprotein c-MYC as liquid biopsy alternative. The sensing scheme relies on the use of specifically designed hybrid materials consisting in silica microbeads coated with interacting silver nanoparticles. The metallic surface of colloids are bioderivatized with a c-MYC binding domain modified with a 4-mercaptobenzoyl antenna (MB-H1) that transduces the c-MYC recognition events into measurable alterations of the SERS signature from MB-H1. The extent of such spectral changes allows for a quantitative analysis of the c-MYC protein levels into real human samples, demonstrating the potential utility of the method as a liquid biopsy approach.

4 Experimental section

Materials

DMF and TFA were purchased from *Scharlau,* CH_2Cl_2 from *Panreac,* and CH_3CN from *Merck.* Dihydrated trisodium citrate (≥99.5%), L-ascorbic acid (≥99.0%), silver nitrate (≥99.9999%), magnesium sulfate (99.5%), polyethylenimine branched (PEI, 25000), and the rest of the reagents were acquired from *Sigma-Aldrich*. Silica microbeads of 7.75 μm in diameter were acquired from *Microparticles GmbH*. Recombinant Human c-MYC was purchased from *Creative BioMart*. All solvents were dry and synthesis grade, unless specifically noted, and all reactants were used without further purification. Milli-Q water (18 MΩ cm^{-1}) was used in all aqueous solutions, and all glassware was cleaned with aqua regia before the experiments.

Instrumentation

UV–vis spectra were recorded using a *Thermo Scientific Evolution 201* UV–vis spectrophotometer. Peptide concentration was calculated by the Lambert−Beer law using an extinction coefficient of 11862 M^{-1} cm^{-1} at 310 nm. Silver concentration for AgNPs was calculated using extinction coefficient of 6.61×10^{10} M^{-1} cm^{-1}.[18,19,20]

Electron micrographs were recorded with a transmission electron microscopy (*JEOL JEM-1011* operating at 80 kV) and an environmental scanning electron microscopy (*JEOL 6400*) for the structural characterization of the samples.

SERS experiments were conducted using a *Renishaw InVia Reflex* confocal microscope equipped with a 1200 grooves mm^{-1} grating for the NIR wavelengths,

[18] Mir-Simon, B.; Reche-Perez, I.; Guerrini, L.; Pazos-Perez, N.; Alvarez-Puebla, R. A. *Chem. Mat.* **2015**, *27*, 950.
[19] Mir-Simon, B.; Morla-Folch, J.; Gisbert-Quilis, P.; Pazos-Perez, N.; Xie, H.-n.; Bastus, N. G.; Puntes, V.; Alvarez-Puebla, R. A.; Guerrini, L. *Journal of Optics* **2015**, *17*.
[20] Paramelle, D.; Sadovoy, A.; Gorelik, S.; Free, P.; Hobley, J.; Fernig, D. G. *Analyst* **2014**, *139*, 4855.

additional band-pass filter optics, and a 2D-CCD camera. All spectra were acquired using 785 nm laser excitation by focusing the laser onto the sample with ×5 or ×50 objectives.

Synthesis of citrate-stabilized spherical silver nanoparticles

Spherical silver nanoparticles of approximately 65 nm in diameter were produced by a modification of the previously reported protocol.[18,19] Briefly, 250 mL of Milli-Q water were heated to reflux under strong magnetic stirring. Once it boils energetically, a mixture containing ascorbic acid (250 µL, 0.1 M) and trisodium citrate (3.41 mL, 0.1 M) was added. After 1 minute, a solution containing $AgNO_3$ (744 µL, 0.1 M) and $MgSO_4$ (559 µL, 0.1 M), previously incubated for 5 min at room temperature, was injected into the reaction vessel under vigorous stirring. Boiling and stirring were continued during 30 min to ensure the precursors reduction. During this time, the color of the solution quickly changed from colorless to yellow, and gradually into dark orange.

Silica beads coating with polyelectrolytes

The well know layer-by-layer (LbL)[21] technique was used to coat the SiO_2 beads with 3 alternating layers of PEI, PAA and PEI providing a positive net charge on the particle surface. To achieve this, 0.5 mL of a SiO_2 beads solution (50 mg/mL) were added drop-wise, meanwhile stirring, to 25 mL of a PEI aqueous solution (2 mg/mL) previously sonicated during 30 min. The mixture was vigorously stirred for

[21] Decher, G. *Science* **1997**, *277*, 1232.

2 h and then centrifuged twice (3190 rcf, 20 min) and redispersed with Milli-Q water to remove the polyelectrolyte excess. The same procedure was applied for the other 2 layers of poly (acrylic acid) (PAA) and PEI, using 2 mg/mL PAA, 6 mM NaCl, and 2 mg/mL PEI solutions. Cyclic repetition of both adsorption steps (+ and - polymers) leads to the formation of multilayer structures with higher charge density, while a single deposition cycle only generates a submonolayer coverage.[21] Finally, the SiO_2 beads were redispersed in 10 mL of Milli-Q water to achieve a final concentration of 2.5 mg/mL.

Silver nanoparticles assembly onto silica beads

AgNPs were cleaned by centrifugation (2770 rcf, 20 min) and redispersed in Milli-Q water, to a final $[Ag^0] = 2.3\times10^{-4}$ M. This washing cycle allows to remove the excess of citrate that partially hinders the adhesion of AgNPs on silica beads, while preserving the overall colloidal stability. The polyelectrolyte wrapped silica beads were coated with AgNPs by adding drop by drop, under sonication, 800 µL of the silica beads solution into a flask containing a AgNPs solution (133 mL, $[Ag^0]$ = 0.23 mM). Then, the mixture was vortexed for 30 s and left sedimenting overnight. After that, the sample was centrifuged 3 times (95 rcf, 5 min) and redispersed in 2 mL of Milli-Q water to achieve a final SiO_2 beads concentration of 1 mg/mL.

MB-H1 conjugation to SiO_2@Ag beads

5 mL of MB-H1 solutions (200, 20, 2 nM, 200, 20, and 2 pM, respectively) in 10 mM Tris·HCl pH 7.5, 100 mM NaCl, were added over 5 mL aliquots of a 20 µg/mL SiO_2@Ag beads solution in 10 mM Tris·HCl, pH 7.5, 100 mM NaCl, and the resulting mixtures were incubated overnight at room temperature. The following morning,

the final SiO_2@Ag bead concentration of the solutions (ca. 2.4×10^4 beads/mL) was calculated with a hemocytometer.

Samples for SERS characterization

Silver nanoparticles (20 µL 10^{-6} M in silver) were spin coated on glass slide at low particle concentration. Also, they were aggregated into a film by casting a drop of a concentrated solution (10 µL 10^{-3} M in silver) and air-dried.

MCF-7 cell line culture

MCF-7 cancer cell line was used as a positive c-MYC expression control. MCF-7 cells were maintained in EMEM media supplemented with 10% fetal bovine serum and 0.1% human insulin and incubated at 37 °C, 5% CO_2 in a humidified atmosphere.

Human samples

Samples were provided by a patient with stage IV ovarian adenocarcinoma, in progression at the time of the sample collection. The presence of a tumor was confirmed histologically in compliance with common standards.

Peripheral blood mononuclear cells extraction

Blood samples were obtained from and healthy donors and processed within the following 24h. 8 mL of blood from each donor were diluted 1:2 with Hank's balanced salt solution (HBSS) and disposed carefully onto a 15 mL layer of Ficoll-Paque Plus (from Ge Healthcare LifeSciences). Samples were centrifuged for 40 min at 400 g to separate blood content. Peripheral blood mononuclear cells (PBMCs) were collected and washed with 1x PBS and finally, cultured in RPMI media supplemented with 10% fetal bovine serum at 37 °C, 5% CO_2 in a humidified atmosphere.

Protein extraction

PBMCs and MCF-7 cells were similarly counted and harvested from flask using trypsin 0.25% EDTA, and centrifuged at 170 g for 5 min. Cell pellets were suspended in 0.2 mL of lysis buffer, containing 50 mM HEPES, 0.5 M NaCl, 1.5 mM $MgCl_2$, 1 mM EDTA, 10% v/v glycerol, 1% Triton X-100, and 0.01 mL of protease inhibitor cocktail (from Sigma-Aldrich). Lysis step was carried out for 1h at 4 °C, spinning tubes every 15 min to disrupt cell membranes. Lysates were centrifuged at 13,000 g for 10 min at 4 °C and protein containing supernatants were kept at −80 °C until use.

Total protein and c-MYC levels quantification

Protein concentration of lysates were quantified with Bradford protein assay; human c-MYC oncoprotein levels were determined with a total-human c-MYC enzyme-linked immunoabsorbed assay (ELISA) kit (from LifeSciences). Samples were

diluted 1/10 – 1/100 and incubated for 3h with a primary anti-c-MYC antibody, followed by 30 min incubation with a secondary HRP labeled antibody. HRP substrate was added for 30 min, and absorbance was measured with a Multimode Plate Reader Tristar 2S. All standards and lysates were assayed in triplicate and protein concentrations were extrapolated from calibration curves.

SERS characterization of the MB-H1 functionalized beads and quantification of c-MYC

An aliquot of each suspension of SiO_2@Ag@MB-H1 was cast on a glass slide. Before drying, beads were first localized with a ×5 objective and, later, investigated by SERS using a ×50 objective to focus 2.5 mW of 785 nm laser line for 1s. For each bead, 10 measurements were collected. For each sample, 10 beads were measured. Notably, time was incremented to 10 s in the samples with 10 and 1 pM MB-H1 concentration. The same protocol was repeated also for a bead concentration of ca. 240 beads/mL. We also attempted to perform the identical study for 24 beads/mL but due to the difficulty of locating the beads (and their low amount for statistical purpose) we could not use these diluted samples for detection.

SERS quantification of c-MYC was performed as follows. First, a calibration curve was generated using the same standards than for ELISA. Briefly, 100 µL of a 2400 beads/mL suspension of SiO_2@Ag@MB-H1, diluted 1/10 in 10 mM Tris·HCl pH 7.5, 100 mM NaCl from a 24000 beads/mL-100 pM MB-H1 solution (corresponding to ca. 2.5×10^6 molecules of MB-H1 per bead), was added per mL of sample, reaching a final bead concentration of ~218 beads/mL. After waiting for 1h to ensure the interaction between H1 and c-MYC, aliquots of 100 µL of sample ere cast onto a glass slide. Then, before drying, beads were first localized with a ×5 objective and

then mapped with the Raman microscope using a ×50 objective and 785 nm laser line. For statistical purpose, 10 spectra of 10 seconds were recorded for each bead (with a power laser at the sample of 2.5 mW). For each sample, between 10 and 15 beads were measured. Each experiment was replicated three times. The same protocol was followed for human samples.

CHAPTER 5

UNIVERSITAT ROVIRA I VIRGILI
NANO/MICROSYSTEMS FOR CANCER DIAGNOSIS AND THERAPY
Manuel García Algar

Breast cancer therapy through membrane receptor targeting

Porous silicon particles (PSiPs) have been used extensively as drug delivery systems, loaded with chemical species for disease treatment. It is well known from silicon producers that silicon is characterized by a low reduction potential, which in the case of PSiPs promotes explosive oxidation reactions with energy yields exceeding that of trinitrotoluene (TNT). The functionalization of the silica layer with sugars prevents its solubilization, while further functionalization with an appropriate antibody enables increased bioaccumulation inside selected cells. We present here an immunotherapy approach for potential cancer treatment. Our platform comprises the use of engineered silicon particles conjugated with a selective antibody. The conceptual advantage of our system is that after reaction, the particles are degraded into soluble and excretable biocomponents. In our study, we demonstrate in particular, specific targeting and destruction of cancer cells *in vitro*. The fact that the LD50 value of PSiPs-HER-2 for tumor cells was 15-fold lower than the LD50 value for control cells demonstrates very high *in vitro* specificity. This is the first important step on a long road towards the design and development of novel chemotherapeutic agents against cancer in general, and breast cancer in particular.

1 Introduction

Cancer is the second cause of death worldwide. In the case of breast cancer, epidemiological studies point to more than one million new cases diagnosed per year and an annual mortality rate close to 450,000 deaths. Particles have shown great potential[1] for drug delivery[1,2,3] and cancer treatment.[4,5,6,7] In most approaches, particles are directed to target cells by antibodies attached to their surfaces, which in the case of in vivo administration, supplements passive targeting through the EPR (enhanced permeability and retention) effect[8]. Some strategies involve heating particles with an external oscillating magnetic or electromagnetic field and causing apoptosis of the nearby cells through magnetothermia[9,10] or photothermia.[5,11-14] These materials suffer certain limitations, such as the large and expensive facilities (i.e. magnetic resonance imaging, MRI) necessary for magnetothermia, and the limited penetration depth of light in the body in the case of photothermia. Other approaches make use of antibody functionalized particles loaded with cancer drugs to deliver the drug to tumor cells.[4,15-18] Porous silicon particles (PSiPs) have been considered a very promising platform for cancer therapy because of their excellent biocompatibility[19] and biodegradability.[4,20-22] In all studies reported to date, PSiPs work either as a passive carrier of an anticancer cargo[4,15-18] or as an element

[1] Prasad, P. N. *Introduction to Nanomedicine and Nanobioengineering*; Wiley: New York, **2012**.
[2] Randall, C. L.; Leong, T. G.; Bassik, N.; Gracias, D. H. *Adv. Drug Del. Rev.* **2007**, *59*, 1547.
[3] Reibetanz, U.; Chen, M. H. A.; Mutukumaraswamy, S.; Liaw, Z. Y.; Oh, B. H. L.; Venkatraman, S.; Donath, E.; Neu, B. r. *Biomacromol.* **2010**, *11*, 1779.
[4] Park, J.-H.; Gu, L.; von Maltzahn, G.; Ruoslahti, E.; Bhatia, S. N.; Sailor, M. J. *Nat. Mater.* **2009**, *8*, 331.
[5] Hong, C.; Lee, J.; Son, M.; Hong, S. S.; Lee, C. *Anti-Cancer Drugs* **2011**, *22*, 971.
[6] Canham, L. T. In *UK Patent Nr. 0302283.7*; 0302283.7, U. P. N., Ed. UK, 2003; Vol. UK Patent Nr. 0302283.7.
[7] Xiao, L.; Gu, L.; Howell, S. B.; Sailor, M. J. *ACS Nano* **2011**, *5*, 3651.
[8] Gil, P. R.; Parak, W. J. *ACS Nano* **2008**, *2*, 2200.
[9] Gomella, L. G. *Nat. Clin. Pract. Urol.* 2004, *1*, 72.
[10] Maier-Hauff, K.; Ulrich, F.; Nestler, D.; Niehoff, H.; Wust, P.; Thiesen, B.; Orawa, H.; Budach, V.; Jordan, A. *J. Neuro-Oncol.* **2011**, *103*, 317.
[11] Lal, S.; Clare, S. E.; Halas, N. J. *Acc. Chem. Res.* **2008**, *41*, 1842.

activated by an appropriate trigger, namely light and acoustic waves for particle thermalization[13,23,24] or singlet oxygen generation in photodynamic therapies.[7]

In this chapter, it is demonstrated that PSiPs themselves can be used as a drug for cancer treatment and shown how to modulate their activity by taking advantage of their surface functionalization and the enzymatic machinery of eukaryotic cells.

Silicon is characterized by a reduction potential[25] of -1.697 eV to yield silicates or -0.91 eV to yield silica, which is ultimately dissolved as silicates in the presence of water. The low reduction potential makes reactions violent and even explosive[26] in nanoscaled porous particles.[27] On the other hand, the high tendency of silicon to undergo oxidation is modulated by the spontaneous generation of a passivation layer of SiOx when exposed to open atmosphere. Notably, this passivation layer dissolves in water and particularly in slightly acidic media. The kinetics of the dissolution of this layer can be modulated by surface functionalization of the silica. Thus, by coating with a compact monolayer of an organic molecule, dissolution can be retarded or even prevented.

The processes for obtaining PSiPs have been well known for 20 years.[28] They are mainly based on wet chemistry methods, where the starting material, bulk silicon, is converted into porous silicon, bya an electrochemical or stain-etching reaction,

---

[12] Lee, C.; Kim, H.; Hong, C.; Kim, M.; Hong, S. S.; Lee, D. H.; Lee, W. I. *J. Mater. Chem.* **2008**, *18*, 4790.
[13] Osminkina, L. A.; Gongalsky, M. B.; Motuzuk, A. V.; Timoshenko, V. Y.; Kudryavtsev, A. A. *Appl. Phys. B* **2011**, *105*, 665.
[14] Jain, P. K.; Huang, X.; El-Sayed, I. H.; El-Sayed, M. A. *Acc. Chem. Res.* **2008**, *41*, 1578.
[15] Serda, R. E.; Godin, B.; Blanco, E.; Chiappini, C.; Ferrari, M. *Biochim Biophys Acta* 2011, *1810*, 317.
[16] Xu, R.; Huang, Y.; Mai, J.; Zhang, G.; Guo, X.; Xia, X.; Koay, E. J.; Qin, G.; Erm, D. R.; Li, Q.; Liu, X.; Ferrari, M.; Shen, H. *Small* **2013**, *9*, 1799**.**
[17] Park, J. S.; Kinsella, J. M.; Jandial, D. D.; Howell, S. B.; Sailor, M. J. *Small* 2011, *7*, 2061.
[18] Xue, M.; Zhong, X.; Shaposhnik, Z.; Qu, Y.; Tamanoi, F.; Duan, X.; Zink, J. I. *J. Am. Chem. Soc.* **2011**, *133*, 8798.
[19] Canham, L. T. *Adv. Mater.* **1995**, *7*, 1033.
[20] Popplewell, J. F.; King, S. J.; Day, J. P.; Ackrill, P.; Fifield, L. K.; Cresswell, R. G.; Di Tada, M. L.; Liu, K. *J. Inorganic Biochem.* **1998**, *69*, 177.
[21] Shabir, Q.; Pokale, A.; Loni, A.; Johnson, D. R.; Canham, L. T.; Fenollosa, R.; Tymczenko, M.; Rodríguez, I.; Meseguer, F.; Cros, A.; Cantarero, A. *Silicon* **2011**, *3*, 173.

followed by a process such as ultrasonication, to break the porous layer into small particles.[29,30] Other, less studied methods, use a bottom-up approach based on chemical vapor deposition techniques, where the starting material is a precursor gas, namely silane or di-silane, which can be decomposed at higher temperatures.[25] Under controlled conditions of pressure, temperature and time, such gases nucleate and nanometric porous silicon nanoparticles can be obtained.[31] This is a complex process, and the involved mechanisms are still under study.[32,33] In some manner PSiPs can be regarded as a macromolecule resulting from the polymerization of disilane with a dramatic capability of oxidation. In this chapter will be demonstrated that silicon particles coated with a native silica layer can be engineered with the bioorganic appropriate ligands to target and accumulate into tumour cells. Once inside the cell, the particles are driven to the lysosome were the enzymatic machinery of the cell metabolize the ligands. Then, the exposition of the soluble silica coating to the aqueous lysosomal solution degrades this layer allowing water to react violently with the silicon. As result the target cells dye while the particles are degraded into soluble and excretable biocomponents.

2 Results and Discussion

Targeting strategy

PSiPs used in this work were fully developed by our collaborators, Prof. Francisco Messeguer (Centro de Tecnologías Físicas, CSIC-Universidad Politécnica de Valencia, Spain) and Prof. Wolfgang J Parak (Fachbereich Physik, Phillips-Märburg Universität, Germany).[34] The nanostructured particles were highly spherical with a diameter between 1.5– 2 μm, with an intrinsic photoluminescence in between the dark red and the near infrared (**Fig. 5.1A and B**).[35] As prepared, and after extracting the materials from the reactor, exposure to atmospheric oxygen generated a thin layer of silicon oxide. This coating acted as a protective shell and generated an easily functionalizable surface to couple an organic layer would protect silica from dissolution in physiological media. The enzymatic machinery present in the cell can easily degrade this protective organic shell, which would consequently trigger oxidation reactions of the particles after their internalization by cells. To prove this concept, we used a glucopyranoside derivative that can be easily metabolized by the lysosomal enzyme α-D-glucoside glucohydrolase. The lysosome has been shown to be a target organelle for most nano- and microparticles[36,37] and thus it can be

[22] Chen Y.; Wan Y.; Wang Y.; Zhang H.; Jiao Z. *Int. J. Nanomed.*, 2321.
[23] Mackowiak, S. A.; Schmidt, A.; Weiss, V.; Argyo, C.; von Schirnding, C.; Bein, T.; Bräuchle, C. *Nano Lett.* **2013**, *13*, 2576.
[24] Li, Z.; Barnes, J. C.; Bosoy, A.; Stoddart, J. F.; Zink, J. I. *Chem. Soc. Rev.* **2012**, *41*, 2590.
[25] O´Mara, W. C.; Herring, B.; Hunt, P. *Handbook of Semiconductor Silicon Technology*, Noyes Publication: New Jersey, **1990**.
[26] Mikulec, F. V.; Kirtland, J. D.; Sailor, M. J. *Adv. Mater.* **2002**, *14*, 38.
[27] Clement, D.; Diener, J.; Gross, E.; Kunzner, N.; Timoshenko, V. Y.; Kovalev, D. *Phys. Stat. Sol. A* 2005, *202*, 1357.
[28] Canham , L. T. *Appl. Phys. Lett.* **1990**, *57*, 1046.
[29] Canham, L. T. *Properties of Porous Silicon*; INSPEC: United Kindom, 1997.
[30] Heinrich, J. L.; Curtis, C. L.; Credo, G. M.; Sailor, M. J.; Kavanagh, K. L. *Science* **1992**, *255*, 66.

predicted that after internalization by cells, the particles would be exposed to α-D-glucoside glucohydrolase.

The sugar and the particle cannot be directly linked without previous modifications. Thus, PSiPs were capped with aminopropylsilane (APS),[38] while the glucopyranoside selected was 2-acetamido-2-deoxy-β-D-glucopyranosyl-oxyacetic acid. The benzotriazol-1-yloxytris(dimethylamino)phosphonium-hexafluoro-phosphate/anhydrous 1-hydroxybenzotriazole (BOP/HOBt) coupling method was chosen to generate a peptide bond between the amine-functionalized particle surface and the carboxylic acid group attached to the carbohydrate. Notably, within this configuration, hybrid particles will resist oxidation in physiological media but should be degraded unselectively within any cell, following endocytosis and subsequent localization within the lysosome. Therefore, for anticancer therapy, a selective antibody that targets the surface receptor of the desired cells is necessary.

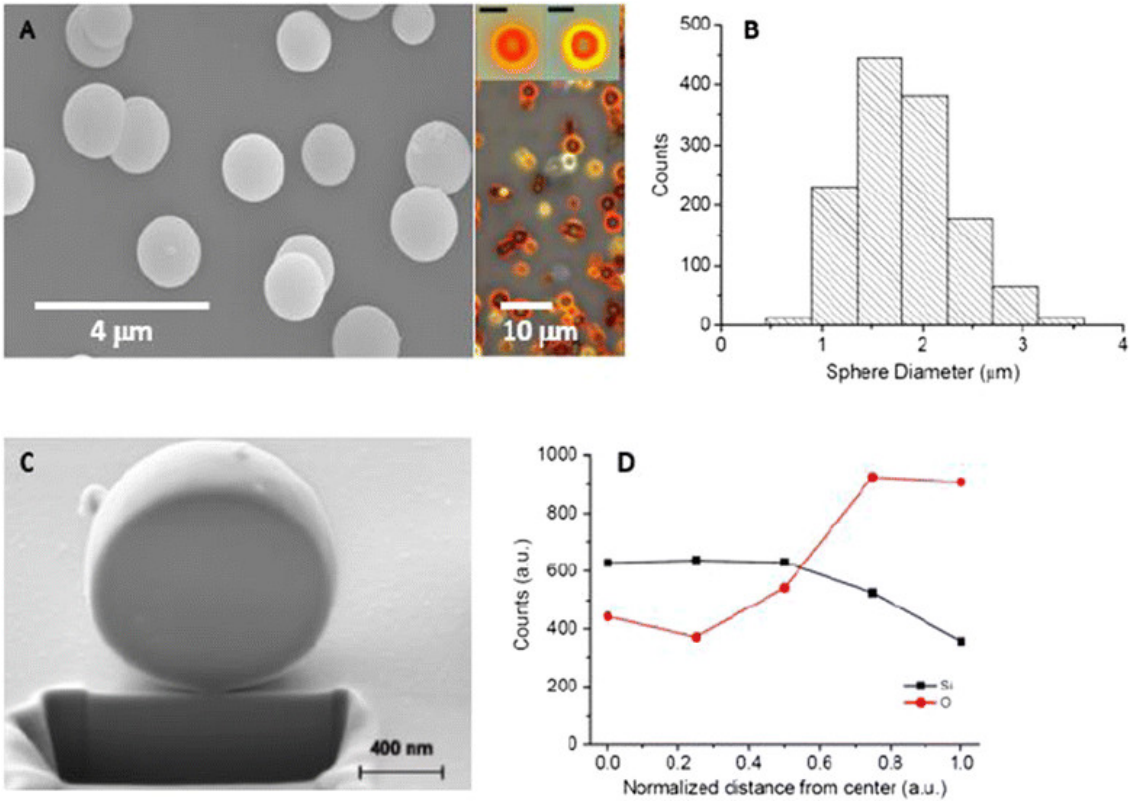

FIGURE 5.1 (A) SEM and optical microscopy images of the porous silicon particles as prepared and (B) their size distribution. All scale bars in the insets correspond to 2 µm. (C) SEM image of a porous silicon colloid carved using the focused ion beam (FIB) technique. (D) EDX analysis of materials inside

a silicon colloid as a function of the distance from the sphere center, normalized to the sphere radius (d=distance from the sphere center/sphere radius). The graph shows the counts for the Si and O peaks of the EDX spectra at five different points of analysis. The points were selected along a line travelling from the nucleus (d=0) to the sphere surface (d=1).

Consequently, the third step in the preparation of our immunotherapeutic material involved the coupling of a directing vector. HER2 positive breast cancer is characterized by the amplification of this gene and high expression and activity of its protein.[39] In fact, there is a strong association between HER2 tyrosine-kinase expression and the aggressiveness and prognosis of the disease.

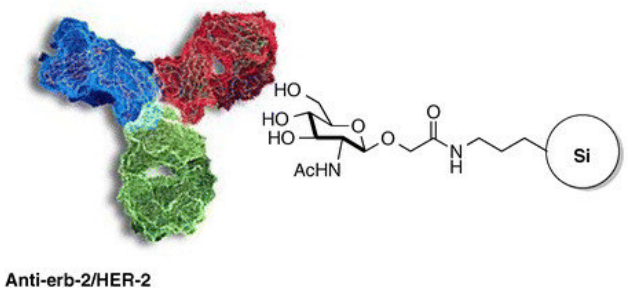

FIGURE 5.2 Schematic representation of the glucopyranose derivative and the antibody HER2 coupled to the silicon particles.

Fortunately, HER2 amplification confers a selective target for specific sensing strategies, such as discussed in previous chapters, and treatment with several drugs targeting this receptor which are actually used for breast cancer treatment in

[31] Littau, K. A.; Szajowski, P. J.; Muller, A. J.; Kortan, A. R.; Brus, L. E. *J. Phys. Chem.* 1993, *97*, 1224.
[32] Menz, W. J.; Shekar, S.; Brownbridge, G. P. E.; Mosbach, S.; Körmer, R.; Peukert, W.; Kraft, M. *J. Aerosol Sci.* 2012, *44*, 46.
[33] Swihart, M. T.; Girshick, S. L. *J. Phys. Chem. B* 1998, *103*, 64.
[34] Fenollosa, R.; Ramiro-Manzano, F.; Tymczenko, M.; Meseguer, F. *J. Mater. Chem.* 2010, *20*, 5210.
[35] Ramiro-Manzano, F.; Fenollosa, R.; Xifré-Pérez, E.; Garín, M.; Meseguer, F. *Advanced Materials* 2011, *23*, 3022
[36] Kastl, L.; Sasse, D.; Wulf, V.; Hartmann, R.; Mircheski, J.; Ranke, C.; Carregal-Romero, S.; Martínez-López, J. A.; Fernández-Chacón, R.; Parak, W. J.; Elsasser, H.-P.; Rivera_Gil, P. *ACS Nano* 2013, *7*, 6605.
[37] Schweiger, C.; Hartmann, R.; Zhang, F.; Parak, W.; Kissel, T.; Rivera_Gil, P. *J. Nanobiotech.* 2012, *10*, 28.
[38] Sanles-Sobrido, M.; Exner, W.; Rodríguez-Lorenzo, L.; Rodríguez-González, B.; Correa-Duarte, M. A.; Álvarez-Puebla, R. A.; Liz-Marzán, L. M. *J. Am. Chem. Soc.* 2009, *131*, 2699.
[39] Slamon, D.; Eiermann, W.; Robert, N.; Pienkowski, T.; Martin, M.; Press, M.; Mackey, J.; Glaspy, J.; Chan, A.; Pawlicki, M.; Pinter, T.; Valero, V.; Liu, M.-C.; Sauter, G.; von Minckwitz, G.; Visco, F.; Bee, V.; Buyse, M.; Bendahmane, B.; Tabah-Fisch, I.; Lindsay, M.-A.; Riva, A.; Crown, J. *New England Journal of Medicine* 2011, *365*, 1273.

medical practice, including small molecule tyrosine kinase inhibitors (TKIs) such as gefitinib, erlotinib or lapatinib or monoclonal antibodies such as trastuzumab, pertuzumab or cetuximab.[40] The HER2 antibody was linked to the particles by taking advantage of its affinity for the sugar (**Fig. 5.2**). Thus, one of the four glycosylation immunogenic regions was spontaneously coupled to the sugars present on the particle surface, allowing the other three to interact with the cell membrane receptors.[41,42]

Performance of the treatment and cancer cells elimination

To test the interaction of our particles with the cells, the PSiP-HER2 were internalized by the HER2 positive cancer cell line, SK-BR-3. As shown in **Fig. 5.3A**, the particles could be visualized, surrounded by the cell membrane. Some particles remained in the extracellular space, while other particles were seen attached to the cell membrane. Despite their micro-size and the degree of agglomeration, the particles could be internalized by SK-BR-3 cells without affecting their viability at an early stage. This is in agreement with other work[37] showing that particles at the micro-scale can be safely incorporated by eukaryotic cells.

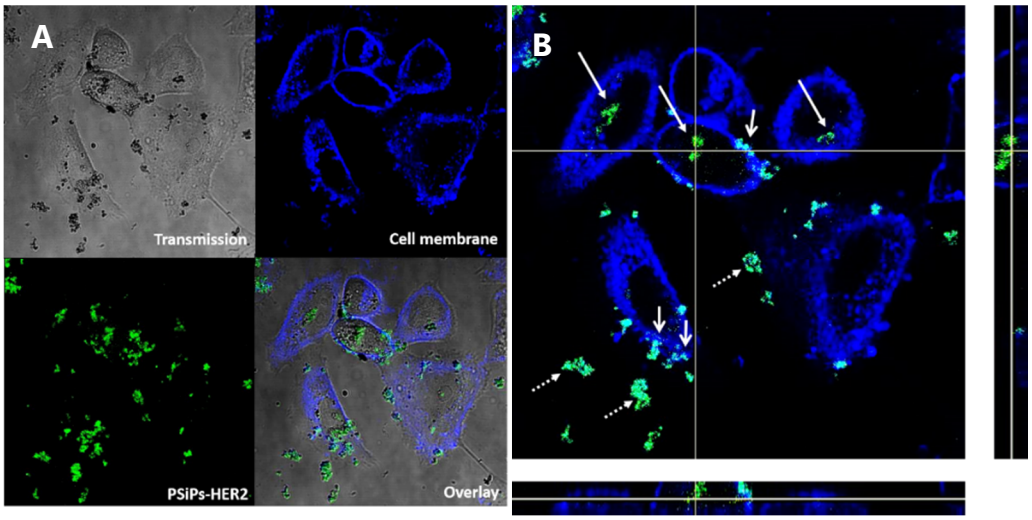

FIGURE 5.3 Particle localization into SK-BR-3 cell line. SK-BR-3 (cell membrane labeled in blue) treated with PSiP-HER2 particles (presented in green) for 24h, showing the particle inside (arrow) and, outside (dashed arrow) the cells and at the cell membrane (opened arrow). (A) Orthogonal view in the 3 planes (X/Y, X/Z and Y/Z) of the particles pointed at the intersection of the X and Y axis. As seen from all planes, the particles are surrounded by the cell membrane. (B) Confocal images of the cells in the transmission channel, the cell membrane and PSiP-HER2 fluorescent channels, and overlay of all channels. PSiPs-HER2 were labeled with DyLight 488.

Next, we tested the efficiency of the PSiPs functionalized with antibodies against HER2 receptors (PSiPs-HER2) for their potential to selectively kill only a cell lines overexpressing the HER2 receptor (SK-BR-3) by comparing to one with normal expression levels (MDA-MB-435).[43] The cells were seeded in 96-well plates and incubated with different quantities of PSiPs-HER2 for 48 h, before a resazurin-based viability assay was performed. Notably, when SK-BR-3 (cells overexpressing the HER2 receptors) were treated with PSiPs-HER2, their viability was clearly compromised (**Fig. 5.4**, black points). On the other hand, SK-BR-3 cells treated with PSiPs (**Fig. 5.4**, blue points) or MDA-MB-435 cells treated with PSiPs or PSiPs-HER2 (**Fig. 5.4**, red and green points, respectively) showed a more delayed toxicological

[40] Agus, D. B.; Gordon, M. S.; Taylor, C.; Natale, R. B.; Karlan, B.; Mendelson, D. S.; Press, M. F.; Allison, D. E.; Sliwkowski, M. X.; Lieberman, G.; Kelsey, S. M.; Fyfe, G. *Journal of Clinical Oncology* **2005**, *23*, 2534.
[41] Colombo, M.; Mazzucchelli, S.; Montenegro, J. M.; Galbiati, E.; Corsi, F.; Parak, W. J.; Prosperi, D. *Small* **2012**, *8*, 1492.
[42] Franklin, M. C.; Carey, K. D.; Vajdos, F. F.; Leahy, D. J.; de Vos, A. M.; Sliwkowski, M. X. *Cancer Cell* **2004**, *5*, 317.
[43] Paris;, L.; Cecchetti;, S.; Spadaro;, F.; Abalsamo;, L.; Lugini;, L.; Pisanu;, M. E.; Lorio;, E.; Natali;, P. G.; Ramoni;, C.; Podo;, F. *Breast Cancer Res.* **2010**, *12*, R27.

response. The L_{50} (lethal dose killing 50% of the cell population) values are presented in **Table 5.1**. Only around 250 µg/mL PSiPs-HER2 were needed to kill 50% of the SK-BR-3 cells, whereas much higher quantities of the same particles were required under the same conditions to kill the same proportion of MDA-MB-435 cells. On the other hand, PSiPs without attached HER2 antibodies showed a much lower toxicological response, as their L_{50} values were very high for both cell types. These results confirm the efficacy of PSiPs-HER2 to recognize the HER2 receptors present on the surface of SK-BR-3 cells to a higher extent than that on MDA-MB-435 cells and to effectively promote their local accumulation. The degree of targeting was more than sufficient to accelerate the death of the targeted cancer cells.

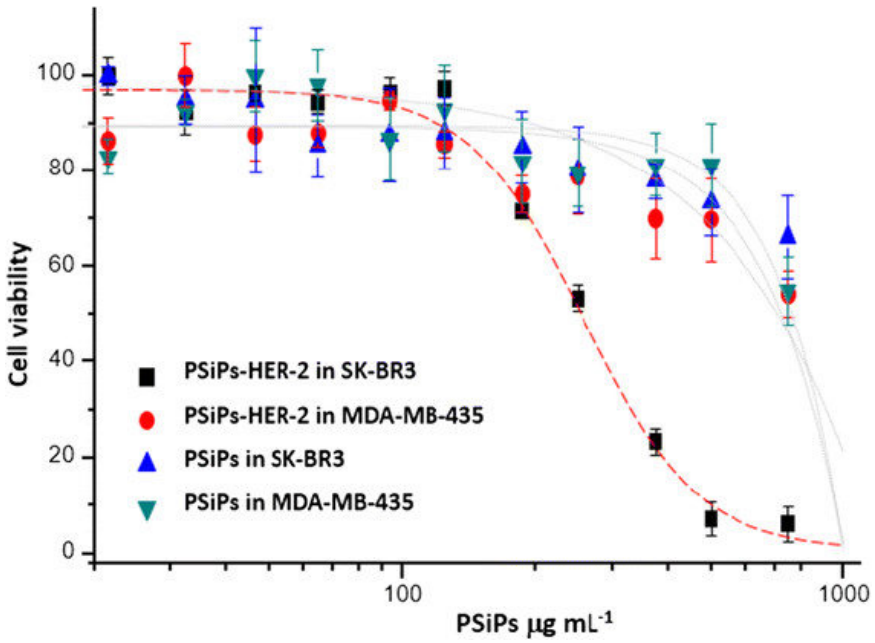

FIGURE 5.4 Relative cell viability after incubation of SK-BR-3 and MDA-MB-435 cells with PSiPs-HER2 for 48h.

TABLE 5.1 Calculated LD_{50} obtained from the dose-response curves shown in Fig. 5.4.

Cell line	Type of NP	LD_{50} (μg/mL)	LD_{50} SD
SK-BR-3	PSiPs-HER2	249	10
MDA-MB-435	PSiPs-HER2	3776	180
SK-BR-3	PSiPs	5603	360
MDA-MB-435	PSiPs	2672	214

3 Conclusions

In summary, here it is presented an immunotherapy approach for potential cancer treatment. Proposed platform comprises the use of engineered silicon particles conjugated with a selective antibody. The conceptual advantage of our system is that after reaction, the particles are degraded into soluble and excretable biocomponents. In this study, it is demonstrated in particular, specific targeting and destruction of cancer cells *in vitro*. The fact that the L_{50} value of PSiPs-HER2 for tumor cells was 15-fold lower than the L_{50} value for control cells demonstrates very high *in vitro* specificity. This is the first important step on a long road towards the design and development of novel chemotherapeutic agent against cancer in general, and breast cancer in particular.

4 Experimental section

Synthesis of porous silicon microspheres

Our method for producing porous silicon microspheres is based on the decomposition of disilane gas (Si_2H_6) by chemical vapor deposition (CVD). This is similar to the synthesis of silicon colloids,[44] where the gas is introduced in a reactor whose walls are heated at high temperatures for a certain time, usually higher than 400 °C. During this procedure, Si_nH_m clusters grow in the gas phase[45] and these become highly spherical, micrometer-sized particles, through surface tension forces. At the same time, the process of hydrogen desorption from the clusters progressively reduces the hydrogen content until they become hydrogenated amorphous silicon (a:Si-H) colloids. To obtain porous silicon microspheres, the heating process is stopped at an early stage, before the formation of amorphous silicon colloids is complete. In this way, porous particles with an undetermined composition of silicon and hydrogen atoms are obtained.

Porous silicon particles for this work were synthesized using a di-silane decomposition temperature of 400 °C. The absolute gas pressure in the reactor was about 0.25 atm at room temperature and we used decomposition times from 1 to 2 minutes, measured from the stage where the gas reaches the target temperature.

Silicon and oxygen content of porous silicon colloids were analyzed by electron dispersive X-ray (EDX) measurements. For this purpose, colloids were carved using a focus ion beam (FIB) technique (FEI Helios NanoLab Omniprobe). Figure 1C shows a scanning electron microscope (SEM) image of a carved colloid, 1.2 μm in diameter. The carved surface appears to be flat because the ion gun of the FIB removes

[44] Fenollosa, R.; Meseguer, F.; Tymczenko, M. *Advanced Materials* **2008**, *20*, 95.
[45] Jasinski, J. M.; Gates, S. M. *Accounts of Chemical Research* **1991**, *24*, 9.

material and deposits it at the same time on the surface of the particle, thus hiding porous structures. Nevertheless, because the EDX interaction volume penetrates the region where pores are less modified by the FIB carving action, one can extract useful information about the cavity structure. Figure 1D shows the EDX analysis corresponding to silicon and oxygen in different regions of the particle, from the cavity center to the cavity surface. This shows two key results: a) the oxygen content appears to be completely within the cavity and b) the oxygen (silicon) concentration increases (decreases) from the center to the surface. This result supports the hypothesis that porous silicon colloids possess a gradient, or onion-like, porous structure, as images taken by optical microscopy suggest. In addition, it indicates that porosity is higher at the surface of the colloid than within it.

Synthesis of the 2-acetamido-2-deoxy-β-d-gluco-pyrano-syloxyacetic acid

Solvents were dried according to published methods and distilled before use. All other reagents were commercial compounds of the highest purity available. Unless otherwise indicated, all reactions involving air- and moisture-sensitive materials were carried out under an argon atmosphere, while those not involving aqueous reagents were carried out in oven-dried glassware. Analytical thin layer chromatography (TLC) was performed on aluminum plates with Merck Kieselgel 60F254 and visualized by UV irradiation (254 nm) or by staining with an ethanolic solution of phosphomolybdic acid. Flash column chromatography was carried out using Merck Kieselgel 60 (230-400 mesh) under pressure. ^{1}H NMR spectra were recorded in $CDCl_3$ and D_2O, at ambient temperature on an AMX-400 spectrometer at 400 MHz, with residual protic solvent as the internal reference [$CDCl_3$, δ_H = 7.26 ppm]; chemical shifts (δ) are given in parts per million, and coupling constants (*J*) are

given in Hertz. The proton spectra are reported as follows: δ (multiplicity, coupling constant *J*, number of protons, assignment).

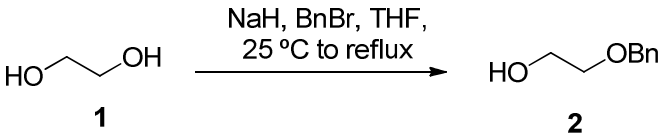

1 **2**

2-(Benzyloxy)ethanol 2. To a mixture of NaH (3.4 g, 0.085 mol, 60% w/w in mineral oil) in tetrahydrofuran (THF, 150 mL), ethylene glycol 1 (25.1 mL, 0.45 mol) was added and the mixture was stirred for 1 h at 25 °C. Then, benzyl bromide (8.9 g, 0.075 mol) was added and the reaction was refluxed for 12 h. After cooling the mixture (0 °C), a saturated aqueous solution of NH_4Cl was added, the solvent was evaporated and the mixture was extracted with EtOAc (3x). The combined organic layers were washed with a saturated aqueous solution of NH_4Cl and brine, and dried (Na_2SO_4). The solvent was evaporated to afford 11.22 g (98% yield) of a colorless oil identified as 2-(benzyloxy)ethanol 2. The spectroscopic data were identical to those described in the literature.[46] ^{1}H-NMR (400 MHz, $CDCl_3$): δ 7.40-7.30 (m, 5H), 4.58 (s, 2H), 3.78 (t, *J*= 5.0 Hz, 2H), 3.61 (t, *J*= 4.9 Hz, 2H), 2.06 (br, 1H, OH) ppm.

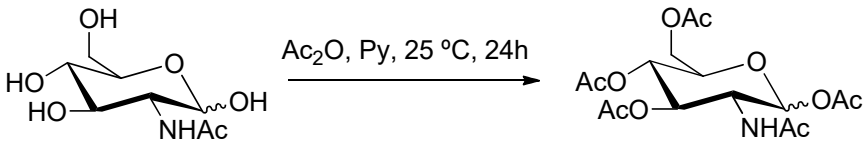

3 **4**

1,3,4,6-tetra-*O*-acetyl-α/β-*N*-acetylglucosamine 4. *N*-acetyl-D-glucosamine 3 (5 g, 22.6 mmol) was dissolved in pyridine (36 mL) and acetic anhydride (25 mL) was added dropwise at 0 °C. The reaction mixture was stirred at 25 °C for 24 h, then

[46] Xiao, Q.; Liu, Y.; Qiu, Y.; Zhou, G.; Mao, C.; Li, Z.; Yao, Z.-J.; Jiang, S. *Journal of Medicinal Chemistry* **2010**, *54*, 525.

diluted with CH_2Cl_2 and washed consecutively with cold water, a saturated aqueous solution of $NaHCO_3$, and a 10% aqueous solution of $CuSO_4$. The organic layer was dried (Na_2SO_4) and the solvent was evaporated to obtain 6.60 g (75%) of a white solid identified as 1,3,4,6-tetra-*O*-acetyl-α/β-*N*-acetylglucosamine 4. The spectroscopic data were identical to those described in the literature.[47] ^{1}H-NMR (400 MHz, $CDCl_3$): δ 6.17 (d, *J*= 3.6 Hz, 1H), 5.64 (d, *J*= 9.3 Hz, 1H), 5.30-5.20 (m, 2H), 4.49 (ddd, *J*= 10.6, 8.9, 3.6 Hz, 1H), 4.25 (dd, *J*= 12.5, 4.1 Hz, 1H), 4.07 (dd, *J*= 12.5, 2.4 Hz, 1H), 4.00 (ddd, *J*= 9.6, 4.0, 2.3 Hz, 1H), 2.20 (s, 3H), 2.09 (s, 3H), 2.06 (s, 3H), 2.05 (s, 3H), 1.94 (s, 3H) ppm.

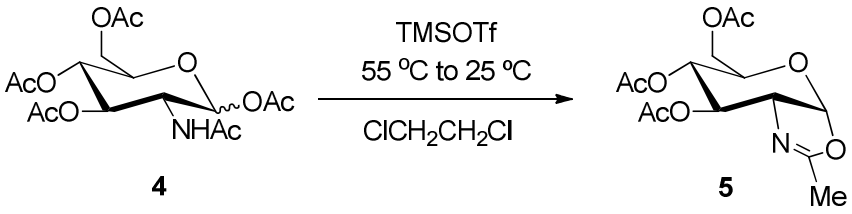

4 **5**

4′,5′-Dihydro-2′-methyloxazolo[5′,4′:1,2]-3,4,6-tri-*O*-acetyl-1,2-dideoxy-α-D-glucopyranoside 5. To a solution of 1,3,4,6-tetra-*O*-acetyl-α/β-*N*-acetylglucosamine 4 (2.49 g, 6.4 mmol) in dichloroethane (25 mL) TMSOTf (1.8 mL, 9.6 mmol) was added and the reaction was stirred for 2 h at 55 °C and for 12 h at 25 °C. A saturated aqueous solution of $NaHCO_3$ was added and the mixture was extracted with CH_2Cl_2 (3x). The combined organic layers were washed with a saturated aqueous solution of $NaHCO_3$ and dried (Na_2SO_4) and the solvent was evaporated. The resulting residue was purified by column chromatography (silicagel, 97:3 CH_2Cl_2/MeOH) to afford 1.86 g (78%) of 4′,5′-dihydro-2′-methyloxazolo[5′,4′:1,2]-3,4,6-tri-*O*-acetyl-1,2-dideoxy-α-D-glucopyranoside 5. The spectroscopic data were identical to those described in the literature.[48] ^{1}H-NMR (400 MHz, $CDCl_3$): δ 5.98 (d, *J*= 7.4 Hz, 1H),

[47] Allman, S. A.; Jensen, H. H.; Vijayakrishnan, B.; Garnett, J. A.; Leon, E.; Liu, Y.; Anthony, D. C.; Sibson, N. R.; Feizi, T.; Matthews, S.; Davis, B. G. *ChemBioChem* **2009**, *10*, 2522.
[48] Chambers, D. J.; Evans, G. R.; Fairbanks, A. J. *Tetrahedron* **2004**, *60*, 8411.

5.27 (t, *J*= 2.4 Hz, 1H), 4.94 (ddd, J= 9.2, 2.0, 1.2 Hz, 1H), 4.19-4.14 (m, 3H), 3.62 (dt, *J*= 8.8, 4.3 Hz, 1H), 2.12 Hz (s, 3H), 2.11 (s, 3H), 2.10 (s, 3H), 2.09 (s, 3H) ppm.

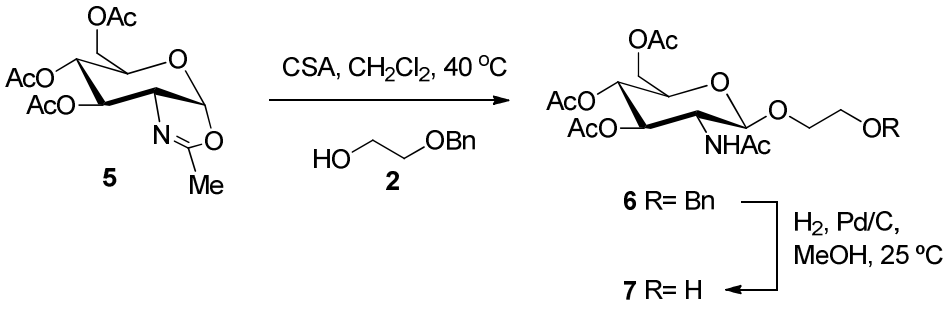

2-Hydroxyethyl-2-acetamido-3,4,6-tri-O-acetyl-2-deoxy-D-glucopyrano-side 7. 10-(*R*)-camphorsulfonic acid (1.40 g, 5.02 mmol) and 2-(benzyloxy)ethanol 2 (7.63 g, 50.2 mmol) were added to a stirred solution of 4′, 5′-dihydro-2′-methyloxazolo[5′,4′:1,2]-3,4,6-tri-*O*-acetyl-1,2-dideoxy-α-D-glucopyranoside 5 (1.86 g, 5.02 mmol) and powdered 4 Å molecular sieves (ca. 8 g) in CH_2Cl_2 (30 mL) and the reaction was stirred at 40 °C for 14 h. The mixture was cooled to 0 °C and a saturated aqueous solution of $NaHCO_3$ (60 mL) and CH_2Cl_2 (30 mL) was added. The layers were separated and the organic layer was washed with a saturated aqueous solution of $NaHCO_3$, brine and dried (Na_2SO_4), and the solvent then evaporated. The residue was purified by column chromatography (hexane/EtOAc 50:50 to CH_2Cl_2/MeOH 95:5) providing 2-*O*-benzyloxyethyl-2-acetamido-3,4,6-tri-O-acetyl-2-deoxy-β-D-glucopyranoside 6 as a colorless solid. The spectroscopic data of the product were identical to those described in the literature.[49] ^{1}H-NMR (400 MHz, $CDCl_3$): δ 7.4-7.3 (m, 5H), 5.50 (d, *J*= 8.8 Hz, 1H), 5.25 (dd, *J*= 10.4, 9.4 Hz, 1H), 5.09 (t, *J*= 9.6 Hz, 1H), 4.76 (d, *J*= 8.4 Hz, 1H), 4.56 (app s, 2H), 4.27 (dd, *J*= 12.3, 4.7 Hz, 1H), 4.20-4.15 (m, 2H), 3.99 (dt, *J*= 11.5, 3.9 Hz, 1H), 3.80 (ddd, *J*= 18.2, 14.7, 11.2 Hz, 1H), 3.70-3.65 (m, 3H), 2.09 (s, 3H), 2.06 (s, 3H), 2.03 (s, 3H), 1.87 (s, 3H) ppm.

[19] Tomabechi, Y.; Suzuki, R.; Haneda, K.; Inazu, T. *Bioorganic & Medicinal Chemistry* **2010**, *18*, 1259.

A mixture of 2-*O*-benzyloxyethyl-2-acetamido-3,4,6-tri-*O*-acetyl-2-deoxy-β-D-glucopyranoside 6 (0.19 g, 0.36 mmol) and Pd/C (10%, 0.02 g) in MeOH (3 mL) was stirred under an H_2 atmosphere for 7 h at 25 °C. The reaction was filtered through Celite and the solvent was evaporated to afford 0.15 g (96%) of a solid identified as 2-hydroxyethyl-2-acetamido-3,4,6-tri-*O*-acetyl-2-deoxy-β-D-glucopyranoside 7. The spectroscopic data of the product were identical to those described in the literature.[49] ^{1}H-NMR (400 MHz, $CDCl_3$): δ 5.58 (d, *J*= 9.0 Hz, 1H), 5.25 (dd, *J*= 10.6, 9.4 Hz, 1H), 5.07 (t, *J*= 9.6 Hz, 1H), 4.71 (d, *J*= 8.3 Hz, 1H), 4.2-4.10 (m, 2H), 3.9-3.8 (m, 2H), 3.7-3.6 (m, 2H), 2.58 (br, 1H, OH), 2.11 (s, 3H), 2.06 (s, 3H), 2.05 (s, 3H), 1.98 (s, 3H) ppm.

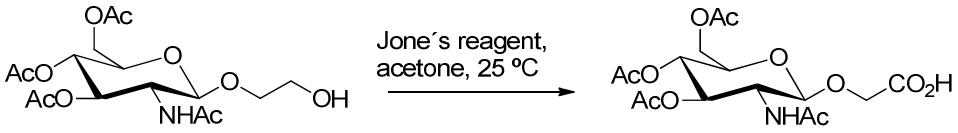

7 **8**

2-Acetamido-3,4,6-tri-*O*-acetyl-2-deoxy-β-D-glucopyranosyloxyacetic acid 8. Jones reagent (3.5 M, 0.2 mL, 0.69 mmol) was added to a stirred solution of 2-hydroxyethyl-2-acetamido-3,4,6-tri-*O*-acetyl-2-deoxy-α-D-glucopyranoside 7 (0.15 g, 0.35 mmol) in acetone (2 mL) at 0 °C and the reaction was stirred for 13 h at 25 °C. Isopropanol was added and the solvent was evaporated. After the addition of CH_2Cl_2 (10 mL) and brine (10 mL), the layers were separated, the organic layer was washed with brine and dried (Na_2SO_4), and the solvent was evaporated to afford 0.11 g (73%) of a white solid that was identified as 2-acetamido-3,4,6-tri-*O*-acetyl-2-deoxy-β-D-glucopyranosyloxyacetic acid 8 The spectroscopic data of the product were identical to those described in the literature.[49] ^{1}H-NMR (400 MHz, $CDCl_3$): δ 6.57 (br s, 1H), 5.22 (t, *J*= 9.6 Hz, 1H), 5.11 (t, *J*= 9.6 Hz, 1H), 4.75 (d, *J*= 8.1 Hz, 1H), 4.35 (app s, 2H), 4.28 (dd, *J*= 12.1, 4.9 Hz, 1H), 4.15 (dd, *J*= 10.7, 2.1 Hz, 1H), 4.1-4.0 (m, 1H), 3.7-3.6 (m, 1H), 2.11 (s, 3H), 2.06 (s, 3H), 2.03 (s, 3H), 1.97 (s, 3H) ppm.

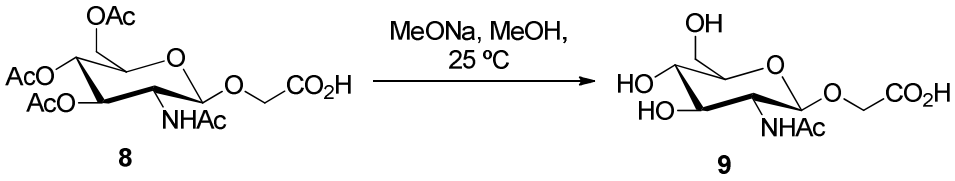

8 **9**

2-Acetamido-2-deoxy-β-D-glucopyranosyloxyacetic Acid 9. Sodium methoxide (0.02 g, 0.332 mmol) was added to a stirred solution of 2-acetamido-3,4,6-tri-*O*-acetyl-2-deoxy-β-D-glucopyranosyloxyacetic acid 8 (0.114 g, 0.255 mmol) in MeOH (6 mL) and the reaction mixture was stirred at 25 °C for 24 h. After the addition of Dowex-200 the mixture was filtered and the solvent was evaporated. The residue was dissolved in H_2O and dried under vacuum to afford 0.071 g (99%) of a solid identified as 2-acetamido-2-deoxy-β-D-glucopyranosyloxyacetic acid 9. The spectroscopic data of the product were identical to those described in the literature.[49] ^{1}H-NMR (400 MHz, D_2O): · · 4.49 (d, *J*= 8.4 Hz, 1H), 4.18 (s, 2H), 3.83 (d, *J*= 12.2 Hz, 1H), 3.70-3.60 (m, 2H), 3.50-3.40 (m, 1H), 3.40-3.30 (m, 2H), 1.97 (s, 3H) ppm.

Particle functionalization

A suspension of aminopropylsilane (APS)-coated silicon particles was produced by treatment of 0.1 g silica particles with APS (20 µL) in 2-propanol (5 mL) at 80 °C for 2 h. The particles were centrifuged at 3800 rpm for 30 min to remove the excess APS, followed by replacement of the supernatant solution by isopropanol. The particles were re-dispersed by shaking (ultrasound) for 10 min. This protocol was repeated two more times.[50]

[50] Pastoriza-Santos, I.; Gomez, D.; Perez-Juste, J.; Liz-Marzan, L. M.; Mulvaney, P. *Physical Chemistry Chemical Physics* 2004, *6*, 5056.

The particles were centrifuged at 3800 rpm for 30 min and the supernatant was replaced by dimethylformamine (DMF). Then, a solution of 2-acetamido-2-deoxy-β-D-glucopyranosyloxyacetic acid 9 (14 mg), benzotriazol-1-yloxy)tris(dimethylamino)phosphonium hexafluorophosphate (BOP, 29 mg), hydroxybenzotriazole (HOBt, 7 mg) in DMF (3 mL) and diisopropylethylamine (30 · L) were added and the suspension was stirred for 12 h at 25 °C. The particles were centrifuged at 3800 rpm for 30 min, washed with DMF and the supernatant then replaced by H_2O. The particles were re-dispersed by shaking (ultrasound) for 10 min. The supernatant was replaced by phosphate buffered saline (PBS, 1x).

To a suspension of the particles in PBS (2 mL) 250 µL of a solution of anti-erbB-2/HER-2 (1 µL/L in PBS) was added and the mixture was shaken at 0 °C for 12 h. The particles were centrifuged at 3800 rpm for 10 min, and the supernatant was replaced with PBS. The particles were re-dispersed by shaking (ultrasound) for 3 min at 0 °C.

Cell culture and viability assays

Dulbecco's modified eagle's medium (DMEM, #30-2002) and McCoy´s 5a medium (#30-2007) were purchased from ATCC. Fetal bovine serum (FBS, #S0615) was obtained from Biochrom AG and penicillin/streptomycin (#15140-122) from Gibco (#15140-122). L-glutamine (#25030-024) was purchased from Life Technologies. The viability assay based on Resazurin (#TOX8) and the 96-well plates (#CLS3603) in which the viability assay was carried out were obtained from Sigma-Aldrich (St Louis, MO, USA).

MDA-MB-435 human epithelial cells (ATCC #HTB-129) were seeded and grown in growth medium (DMEM with 4.5 g/L glucose supplemented with 10% FBS, 1% L-glutamine (200 mM) and 1% penicillin/streptomycin. SK-BR-3 human breast

adenocarcinoma cells (ATCC #HTB-30) were seeded and grown in another growth medium (McCoy´s medium supplemented with 10% FBS, 1% L-glutamine (200 mM) and 1% penicillin/streptomycin.

Imaging of the particle internalization: SK-BR-3 cells were seeded on an Ibidi 8-well plate (2E4 cells/well) and left to adhere and grow for 4 days. Subsequently, the cells were incubated with 30 µg/mL PSiP-HER-2 particles for 24 h. The cells were then washed intensively and the cell membrane stained with 20 µg/mL cell mask deep red for 10 min at 37°C before imaging. Images of living cells using transmitted and reflected light were taken with a confocal laser scanning microscope (NIKON TE2000-E). A 650 LP filter was used to collect the fluorescence signal of the cell membrane after excitation at 633 nm, whereas a 515/30 BP filter was used to collect the light reflected by the PSiP-HER-2 after irradiation with a 488 nm laser line. As previously reported, the particles exhibit intrinsic photoluminescence because of the presence of the microcavities. [35,36]

Viability assay: 20,000 cells (MDA-MB-435 or SK-BR-3) were seeded per well in a 96-well plate and incubated in 100 µL of the corresponding cell medium for 48 h at 37 °C and 5% CO_2. After this time, different concentrations of particles (PSiNPs or PSiNPs-HER-2) were added and cells were incubated for another 48 h. The viability assay was repeated three times at each concentration. Control viability assays were performed using cells without particles and particles without cells. After incubation, cellular viability was probed. Cells were washed with PBS and a solution of 10% of resazurin in growth medium was added to each well. Cells were placed in the incubator for 3 h (37 °C and 5% CO_2). Resazurin is a nonfluorescent molecule that is reduced from the oxidized to the reduced form, resofurin, by metabolically active cells. Resofurin is fluorescent, has a maximum emission wavelength at 585 nm (red emission), and can be excited from 530 to 560 nm. The fluorescent emission intensity originating from resofurin is proportional to the number of metabolically active (=

living) cells. Fluorescence emission was measured with a Fluorolog-3 spectrofluorometer equipped with a microwell plate reader (MicroMax 384) from Horiba JOBIN YVON. The samples were excited at 560 nm and the emission spectra were collected from 572 to 650 nm. Background was subtracted from the spectra. As the position of the maximum emission, wavelength can be slightly shifted, so the peak emission was averaged from 584 to 586 nm. The emission peak intensity values were normalized, considering a cell viability of 100% for the control experiments, in which no particles had been added to the cells. The normalized fluorescence emission peak intensities were plotted against the logarithm of the particle concentration, *cf.* Figure 4. Dose-response curves were obtained for SK-BR-3 and MDA-MB-435 exposed to different concentrations of Si-NPs and SiNPs-HER2, *cf.* Figure 4. The results were fitted to sigmoidal curves and the inflexion point was calculated. The inflexion point represents the LD_{50} value, which in this case is the concentration of particles at which cell viability is reduced to 50%, i.e. 50% of the cells are no longer metabolically active. The calculated LD_{50} values are shown in **Table 1**.

UNIVERSITAT ROVIRA I VIRGILI
NANO/MICROSYSTEMS FOR CANCER DIAGNOSIS AND THERAPY
Manuel García Algar

UNIVERSITAT ROVIRA I VIRGILI
NANO/MICROSYSTEMS FOR CANCER DIAGNOSIS AND THERAPY
Manuel García Algar

General Conclusions

This dissertation is focused on the development of new methods for the investigation of cancer diagnosis and therapy. Since biological fluids from patients represents a source of cancerous material, they can provide valuable information about the disease progression, when analyzing them in a liquid biopsy approach. Additionally, physicochemical properties of this circulating material, as entire tumor cells CTCs, can help to engineer systems for its both detection and therapy. The use of fluorescence and SERS spectroscopy has been widely used in microscopic and imaging techniques for the pathological evaluation of cancer disease, so methods based on them permit the advancement in potential tools for the above mentioned purposes.

In this scenario, this work accounts for enlarging the current methodologies for cancer diagnosis, by concentrating the efforts on establish robust and sensitive optical methods capable to identify cancerous material present in blood. More, taking advantage of specific cellular markers, a nanotechnological system has been constructed for the successful destruction of cancer cells, as a therapeutic weapon. In summary, this dissertation demonstrates:

1. **The feasibility of using 2-NBDG** optical probe **to discriminate tumour cells from normal blood cells** using a flow cytometric assay under optimized experimental conditions (specific incubation time and hyperoxia). This method relies on the intrinsic and universal metabolic property of the tumour cells to uptake large amounts of this glucose-based optical probe, and differs from the conventional methods using presence of cell membrane receptors. This metabolic alternative will help to solve the problems derived from the cell heterogeneity and making possible also to detect several types of CTCs in cancer patients at different stages of the disease.

2. **The capability of metabolic liquid biopsy (MLB)** to be applied **in clinical diagnosis** of human lung cancer by its further statistical **and** probabilistic analysis to determine **staging** of the progressive disease.
3. **The use of** specifically designed hybrid materials consisting in **silica microbeads coated with** interacting **silver nanoparticles for the** efficient **detection of** oncoprotein **c-MYC**, as a second liquid biopsy alternative. The metallic surface of colloids are modified with a c-MYC binding domain that transduces the c-MYC recognition events into measurable alterations of the SERS spectrum. This allows for a quantitative analysis of the c-MYC protein levels into real human samples comparing between healthy and cancer patients.
4. **The potential of engineered silicon particles** conjugated with a selective antibody against HER-2 positive breast cancer cells **as** an **immunotherapy** approach for cancer treatment. It is demonstrated specific targeting and destruction of cancer cells *in vitro* that will serve for the design and development of a novel chemotherapeutic agent against several cancer types by tuning antibody conjugation.

In summary, this work provides two new optical liquid biopsy methods: one based on a universal metabolic pathway proven in specific human lung cancer samples and another using a protein recognition nano/microsystem applied to breast cancer; and an engineered system, as a therapeutic agent for specific breast cancer, evidencing the potential of biophotonics and nanomedicine in the field of cancer research.

UNIVERSITAT ROVIRA I VIRGILI
NANO/MICROSYSTEMS FOR CANCER DIAGNOSIS AND THERAPY
Manuel García Algar

UNIVERSITAT ROVIRA I VIRGILI
NANO/MICROSYSTEMS FOR CANCER DIAGNOSIS AND THERAPY
Manuel García Algar

Appendices

1 List of figures

2 List of tables

3 List of publications

This dissertation is based on the following publications and patents:

Garcia-Algar, M.; Fernandez-Carrascal, A.; Guerrini, L.; Garcia-Rico, E.; Alvarez-Puebla, R. A., **2018 (manuscript in progress)**

Garcia-Algar, M.; Fernandez-Carrascal, A.; Nazarenus, M.; Torres-Nunez, A.; Guerrini, L.; Feliu, N.; Parak, W. J.; Garcia-Rico, E.; Alvarez-Puebla, R. A. Metabolic pathway for the universal fluorescent recognition of tumor cells. *Oncotarget* **2017,** *8* (44), 76108-76115.

Xie, H.; Garcia-Algar, M.; Nazarenus, M.; Sagalés, J.; Villanueva, C.; Gomez de Pedro, S.; Garcia-Rico, E. Apparatus and method for detection of tumour cells and circulating tumour cells. **2016**. **PATENT**

Pazos, E.; Garcia-Algar, M.; Penas, C.; Nazarenus, M.; Torruella, A.; Pazos-Perez, N.; Guerrini, L.; Vazquez, M. E.; Garcia-Rico, E.; Mascarenas, J. L.; Alvarez-Puebla, R. A. Surface-Enhanced Raman Scattering Surface Selection Rules for the Proteomic Liquid Biopsy in Real Samples: Efficient Detection of the Oncoprotein c-MYC. *J Am Chem Soc* **2016,** *138* (43), 14206-14209

Fenollosa, R.; Garcia-Rico, E.; Alvarez, S.; Alvarez, R.; Yu, X.; Rodriguez, I.; Carregal-Romero, S.; Villanueva, C.; Garcia-Algar, M.; Rivera-Gil, P.; de Lera, A. R.; Parak, W. J.; Meseguer, F.; Alvarez-Puebla, R. A., Silicon particles as trojan horses for potential cancer therapy. *Journal of nanobiotechnology* **2014,** *12*, 35.

Other publications and patents result of this thesis:

Garcia-Algar, M.; Pedrol, E.; Massons, J.; Nazarenus, M., Optofluidic device for the quantification of circulating tumor cells in breast cancer. **2017,** *7* (1), 3677.

Pedrol, E.; Martínez, J.; Aguiló, M.; Garcia-Algar, M.; Nazarenus, M.; Guerrini, L.; Garcia-Rico, E.; Álvarez-Puebla, R. A.; Díaz, F.; Massons, J., Microfluidic device with dual-channel fluorescence acquisition for quantification/identification of cancer cells. *Microfluidics and Nanofluidics* **2017,** *21* (12), 181.

Pedrol, E.; Garcia-Algar, M.; Massons, J.; Nazarenus, M.; Garcia-Rico, E.; Álvarez-Puebla, R; Sagalés, J.; Díaz, F. Optofluidic device and method for detecting circulating tumour cells. **2017**. **PATENT**

Garcia-Algar, M.; Tsoutsi, D.; Sanles-Sobrido, M.; Cabot, A.; Izquierdo-Roca, V.; Gil, H. P. R., Subcellular Optical pH Nanoscale Sensor. *ChemistrySelect* **2017,** *2* (26), 8115-8121.

Álvarez-Puebla, R.; Gómez de Pedro, S.; Garcia-Algar, M.; Nazarenus, M.; Feng, X.; Sánchez-Álvarez, M.; Sánchez-Arizmendarrieta, P.; Delgado San-Vicente, D.; Garate-Letona, A.; Alonso, J.; Puyol, M.; Calvo-López, A. A method for preparing platelet rich plasma (PRP) enriched in plasmatic growth factors and platelets. **2017**. **PATENT**

UNIVERSITAT ROVIRA I VIRGILI
NANO/MICROSYSTEMS FOR CANCER DIAGNOSIS AND THERAPY
Manuel García Algar

UNIVERSITAT ROVIRA I VIRGILI
NANO/MICROSYSTEMS FOR CANCER DIAGNOSIS AND THERAPY
Manuel García Algar

UNIVERSITAT
ROVIRA i VIRGILI